Enhancement of Charged Particle Emission from a Plasma Focus Device

A Thesis Submitted to the

College of Graduate and Postdoctoral Studies

In Partial Fulfillment of the Requirements for the

Degree of Doctor of Philosophy in

Physics in the Department of Physics and

Engineering Physics

University of Saskatchewan

Saskatoon, Saskatchewan, Canada

By

Reza Alibazi Behbahani

University of Saskatchewan

Permission to Use

In presenting this thesis in partial fulfillment of the requirements for a Postgraduate degree from the University of Saskatchewan, I agree that the Libraries of this University may make it freely available for inspection. I further agree that permission for copying of this thesis/dissertation in any manner, in whole or in part, for scholarly purposes may be granted by the professor or professors who supervised my thesis work or, in their absence, by the Head of the Department or the Dean of the College in which my thesis work was done. It is understood that any copying or publication or use of this thesis/dissertation or parts thereof for financial gain shall not be allowed without my written permission. It is also understood that due recognition shall be given to me and to the University of Saskatchewan in any scholarly use which may be made of any material in my thesis.

Head of the Department of Physics and Engineering Physics

163-116 Science Place

University of Saskatchewan

Saskatoon, Saskatchewan S7N 5E2 Canada

Abstract

Design and optimization of a low energy plasma focus for enhancing charged particle emission and x-ray radiation from the plasma focus device have been investigated. The design concept and the technical details are described. Design and fabrication of the required diagnostic instruments used to monitor the emitted charged particles and x-rays radiations are presented.

The effects of working gas on pinching regimes of the device and generation of charged particle and x-ray radiation have been investigated. Hydrogen, nitrogen, and argon have been used as working gases. The energy spectra of the ions generated in three operating gases depend on the capacitor bank voltage and the effective charge of the ions. The duration of the current drop and the injected energy into the plasma increases significantly in the high-z gases such as argon. Based on discharge circuit analysis of the device it has been found that the plasma resistance reaches 0.2 ohm during the post pinch phase in argon plasma and this anomalous resistance causes significant energy consumption during this phase.

It has also been found that the anomalous Joule heating during the post pinch phase enhances the production rate of the runaway charged particles due to reduced Dreicer field. It has been found that the runaway electron generation conditions in tokamaks and plasma focus devices are consistent in terms of the ratio of the electric field across the plasma to the electron plasma density.

To enhance the efficiency of plasma focus device as a charged particle source, a new configuration of a dense plasma focus device with three electrodes has been designed and tested. The preliminary experimental results have demonstrated that the new device can produce several focusing events in a plasma focus device. The ion beam emission and hard x-ray radiation pulses last longer than that is expected in a conventional plasma focus and their intensities are also higher.

Acknowledgements

I would like to extend my gratitude first and foremost to my supervisor Dr. Chijin Xiao for his mentorship over the course of my Ph.D. study. His insight has helped me through extremely tough times during my research. He is the one that was always with me when I had difficulties.

I would also like to extend my sincere appreciation to Dr. Akira Hirose, the director of the Plasma Physics Laboratory, for his excellent support and guidance. I would also like to thank Mr. David McColl and all my fellow graduate students.

This research was supported by the grants from the Natural Sciences and Engineering Research Council of Canada (NSERC), and the Sylvia Fedoruk Canadian Centre for Nuclear Innovation. The partial financial aid from the University of Saskatchewan and Saskatchewan Innovation Opportunity Scholarship is also much appreciated.

This is dedicated to my parents

Table of Contents

Table of Figures

List of Tables

List of Abbreviations

DPF	Dense plasma focus
DPF-SAE	Dense plasma focus with semi-active electrodes
EMP	Electromagnetic pulse
FWHM	Full width half maximum
H-X	Hard x-ray
IB	Ion bean current
LHDI	Low hybrid drift instability
MCF	Magnetic confinement fusion
MP	Magnetic piston
ICF	Inertial Confinement Fusion
SEE	Secondary electron emission mode
SLR	Short-lived radioisotope
SW	Shock wave

Chapter 1
INTRODUCTION

1.1 Magnetic Pinch

A pinch is one of the first configurations proposed for producing fusion energy by mankind. Z-pinch, theta pinch, and X-pinch are three different types of pinches to compress plasma by magnetic pressure. A pinch device is a source of intense energetic x-rays. In a pinch device, the compressed plasma lasts for tens of nanoseconds and instabilities tend to terminate the compressed plasma [1].

A zeta pinch (Z-pinch) is one of the simplest ways to produce hot and dense plasma in a laboratory. A Z-pinch is produced by an electrical discharge current in the axial direction (Z axis) as shown in Fig. 1.1. The induced magnetic field in the azimuthal direction exerts an external magnetic pressure which compresses the plasma radially inwards. During the compression phase the plasma density and temperature, and thus the internal pressure, increases. Since the plasma is highly conductive with a low resistivity, the penetration of magnetic field occurs in a time much longer than the compression time due to the skin effects. The compression dynamics depends on the difference between the internal thermal pressure and the external magnetic field. In a normal Z-pinch device the total time duration of plasma compression is of the order hundreds of nanoseconds. Therefore, it is necessary to achieve the peak of the discharge current during a very short time.

A high current pulse produced by discharging a low inductance capacitor bank is often limited to a time duration of several microseconds which is still not short enough for compression of plasma within hundreds of nanoseconds. To produce a pulse of electrical current with a suitable time duration the primary electrical pulse from a capacitor bank is transferred to a pulse forming line (PFL). The PFL would produce an electric current pulse with time duration of hundreds of nanoseconds and deliver it to the discharge electrodes. Generation of such a pulse of electricity during a brief time involves expensive equipment and complicated technologies. Usually, a significant amount of energy could be lost to the PFL.

In a Z-pinch, the magnetic field of discharge current compresses the plasma by the $\boldsymbol{J}\times\boldsymbol{B}$ force in the radial direction, where $\boldsymbol{J}$ is the axial current through the plasma and $\boldsymbol{B}$ the azimuthal magnetic field produced by the current as illustrated in Fig. 1.1. The name Z-pinch is based on the direction of the electrical current, which is in the Z-direction in the cylindrical coordinate system. In Z-pinch devices, the number density of particles reaches up to 10^{24} m^{-3}, and the plasma temperature can reach up to 1 keV within hundreds of nanoseconds. This condition is suitable for D-D and D-T fusion reactions.

A theta pinch is another method to produce a pinching plasma [1]. In a theta pinch, the current is in the theta direction and the produced magnetic field is in the Z-direction as depicted in Fig. 1.2. During the compression phase in a theta pinch, the magnetic field inside the plasma is frozen inside of the plasma due to the high plasma conductivity.

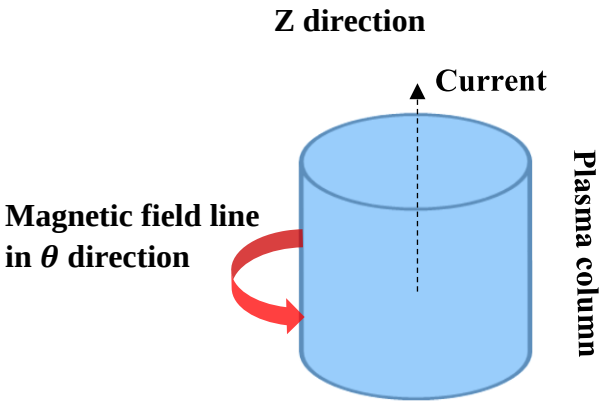

Fig. 1.1 A Z-pinch in cylindrical coordinates.

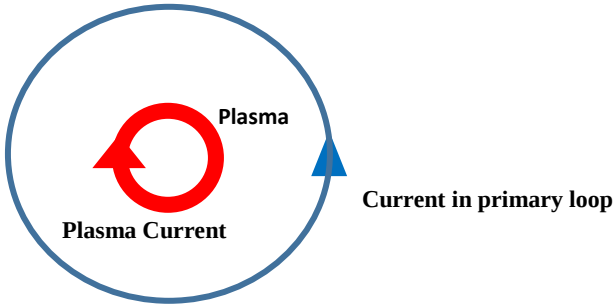

Fig. 1.2 Schematic of theta pinch configuration.

An X-pinch is another configuration for producing a dense and hot plasma by a magnetic force [1]. In an X-pinch, the current passes through an x-shaped wires. The plasma is then focused in a cross point of the wires due to the magnetic pressure as shown in Fig. 1.3.

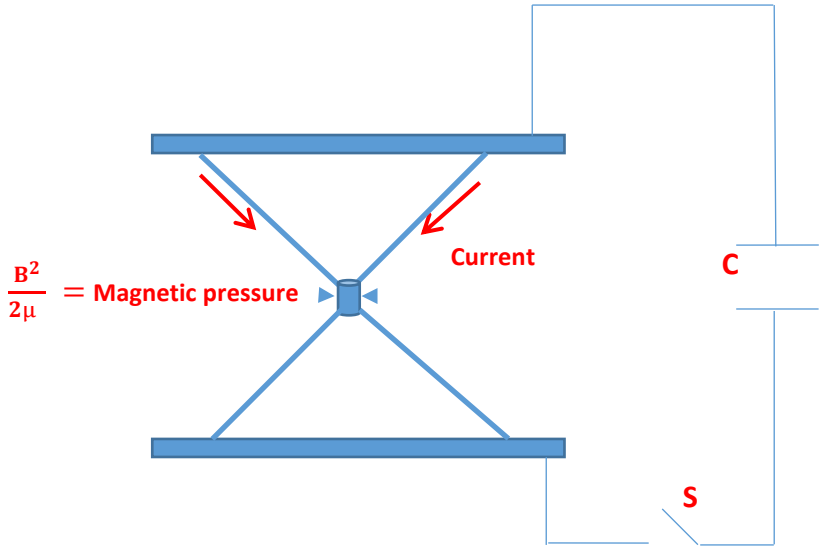

Fig. 1.3: The configuration of an X-pinch device.

1.2 Dense Plasma Focus

The high costs for making a PFL and its complicated process in a Z-pinch machine leads to the invention of the plasma focus device. Dense plasma focus (DPF) devices have been studied in 1961 by Filippov [2], and in 1965 by Mather [3]. These studies were carried out in Russia and United States independently, and led to two different configurations of the plasma focus.

A DPF device consists of a fast capacitor bank, a spark-gap switch, two coaxial electrodes, an insulator, a vacuum chamber, a vacuum pump, and inlet and outlet gas lines. The electrodes can be made of copper, brass, or tungsten. Pyrex and quartz can be used to insulate the anode and cathode. The charging voltage of the capacitor can range between 10 to 50 kV. The discharge current in a DPF device can reach up to 100 kA in a low energy device (with the stored energy $E \leq 3$ kJ), and 1 MA in a medium energy device ($E \leq 100$ kJ), and can reach up to tens of MA in a high energy device ($E \approx 1$ MJ). In a DPF device, the two coaxial electrodes are insulated by an

insulator tube (glass or ceramic) and connected to a charged capacitor bank through a switch. The electrodes are placed in a vacuum chamber filled with the low-pressure gas (0.1 to 20 Torr). When the switch is triggered, the discharge between the two electrodes breaks down the gas and produces a current sheath next to insulator. It should be noted that the electrodes and insulator, together, shape the initial discharge current in the downward axial direction as shown in Fig. 1.4. The current layer at this stage is accelerated by the $\boldsymbol{J} \times \boldsymbol{B}$ force initially in the radial direction and then also in the axial direction to form an umbrella-shaped current sheath moving axially forward, as can be seen in Fig. 1.4. Position 1 shows the break-down phase, position 2 shows the axial phase, and position 3 shows the compression phase. The break-down and axial phases are the two phases that cause a reasonable delay times in getting the compression of plasma at the peak of the discharge current.

At the compression phase, a hot and dense plasma column is formed on the top of the anode and extends in the axial direction. At this stage, charged particle beams and x-rays are generated by the compressed plasma that can last for tens of nanoseconds. The hot and densely-focused plasma lasts for a brief period of time (on the order of tens of nanoseconds). The temperature of the plasma can reach up to 1 keV, and the plasma density can reach up to 10^{25} $m^{-3.}$ The hot and dense plasma generates neutrons when Deuterium or Tritium gases are used. The occurrence of instabilities in a plasma causes a disruption that can induce a huge electric field across the plasma in the axial direction. The charged particles can be accelerated by electric fields of up to MeV per meter. The generated electron beams hit the electrodes and generate hard x-rays. Plasma focus devices may be operated in different gases with low and high atomic numbers, such as hydrogen, nitrogen, and argon.

In all plasma focus devices with different stored energies, the energy density of the pinching plasma is, $\frac{10E}{(\pi a^2)a}$ $\frac{\mathrm{J}}{\mathrm{cm}^3}$ where a is the anode radius and E the stored energy in the capacitor bank, is on the same order of magnitude. It should be noted energy density is estimated based on the ratio of stored energy in capacitor bank and the volume of plasma column (radius $\approx 0.1a$ and plasma column length $\approx a$). Plasma temperature and electron density are similar in all devices operating with low and high stored energies. It should be noted that the plasma focus with a higher stored energy can produce a greater volume of compressed plasma that lasts for a longer time compared to a low energy device [4]. The drive factor, $\frac{I}{a\sqrt{p}}$ $(\frac{\mathrm{KA}}{\mathrm{cm}\sqrt{\mathrm{mbar}}})$, where I is the peak discharge current, a anode radius, and p the operating pressure, is another important parameter which remains almost in the same range in all DPF devices [4]. In all plasma focus devices, the energy density is about 1-10 $\times$ 10^{10} $\frac{\mathrm{J}}{\mathrm{cm}^3}$ and the drive parameter is about (60 – 120) $\frac{\mathrm{KA}}{\mathrm{cm}\sqrt{\mathrm{mbar}}}$ [4]. Low-Z and High-Z gases such as hydrogen, helium, nitrogen, argon, and xenon, have been used as working gases for non-fusion applications of plasma focus. For fusion studies, deuterium and tritium have been used as working gases.

When the plasma is compressed, it will increase in both density and temperature. A considerable number of neutrons will be emitted from fusion reaction (if Deuterium gas is used). In addition, the intense radiation of x-rays and a significant number of energetic charged particles will also be emitted from a plasma focus with low and high stored energies. The low operating costs of DPF makes this device a strong candidate for industrial applications, for instance, as a charged particle source. Lithography and microlithography [5], fast x-ray imaging [6], material

processing [7], thin film deposition [8], and short-lived isotope production [9] are some of the industrial applications of the plasma focus to be introduced in the following sections.

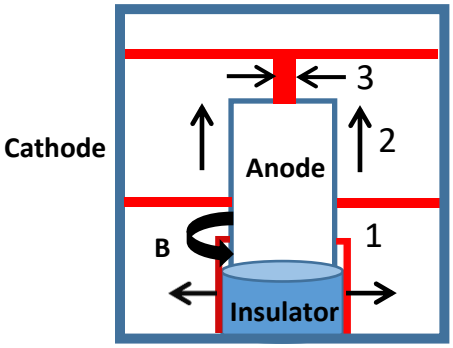

Fig. 1.4: Three positions of the current sheath in plasma focus device. "1" denotes the breakdown phase, "2" axial phase, and "3" radial phase in plasma focus. Red line shows the plasma layer.

The *m=0* and *m=1* instabilities commonly seen in DPF plasma induce huge voltages across the plasma due to the rapid change in plasma inductance [10]. Microinstabilities and turbulences in plasma can also significantly increase the plasma resistance, which causes a diode voltage across the plasma. This diode voltage can also accelerate the charged particles along the plasma column [11]. In a plasma focus, an anomalous resistance is one of the main mechanisms for plasma heating leading to neutron production [12].

The typical discharge current and tube voltage (measured at the base of the DPF) signals in a plasma focus can be seen in Fig. 1.5. The change in plasma impedance during the compression phase can cause a sharp drop in the discharge current. The duration of the current drop also shows the lifetime of the plasma column in the compression phase.

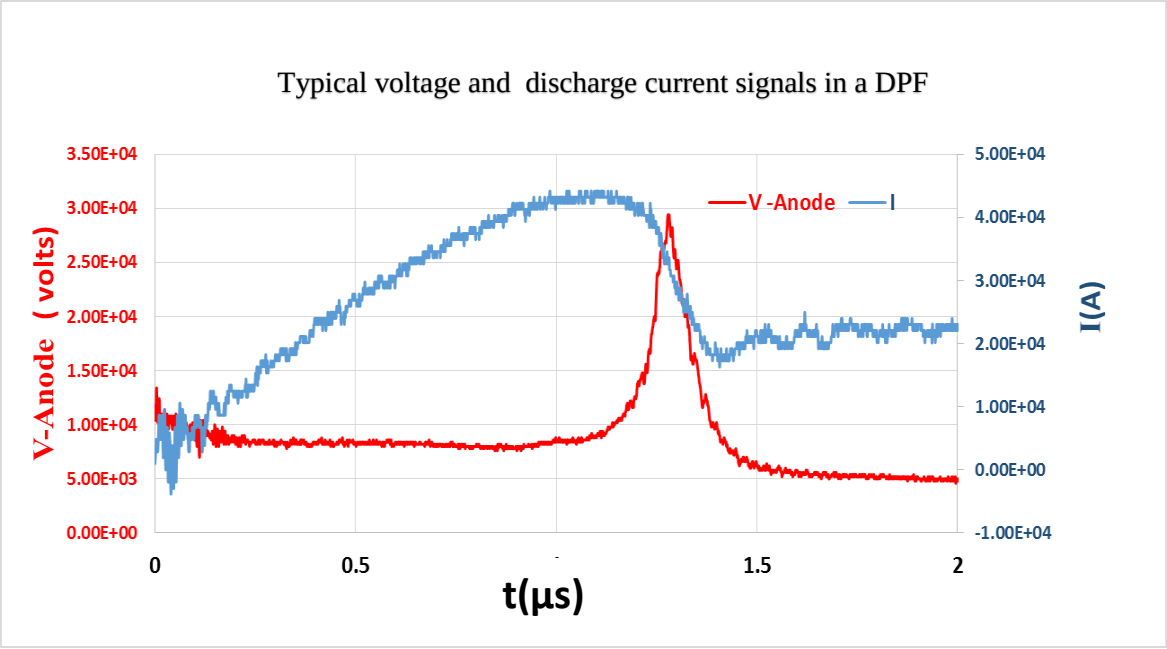

Fig. 1.5: *Typical discharge current and tube voltage traces during focusing of plasma. The current drop and voltage peak indicate the occurrences of a focusing event.*

The hemispherical plasma focus, Mather-type plasma focus, and Filippov-type plasma focus are the three types of DPF devices. The ratio of the anode radius (a) to the anode length (L) are very different in Mather type and the Filippov type. In the Mather type, the ratio $\frac{a}{L}$ is less than 1 while in the Filippov, this ratio is greater than one. Fig. 1.6 shows the Fillipov-type of the DPF device. In a hemispherical plasma focus the anode and cathode are two hemispheres that are insulated electrically from each other.

In a Filippov-type, the plasma focus break-down and compression phases are the two main phases. In a Mather-type, the plasma break-down, axial, and compression phases are the three main phases. In a hemispherical plasma focus, the break-down phase and the combined axial compression phases are the main two phases. In all types of the DPF device, a plasma pinch has

to happen when the discharging current reaches to its maximum to fully use the energy stored in the capacitor bank.

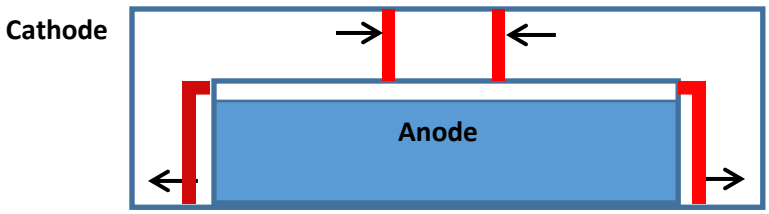

Fig. 1.6 schematics of Filippov-type dense plasma focus.

1.3 Research History on Dense Plasma Focus

The dense plasma focus has been studied for more than half a century, which has led to thousands of scientific reports. These studies on a DPF device can be divided into six aspects: Plasma dynamics, particle emission (electrons and ions), x-ray radiation, neutron radiation, and fusion energy. In the following Sections, a brief review of those studies will be presented.

1.3.1 Plasma Dynamics

The formation and acceleration of the plasma in various stages of the plasma focus are important phenomena occurring in a DPF device. It has been shown that the velocity of the current sheath plays a key role in the neutron emission in DPF devices [4]. Formation of the plasma in the break-down phase can also affect the focusing of the plasma in the compression phase [13]. In the plasma focus, the current sheath moves roughly like a rigid body. This means that the dynamics of one part of the layer depends on the other parts within the layer. A magnetic probe can be used to study the formation and acceleration of the current sheath in a plasma focus.

One of the well-known models to simulate the dynamics of plasma is the Lee model [14-15]. By coupling thermodynamics and electrodynamics of the plasma in a plasma focus, the Lee model has been used extensively for different plasma focus devices with different stored energies [12, 13, 16-19]. In this model, three phases have been considered including the plasma dynamics in the compression phase of plasma focus. The detail of the Lee model will be explained in the next chapters.

The effect of the insulator length, types of operating gas, filling pressure, charging voltage and the geometry of the electrodes on the dynamics of the plasma in the break-down phase, axial phase, and compression phase have been studied experimentally in low energy plasma focus devices [13,20-22].

In the break-down phase, the required time for the formation of the plasma layer across the insulator depends on the charging voltage, operating pressure, and insulator length [20, 21]. Decreasing the pressure and increasing the insulator length make the formation time of the plasma layer longer. Under a good focusing condition (i.e. significant current drop during the pinch phase), the formation time of the plasma layer in the breakdown phase is about 100 to 300 ns. The radial velocity of the plasma layer in the break-down phase depends on the filling gas pressure. Under a good focusing condition, the measured radial velocity of the plasma layer is about $(1\text{-}3)\times10^4\ \frac{\mathrm{m}}{\mathrm{s}}$. The focusing condition of the plasma also depends on the insulator length.

In the axial phase the anode radius, operating pressure and charging voltage, can change the axial velocity of the plasma layer [13, 21]. Decreasing the anode radius and operating pressure, and increasing the charging voltage, enhance the axial plasma layer velocity. In a good focusing

condition, the axial velocity of plasma is about (1-2) $\times 10^5 \ \frac{\mathrm{m}}{\mathrm{s}}$. In the radial phase the measured plasma layer velocity reaches up to $3\times 10^5 \ \frac{\mathrm{m}}{\mathrm{s}}$.

1.3.2 Charged Particle Emission

Due to the different applications of energetic charged particle beams, such as lithography [5], short-lived radioisotopes production [9], and thin films deposition [8], a series of experiments have been carried out to measure and optimize the energy spectrum and the number of the charged particles per shot, generated by DPF devices. Fig. 1.7 shows the directions of the charged particle beam emission from a DPF device. Ions and electrons in a plasma focus are accelerated in the opposite directions. The accelerated ions and electrons have different energy spectrums. The energy of the generated ions is about 10 keV to 10 MeV. The power density of the generated ion beam by the pinching plasma is about $10^{12} \ \frac{\mathrm{W}}{\mathrm{cm}^2}$. The energy of the electrons is about 10 keV to 1 MeV. The power density of the generated electron beam reaches $10^{13} \frac{\mathrm{W}}{\mathrm{cm}^2}$. The electron and ion current is on the order of discharge current during the pinch phase. The total energy of the generated charged particle beam can be expressed based on the fraction of the total energy stored in the inductance of pinching plasma (i.e. 0.5 $L\ I^2$, where L is plasma inductance and I the plasma current during the pinch phase) .

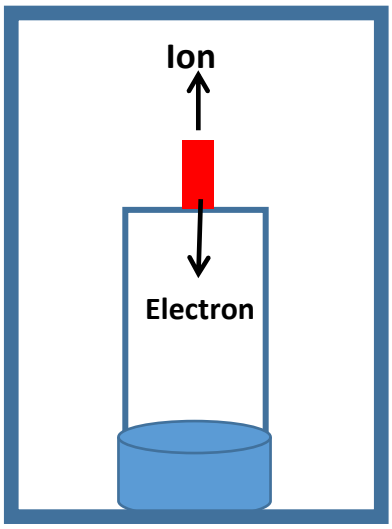

Fig. 1.7: The directions of charged particle beams emission from DPF device.

In a plasma focus, ions and electrons are accelerated by an electric field to high energies when they become runaway (i.e. drag force acts on particle is not significant). The generation of run-away charged particles in a plasma can be explained by the Dreicer Theory [23]. Based on theory, an electron becomes runaway if the component of the electric field along the magnetic field exceeds the collisional friction force. For an electron in an electric field the equation of motion can be presented by Eq. 1.1

$$m_e \frac{dv}{dt} = eE - F(v) \qquad (1\text{-}1)$$

where m_e is the mass electron, v is the electron velocity, E is the component of electric field along the magnetic field, and $F(v)$ is the friction force that is experienced by the electron. The friction force can be presented by Eq. 1-2

$$F(v) = m_e \, \boldsymbol{v} \, \nu_{ee} \qquad (1\text{-}2)$$

where ν_{ei} is the collision frequency of the electrons. By considering $\nu_{ei} \approx \frac{1}{v^3}$ the friction force $F(v) \approx \frac{1}{v^2}$. Eq. 1-1 shows that if there are no other loss mechanisms, and $\frac{m_e\, v\, \nu_{ee}}{e} \leq E$, the electron velocity is continuously increasing, and consequently the friction force that is experienced by electron becomes negligibly smaller and smaller. Hence, runaway electrons are generated if $E_C \leq E$, where $E_C = \frac{m_e\, v\, \nu_{ee}}{e}$. Due to the higher mobility of electrons compared to ions, an electron becomes runaway in a much shorter time compared to ions.

In the following chapters, the generation of runaway charged particles in a plasma focus will be explained and discussed.

In a plasma focus, three main mechanisms have been proposed to explain the generated electric field across the plasma column. The most common mechanism responsible for accelerating the ions and electrons is the inductive electric field [24-26] due to the rapid local changes in the magnetic flux accompanying the onset of the radial phase in the plasma focus device. The induced voltage across the plasma column is expressed by $V = \frac{d(LI)}{dt}$, where L is plasma circuit inductance and I is the plasma current. The induced electric filed mechanism explains the generation of energetic ions and electrons at the onset of radial phase.

The occurrence of the axial symmetrical (or $m = 0$ mode) instability also induces a plasma voltage locally across the plasma column that can accelerate ions and electrons at the end of the compression phase.

Another proposed mechanism is the anomalous resistivity effect [12, 27-28]. In the pinching plasma, resistance is increasing while the plasma current remains almost constant. Therefore, the voltage across the plasma column increases. This mechanism explains several bursts

of energetic electrons and ions observed during the pinching of the plasma and at the post pinch phase [12].

A mechanism which can explain the energy of electron up to the order of MeV is the rupture of the conductivity current due to $m = 0$ instability and the appearance of the current displacement [29]. After losing plasma conductivity, the energy in the magnetic field is converted to electromagnetic waves. The voltage across the plasma column generated by breakup of the plasma column reaches up to 60 MV. Breakup of pinch induces a huge voltage across plasma that can be counted for by including the displacement current ($\frac{\partial E}{\partial t}$). This mechanism also explains the generation of hard x-rays during the pinching phase.

Magnetic reconnecting during the pinching of the plasma column might also be a possible mechanism to induce a huge voltage across the plasma column to a value about 10 MV. The magnetic reconnection occurs within a time interval of 1 ps in a narrow gap of about (1-10 μm) [30].

The main detectors that measure the generation of electron and ion beams from a DPF device includes Rogowski coil [31], a Faraday cup [12, 32], a magnetic electron energy analyzer [33], and a Cherenkov detector [34].

1.3.3 X-ray Radiation

There are two main, and well-known, mechanisms for x-ray radiation in plasma focus devices: line and continuum radiation. The line radiation is generated by a working gas, or from the interaction between the energetic electrons and impurities. The line radiation generated from the impurities in a pinching plasma has a significant contribution in the total radiation.

In DPF machines, continuum includes recombination and Bremsstrahlung radiation. The latter is caused by the accelerating electrons in the Coulomb field of ions, producing soft and hard x-rays. The interaction of the electron beam with anode tip also generates hard x-rays with energies up to 1 MeV.

The soft x-ray energy in a plasma focus is in the range of 1 keV to 10 keV. The duration of the soft x-ray radiation in a plasma focus is approximately hundreds of nanoseconds. The generated x-ray power is about $10^8 \frac{W}{cm^2}$ at the pinch while the duration of hard x-ray generation from a pinching plasma is about tens of nanoseconds. The energy of hard x-ray is in the range of 100 keV to 1 MeV.

In a plasma focus, the $m = 0$ instability and the anomalous resistance are also the mechanisms of hard x-ray generation [12]. The anomalous resistance mechanism also explains the multiple intensity peaks of hard x-rays from a pinching plasma [12].

A plastic scintillator along with a photo multiplayer tube (PMT) and Si-based diodes, have been used to measure the energy and spectrum of the radiated x-ray from the pinching plasma. The energy spectrum of the radiated soft x-ray also gives valuable information on plasma temperature [35, 36].

1.3.4 Neutron Emission

The production of neutrons in a plasma focus is based on two main mechanisms: the thermal mechanism and the beam target mechanism [37]. The thermal mechanism of neutron production is based on the collision of energetic deuterium ions inside the bulk of the plasma. The

beam target mechanism in a plasma focus is caused by the interaction of accelerated deuterons with the plasma or background gas.

In a plasma focus, the beam target generates the most significant part of neutrons. The yield of neutron generation based on this mechanism ($Y_{b\text{-}t}$) can be expressed by Eq. 1-3 [16, 18].

$$Y_{b\text{-}t} = C_n\, n_i (I_{pinch})^2 (z_p)^2 \ln\left(\frac{b}{r_p}\right)\ \sigma\, U^{-0.5} \tag{1-3}$$

where n_i is the ion density, b is the cathode radius, r_p is the radius of the plasma pinch with length z_p, σ is the cross-section of the fusion reaction, and U is the beam energy in SI units. C_n is a calibration constant and is in the order of 10^7 [17].

In a DPF device, increasing the stored energy of the plasma focus can enhance the number of charged particles and the number of neutrons per shot. The neutron yield per shot in a low energy plasma focus is proportional to E^2. In the high stored energy plasma focus, the neutron yield is proportional $E^{0.8}$. The neutron yield will reach a saturation level by increasing the energy of the plasma focus to a higher stored energy [18].

The typical number of neutrons that can be produced by a 1 kJ plasma focus is about 10^8 $\left(\frac{\text{neutron}}{\text{shot}}\right)$. It should be noted that increasing the energy of the plasma focus device can be done by increasing the energy of the bank through increasing the charging voltage and capacitance of the bank. There is an optimum limit for a breakdown voltage across the insulator. Increasing the charging voltage over a certain experimental limit (50 kV) can cause a break-down in all space between the electrodes, and prevent a proper formation of the current layer across the insulator. Increasing the capacitance may also cause the discharge time to become longer, which allows growth of instability through the plasma current before the compression phase. The growth of

instability prevents proper formation of the plasma column in the final stage of the plasma focus. Due to the above limitations of increasing the stored energy for the plasma focus, increasing the neutron yield by increasing the stored energy of a plasma focus is not practical.

1.4 Dense Plasma Focus Applications

Dense plasma as a low cost and intense source of charged particles, x-rays, and neutron has been used for different industrial and medical applications. In the following subsections three main applications of DPF will be presented and discussed.

1.4.1 Short-lived Radioisotopes Production

The current method to produce short-lived radioisotopes (SLRs) for medical applications is through a cyclotron. The operation costs of a cyclotron can go up to millions of dollars. Furthermore, neutron emission from a cyclotron raises up safety environmental hazards. Therefore, an alternative technology is desired to produce SLRs in a safe and cost-effective way.

Production of SLRs, such as ^{13}N, ^{17}F, ^{18}F, ^{15}O, and ^{11}C, through a plasma focus is one of the promising medical applications in the medical sciences [38-44]. SLRs can be produced in a plasma focus through the bombardment of an external solid (exogenous method) or a high atomic number gas (endogenous method) targets by energetic ions as can be seen in Fig. 1.8.

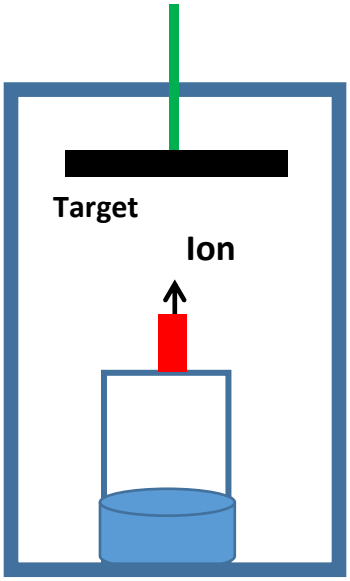

Fig. 1.8: The bombardment of target by ion beam generated by plasma.

These short-lived radioisotopes are positron emitters used for positron emission tomography (PET) imaging. It should be noted that due to its short lifetimes in these isotopes, a high number of energetic ions is needed to activate the target to a suitable level for medical applications within a time less than the half-life time of the isotopes. The main problem in using dense plasma focus devices for SLR production is that only a limited number of energetic ions can contribute to isotope activation. For instance, the lifetime of N-13 as one the important SLRs used for medical applications is about 10min, and the level required for activation is 4 giga Becquerels (GBq). Such level of activation is far greater than the maximum expected activity that one could achieve in a single shot of a medium energy plasma focus. To solve this issue, the repetitive operation of a plasma focus with a high stored energy is needed. However, technical issues, such as heating and high level of impurities, may arise during the repetitive operation of a high energy DPF device.

The highest reported activity of N-13 produced in a carbon target is about 200kBq, and was achieved by using a 76 kJ DPF device operating in a single discharge mode [44]. In general, the activation rate of nitrogen-13 in a DPF can be expressed by the Eq. 1-4 [41]:

$$N_{13} = K \int_{Emin}^{Emax} Y_{tt}\ E^{-n}\ (E)dE \qquad (1\text{-}4)$$

Where *N*, *E*, Y_{tt} are the number of activated nuclei, the energy of the ions, and a thick target yield of production, respectively. The values of unit less *n* and *K* are 5 and 5.95×10^{11} MeV^{-1}. E_{min} and E_{max} refer to the threshold energy for activation and maximum energy of ions ejected from the plasma focus. In the above equation, $K\ E^{-n}$ represents the energy distribution function of the ion beam produced by a DPF, where n ≃2. The energy distribution function shows that the number of deuterium ion decrease by increasing the ion energy.

Based on the maximum activity in low and medium energy machines, such as NX-2 (1.7 kJ) and PF-150 (operated in 20 kJ) devices, the number of high energy ions in the order of $(1-2) \times 10^{12}$ and $(1-2) \times 10^{13}$ have been reported respectively [41, 43]. These numbers have been interpreted from the measured nitrogen-13 activity. The activity of the nitrogen-13 nuclei, in Bq, can be estimated by the Eq. 1-5 where N_{od} is the number of high -energy deuterons with energy over 340 keV[41].

$$A = 10^{-9} N_{od} \qquad (1\text{-}5)$$

In a plasma focus, 10^{15} ions can be produced per kilojoules of stored energy in a capacitor bank [45]. However, only a small portion of these ions ($\simeq 10^{-3} N_{ion}$) can contribute to the activation of the ^{12}C. The minimum required energy for the N-13 activation through the ^{12}C (*d*, *n*)^{13}N reaction is about 340 keV, and the cross-section reaches its maximum at 2.5 MeV. By considering Eq. 1-4,

1 GBq activation of N-13 can be achieved by a 1 GJ DPF device in a single shot. As it is previously mentioned, operating a DPF device with such a high energy is not practical.

Repetitive operation of a DPF device might decrease the required stored energy of device. In the case of N-13 with a half lifetime of 10 min, the operation of a device with a stored energy in the order of 10^2 kJ, and with the repetitive rate on the order of 10 Hz, is needed to produce 1 GBq of N-13. It should be noted that operating a repetitive DPF reduces the neutron yield per shot in a plasma focus. Therefore, a high repetition rate may not be the only solution for SLR production [46].

By considering the above technical issues, shifting the energy spectrum and numbers of ions to higher values would be an ultimate solution for SLR production in a plasma focus. It should be noted that the number of ions produced by a 1 kJ plasma can produce 1 MBq in a single shot if all produced ions can contribute to the activation process. Based on these issues, this thesis will study the effective parameters on ion beam emission from a plasma focus.

1.4.2 Thin Film Deposition and Ion Implantation

A dense plasma focus as a source of charged particles can be used for thin film deposition [47-49], ion implantation [50-52], and phase change of thin films [53-54]. Deposition of different materials on a substrate can be done in a plasma focus by using the electron beam and the ion beam generated from the pinching plasma. In the case of electron beam, a target is placed on the tip of anode as seen in Fig. 1.9. The generated energetic electron beam hits the anode tip and sputters the target. The sputtered material gets deposited on a substrate that is placed on the top of the anode. In the second scenario the target is placed on the top of anode. The generated ion beam from the

pinching plasma hits the target and sputters it on a substrate that is placed next to target. Deposition of TiN and synthesizing of CoPt on Si substrates have been done using a low energy plasma focus [55-56].

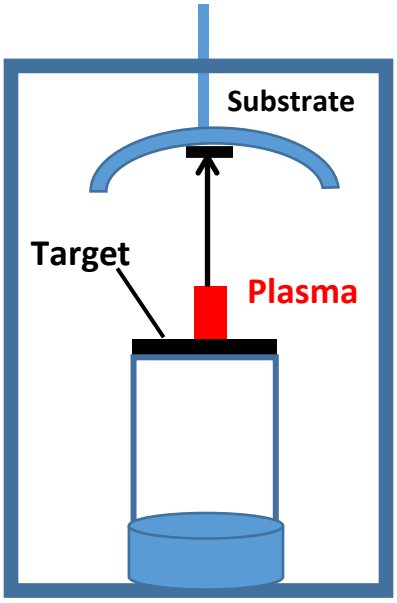

Fig. 1.9: Schematic arrangement for thin film deposition in a plasma focus.

A dense plasma focus can also be used for ion implantation and nitrating of different materials. Nitrating of Si [57], Aluminum [58], Titanium [59], and Tungsten [60] in a low energy plasma focus has been done in many reported studies. For this purpose, a substrate is placed in front of the hollow anode. Nitrogen has to be used as filling gas. The generated energetic nitrogen ions from the pinching plasma penetrates into the substrate, nitrating the substrate. The graphite carbon target on the top of the anode is also used for generating carbon ions for formation of TiC in a plasma focus [62]. Proton beams can also be generated by using hydrogen as a filling gas in a plasma focus. The proton beam is used for annealing ion-implanted semi-conductors [61]. Phase

changing of thin film is also done by using noble gases such as argon. For this purpose, a noble gas has to be used as filling gas in a plasma focus [53].

The distance of the substrate from the pinching plasma, angle of the substrate with respect to the axis of the pinching plasma, and the number of shots, are important parameters in thin film deposition and implantation processes. Decreasing the distance between substrate and anode tip would increase the thickness of the deposited thin film per shot. The thickness of the deposited thin film also increases by increasing the numbers of shots. Increasing the angle of the substrate with respect to the pinch axis also decreases the thickness of deposited thin film per shot in the plasma focus. In ion implantation process, increasing the angle of substrate with respect to the pinch axis and increasing the distance from pinching plasma would decrease the flux of the incident ion beams per surface area.

1.4.3 Detection of Illicit Materials and Explosives

Detection of illicit and explosive materials is one of the important applications of a neutron source [63-65]. Interaction of neutrons with different materials produces numbers of scattered neutrons and gamma rays. The scattered neutrons and gamma rays are produced because of the elastic and inelastic scattering of the primary neutrons with the nuclei of the irradiated matter.

The energy of the scattered neutrons in elastic interaction with different nuclei would be different due to the different masses of the nuclei. The generated gamma rays due to inelastic interactions of neutrons with the nuclei also give valuable information on elemental composition of the sample. Oxygen, nitrogen, carbon, hydrogen are the main elements that exist in explosive materials.Due to the low intensity of neutron sources ($\leq 10^{8}\ \frac{\text{neutron}}{\text{shot}}$) and the required long time

(few minutes to half an hour) in detecting the elemental composition of the object [66-68], an alternative neutron source that produces an intense pulse of neutrons is in demand.

The dense plasma focus is a cost-effective candidate of neutron source that produces up to 10^{12} fast neutrons within tens of nanoseconds. Such intense neutron source would reduce the required time for detecting the elemental composition of samples. The required short time and high accuracy of results due to the low level of noise to signal ratio also prevents the activation of exposed materials [69-70]. A dense plasma focus with a stored energy of 7 kJ, operating in D-T along with several neutron detectors (plastic scintillator + photomultiplier tube (PMT)) were used for this purpose [69-70]. The schematic arrangement of the experiment can be seen in Fig. 1.10.

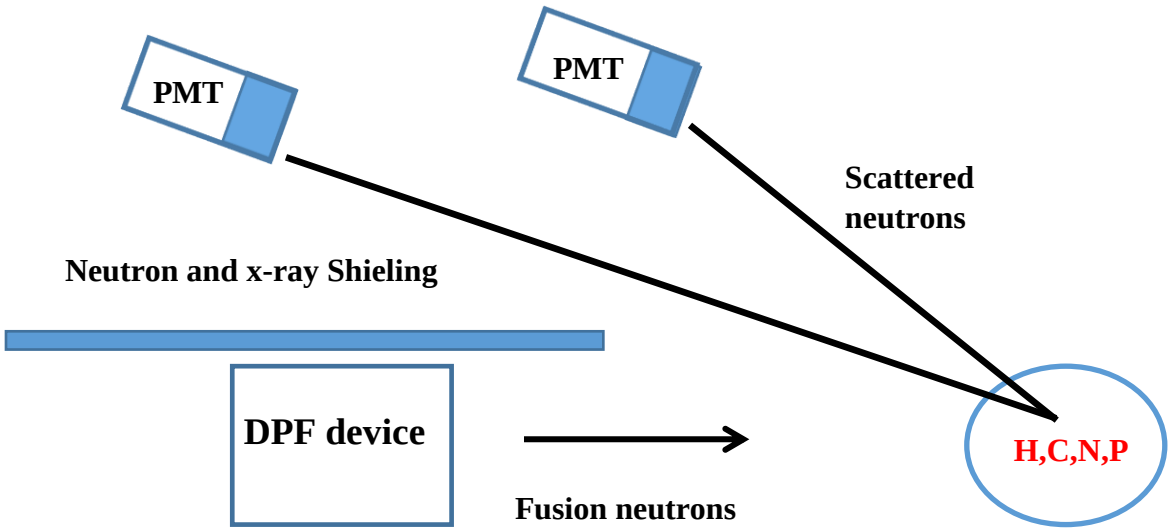

Fig. 1.10: Schematic arrangement of illicit and explosive materials detection by a DPF.

1.5 Motivation of the Thesis

Due to the important applications of charged particle sources in science and modem technologies, developing a cost-effective ion and electron beam source has a tremendous value. The primary goal of this thesis is to enhance the efficiency of a DPF device as an energetic charge particle source for the prodcution of isotopes.The main work done is listed below:

- A low energy Mather type plasma focus (DPF UofS-I) with a stored energy up to 3 kJ has been developed. DPF UofS-I has been optimized as an ion source by incorporating existing experimental results and theoretical models.
- By analyzing the discharge circuit of DPF UofS-I plasma resistance has been measured.
- The effects of anomalous resistance and plasma heating on run-away charged particles generation from pinching have been studied.
- The effects of atomic number of the gas on plasma inductance and resistance have been investigated.
- The effect of atomic number of the gas on ion emission from the pinching plasma has been explored.
- A new type of dense plasma focus has been developed.

The experimental results regarding the ion beam emission from different operating gases have been compared with simulation results based on the Lee model.

1.6 Thesis Outline

Chapter 1 covered the introduction of the plasma focus. The physics of charged particle radiations from the pinching plasma was discussed. Different types of plasma focus devices were introduced, and the limitations of using a plasma focus to produce fusion energy were presented. Short-lived radioisotope production by a plasma focus, and the technical difficulties to utilize a plasma focus as an ion source for this purpose, were explained.

In chapter 2, the Lee model, as a theoretical model to simulate operation of DPF UofS-I as an ion source, will be introduced.

Chapter 3 will be on the design and fabrication of the DPF UofS-I. The technical details regarding the building process of the DPF UofS-I will be presented and discussed. The optimization of the device as ion source based on Lee model will be explained.

Chapter 4 will be on the plasma diagnostics that have been designed and installed on the DPF UofS-I. The technical details regarding the design and fabrication of a Faraday cup as an ion beam detector, an electron beam extraction and measurement setup, a soft x-ray detector, and a hard x-ray detector, will be explained.

Chapter 5 will highlight the key results on energetic charged particle emission from a dense plasma focus device. By analyzing the discharge circuit, a new method for analyzing the anomalous plasma resistance as the main mechanism to generate energetic ions and electrons will be presented. By measuring the plasma voltage and inductance, the required electric field for runaway charged particle generation from the pinching plasma will be discussed. The Driecer theory will be considered, and the avalanche process effects of plasma heating required in electric

fields for runaway charged particle generation from the pinching plasma will be presented. It will be shown that the required electric field for runaway electron generation in the pinching plasma and Tokamaks are similar, even though the two types of devices are working on different time scales. The results regarding the current density and energy of ions generated from the DPF UofS-I as an optimized ion source will be presented and compared with the Lee model. To enhance the ion beam and x-ray generation from a plasma focus device, a new type of dense plasma focus will be introduced. Based on the electrical discharge signals, the generation of several focusing events in the new type of plasma focus will be discussed.

In chapter 6, the major results will be summarized, and possible future work will be presented.

Chapter 2

PHYSICS OF Z-PINCH

2.1 Introduction

The physics of Z -pinch is explained by considering MHD equations to predict the temporal behavior of the plasma current, temperature, and radius. By assuming: a constant line density of plasma column, thermal equilibrium of ions and electrons, quasi neutrality of plasma, and an isothermal plasma column, the MHD momentum equation for a fully ionized plasma can be expressed by Eq. 2-1.

$$mn\frac{D\boldsymbol{v}}{Dt} = -\boldsymbol{\nabla}P + \boldsymbol{J}\times\boldsymbol{B} - \boldsymbol{\nabla}\cdot\pi \tag{2-1}$$

where *m* is the mass, *n* is the particle density, ***V*** is velocity, P is the scalar diagonal pressure, ***J*** is the current density, and π is the off-diagonal pressure tensor. All elements in Eq. 2-1 are a function of time and radius for an axial symmetric system such as DPF.

The right-hand side of Eq. 2-1 shows the force from the plasma pressure, magnetic pressure, and the viscous effect. The left-hand side of Eq. 2-1 shows the inertial momentum. The derivative $\frac{D}{DT}$ is the convective derivative (i.e. $\frac{D}{Dt} = \frac{d}{dt} + \mathbf{v}\cdot\boldsymbol{\nabla}$). By ignoring the inertial term and the viscous term (considering plasma is homogenous and is in steady state), Eq. 2-1 gives

$$\boldsymbol{\nabla}P = \boldsymbol{J}\times\boldsymbol{B} \tag{2-2}$$

where $\boldsymbol{J}$ is axial current vector and **B** is azimuthal magnetic field vector in cylindrical coordinates. Maxwell's equation with no displacement current in cylindrical coordinates gives

$$\boldsymbol{\nabla} \times \boldsymbol{B} = \mu \boldsymbol{J} = \frac{1}{r} \frac{\partial}{\partial r} (r\, B)\, \boldsymbol{e_z} \tag{2-3}$$

where μ is the magnetic permittivity of plasma and $\boldsymbol{e_z}$ is the unit vector in the direction of plasma column or the axial direction. The cross product of Eq. 2-3 by $B\boldsymbol{e}_\theta$ gives

$$\boldsymbol{J} \times \boldsymbol{B} = -\frac{B}{\mu r} \frac{\partial}{\partial r} (rB)\, \boldsymbol{e_r} = -\frac{1}{2\mu r^2} \frac{\partial}{\partial r} (r^2 B^2)\, \boldsymbol{e_r} \tag{2-4}$$

The equation of state gives

$$P = \left(n_e K\, T_e + n_i K\, T_i\right) = 2nKT \tag{2-5}$$

where K is the Boltzmann's constant, T is the temperature, and the subscripts i and e refer to electrons and ions. It is also assumed that $n_e = n_i = n$ *and* $T_e = T_i = T$. The left-hand side of Eq. 2-2 in cylindrical coordinates can be expressed by Eq. 2-6.

$$\boldsymbol{\nabla} P = \frac{\partial}{\partial r} (P)\, \boldsymbol{e_r} = 2\, KT \frac{\partial}{\partial r} (n)\, \boldsymbol{e}_r \tag{2-6}$$

Substituting of Eq. 2.4 and Eq. 2.6 in to Eq. 2-2 gives

$$2\, KT \frac{\partial}{\partial r} (n)\, \boldsymbol{e_r} = -\frac{1}{2\mu r^2} \frac{\partial}{\partial r} (r^2 B^2)\, \boldsymbol{e_r} \tag{2.7}$$

By multiplying both sides of Eq. 2-7 by πr^2 and integrating over the radius, the left side of Eq. 2-7 gives where N is the linear density with a unit of $\frac{\text{number of particles}}{\text{m}}$.

$$\int_0^\infty 2\pi r^2\, KT \frac{\partial}{\partial r} (n)\, dr = -2KT \int_0^\infty 2n\pi r dr = -2KTN \tag{2-8}$$

It should be noted that in the above integration, it is assumed that n (r = ∞) = 0. Integrating the right-hand side of Eq. 2-7 gives

$$-\int_0^{\infty} \frac{1}{2\mu}\pi \ \frac{\partial}{\partial r} \ (r^2 B^2) \, dr = \frac{\mu^2 I^2}{8\pi^2} \tag{2-9}$$

By considering Eq. 2-8 and Eq. 2-9 the momentum equation gives Eq. 2-10, which is called the Bennet equilibrium equation. In Eq. 2-10, I is the plasma current. This equation expresses the balance between magnetic and thermal pressures and can be used to estimate the plasma temperature.

$$\frac{\mu^2 I^2}{8\pi^2} = 2KTN \tag{2-10}$$

The thermal pressure of plasma column can change due to thermal heating and radiation loss. Temporal variation of plasma thermal pressure can be explained by MHD energy equilibrium.

$$\frac{3}{2}\frac{DP}{Dt} + \frac{5}{2}P\boldsymbol{\nabla}\cdot\boldsymbol{V} = \eta_{\perp} J^2 - \boldsymbol{\nabla}\cdot\boldsymbol{q} - R \tag{2-11}$$

where $\eta_{\perp}$ is the classic plasma resistivity, $\boldsymbol{q}$ is the heat flux, and R is radiation loss. The first term in left hand side of Eq. 2-11 is the change in internal energy of the plasma and the second term is the work done by plasma during expansion against magnetic pressure. The first term in the right-hand side of Eq. 2-11 is Joule heating, and second term in right hand side is heat flux. At a steady state equilibrium Eq. 2-11 reduces to Eq. 2-12

$$R = \eta_{\perp} J^2 \tag{2-12}$$

Radiation loss is mainly due to Bremsstrahlung and line radiation in the pinching plasma. The Bremsstrahlung radiation is more important in hydrogen-like atoms and depends on plasma density and temperature, $R \approx n^2 T^{\frac{1}{2}}$. Classical resistance of plasma depends on plasma temperature,

$\eta_{\perp} \approx T^{\frac{-3}{2}}$. Eq. 1-12 also defines a critical current (peace current) that balance the Joule heating and Bremsstrahlung radiation loss.

In a Z-pinch, due to intense radiation of x-ray and the occurrence of anomalous resistance due to micro instabilities and turbulences, the Joule heating and Bremsstrahlung radiation loss might not stay balanced. The unbalanced energy gain/loss process in these spots produces macro instabilities characterized by the perturbations expressed in the temporal and angular components form (in cylindrical coordinate system) $x = x_0 + \sum_m x_m \sin\left(m\vartheta - \omega_m t + \varphi_m\right)$, where x represents any physical quantities, such as density, pressure, or magnetic field, x_0 the equilibrium distribution, m the poloidal mode number, and x_m, ω_m, and φ_m the perturbation amplitude, frequency and the constant phase associated with the mode m. The macro instabilities such as *m*=0 (symmetric sausage mode) and *m*=1 (kink mode) can be seen in Fig. 2.1. The magnetic pressure is expressed by $\frac{B^2}{2\mu} = \frac{\mu^2 I^2}{8\pi^2 a^2}$ where *B* is the magnetic field caused by the plasma current.

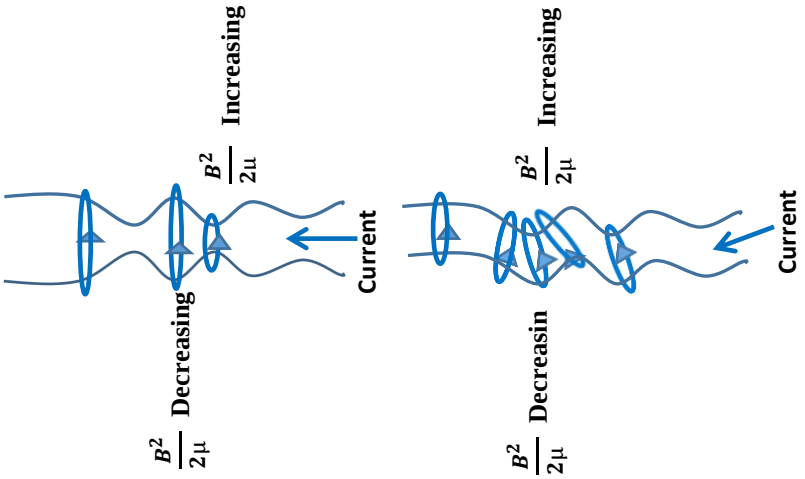

Fig. 2.1: Macro instabilities such as m=0 and m=1 through the plasma column.

The resistive diffusion of magnetic field into plasma is another reason that terminate plasma confinement when plasma resistance becomes significant. The temporal and spatial evolution of magnetic field can be expressed by Eq. 2-13, where $\boldsymbol{v}$ is ion velocity, η is plasma resistance, and μ_0 is vacuum magnetic permittivity.

$$\frac{\partial \boldsymbol{B}}{\partial t} = \boldsymbol{\nabla} \times (\boldsymbol{v} \times \boldsymbol{B}) + \frac{\eta}{\mu_0} \nabla^2 B \qquad (2\text{-}13)$$

The first term in the right-hand side of Eq. 2-13 shows convection term. The second term in the right-hand side of Eq. 2-13 is resistive diffusion term. In the case of hot and dense plasma when the plasma resistance is negligible the magnetic field is frozen into plasma and diffusion of magnetic field in to plasma occurs in a time much longer than the confinement time.

The electrodynamic of plasma in z-pinch machine can be explained by some model such as snowplough and slug models. In snowplough model the current flows in a skin layer which acts as a piston. As the piston moves it produces a supersonic wave in front of plasma skin layer. A fraction of the ionized gas is accumulated by the supersonic wave in this skin layer as in a snowplough [1]. In the slug model the movement of current layer produce a supersonic wave that ionizes the gas in front of the piston. In slug model, it is assumed plasma reaches to a minimum radius when the supersonics wave reaches to the central axis [1]. One well-known model that is based on snowplough model and slug the model is Lee model [14, 15]. In the following part the Lee model will be explained.

2.2 Lee model

The Lee model is a well-known model that has been used in different Mather-type and Fillipov-type plasma focus devices to predict the dynamics of the plasma, production of neutrons, and emission of charged particles from the pinching plasma [14, 15]. The model incorporates the plasma electrodynamic and thermodynamics equations, and the geometry of electrodes, trying to reproduce the experimental electrical signals (i.e. discharge current and voltage between anode and cathode) and predict the output of plasma focus as a neutron and charged particle source. In the Lee model, the break-down, axial, and compression are the three main phases of plasma dynamics in a Mather-type plasma focus device. The compression phase is divided into: inward radial shockwave phase, outward reflected shock wave phase, and slow compression phase. In the following sections, a description of each of the phases will be presented and explained.

2.2.1 Axial Phase

In the Lee model, the axial phase is initiated after the break-down phase. In this phase, the current layer that is formed in the break-down phase is accelerated by the $\boldsymbol{J} \times \boldsymbol{B}$ force in the axial direction, as can be seen in Fig. 2.2. An umbrella shaped current makes a shock wave (SW) in its front due to the magnetic pressure (MP). The shockwave makes the gas ionized and forms a plasma layer on its backside as can be seen in Fig. 2.2.

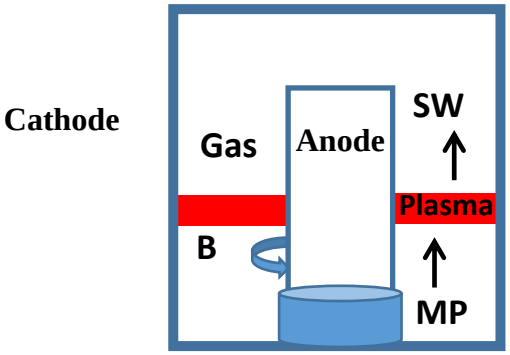

Fig. 2.2: The formation of plasma layer in plasma focus.

The plasma layer carries the fraction of the mass of the gas (f_{ma}) that is filling the space between the anode and cathode from the bottom to the top of the discharge electrodes. z is the axial position of the current layer from the base plate. By assuming $z=0$ as an initial position of the current layer, $Z=Z_0$ as the final position of current layer, n_0 as number of atoms per volume, m as the atomic mass of the filling gas, a as the anode radius, b as the cathode radius, and f_{ma} as a fraction of mass that carry by plasma, the total mass of plasma can be estimated by $f_{ma} n_\circ m z \pi \left(b^2 - a^2\right)$. Fig. 2.3 shows the axial phase in Mather-type plasma focus.

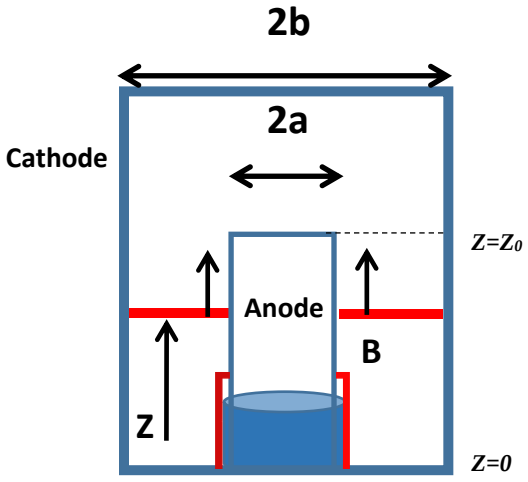

Fig. 2.3: The axial phase in a Mather type plasma focus.

The voltage across the discharge tube (V_{tube}) can be expressed by Eq. 2-14,

$$V_{Tube} = \frac{d\,(L(t) f_c\, I)}{dt} + r f_c\, I = V_0 - \frac{\int_0^t I dt}{C_0} - L_0 \frac{dI}{dt} - R_0 I \qquad (2\text{-}14)$$

where f_c is the fraction of discharge current that pass through plasma, V_0 is the charging voltage of the capacitor, C_0, L_0, R_0 are the capacitance, static inductance, and static resistance of the discharge circuit. I is the discharge current, while $L(t)$ and $r(t)$ are time dependent inductance and resistance of the discharge tube, respectively.

By assuming that the inductance of tube $L(t) = \mu/2\pi\, z\,(t) \ln (b/a)$ in the axial phase, Eq. 2-14 gives the time derivative of the discharge current where $c = b/a$.

$$\frac{dI}{dt} = \left[V_0 - \int \frac{Idt}{c_0} - (R_0 + r(t))I - I f_c \frac{\mu}{2\pi} (\ln c) \frac{dz}{dt} \right] \Big/ \left[L_0 + \frac{f_c \mu}{2\pi} (\ln c)\, z \right] \qquad (2\text{-}15)$$

By considering the plasma as a rigid body the total magnetic force that pushes the plasma in the axial direction can be expressed by Eq. 2-16

$$F_z = \int_a^b I_p \times \frac{\mu I_P}{2\pi r} dr = \frac{\mu I_p^2}{2\pi} \ln\left(\frac{b}{a}\right) \qquad (2\text{-}16)$$

where $I_P = f_c I$ and f_c is an input fitting parameters in the model.

By considering the mass of the plasma, the momentum equation in the axial phase can be expressed by Eq. 2-17,

$$F_z = \frac{d(mV)}{dt} = \frac{d}{dt}\left(\left[\rho_0 \pi \left(b^2 - a^2\right) z \right] f_{ma} \frac{dz}{dt} \right) = \rho_0 \pi \left(c^2 - 1\right) a^2 f_{ma} \frac{d}{dt}\left(z \frac{dz}{dt} \right) \qquad (2\text{-}17)$$

where $\rho_0 = n_0 m$ is the mass density, $c = b/a$, and z is the distance of plasma sheath from the baseplate. By substituting Eq. 2-16 in Eq. 2-17, the momentum equation can be expressed by Eq. 2-18 where

$$\rho_0 \pi \left(c^2 - 1\right) a^2 \, f_{ma} \frac{d}{dt}\left(z \frac{dz}{dt} \right) = \frac{\mu I_p^2}{2\pi} \ln\left(c\right) \tag{2-18}$$

Assuming that the plasma current arrives at the top of the anode at the time, t_a, from the start of the discharge. This characteristics time depends on the anode length Z_0 among other parameters and can be derived from Eq. 2-18 by considering $\frac{dz}{dt} = \frac{z_0}{t_a}$ where t_a is the duration of axial phase when the current reaches to the top of the anode, $z = Z_0$, and $I_P = f_c I$.

$$t_a = \left[\frac{4\pi^2 (c^2 - 1)}{\mu \ln c} \right]^{1/2} \frac{\sqrt{f_{ma}}}{f_c} \frac{Z_0}{(I/a)/\sqrt{\rho_0}} \tag{2-19}$$

The choice of the characteristics time t_a should match the discharge time of the capacitor bank ($\sqrt{C_0 L_0}$). Eq. 2-19 gives an estimation of a proper electrode geometry and operating pressure of filling gas, based on the discharge time of the capacitor bank. It should be noted that Eq. 2-15 and Eq. 2.18 are coupled equations. The change in plasma current ($\frac{dI}{dt}$) depends on $\frac{\mathrm{d}L(t)}{\mathrm{d}t}$ and the change in the tube inductance depends on the plasma current (i.e. $\frac{\mathrm{d}L(t)}{\mathrm{d}t} \propto \frac{dZ}{dt} \propto I_P^2$). Lee solved the two coupled equations 2-15 and 2-18 numerically for z and I to reproduce the discharge current waveform in the axial phase using the known electrical constants C_0, V_0, R_0, ρ_0 (based on the

operating pressure) and the geometry of electrodes, and also assuming vanishing resistance $r(t) \simeq 0$ during the axial phase as a very good approximation. Afterwards, the voltage waveform $V(t)$ can be solved by combining Eq. 2-16 and Eq. 2-17.

2.2.2 Inward Shockwave Phase

When the plasma layer arrives at the top of the anode, the $\boldsymbol{J} \times \boldsymbol{B}$ force pushes the plasma layer into the center of the anode. The first stage in the compression phase is the inward radial shock phase. In this phase, a plasma column with the inner radius of r_s and the outer radius of r_p (Fig. 2.4) will form on the top of the anode. The r_s shows the shockwave distance from the center of the anode and r_p shows the outer radius of plasma column from the center.

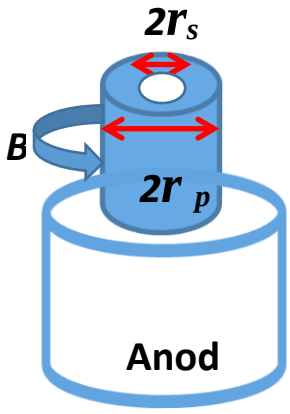

Fig. 2.4: The inward radial shock wave in final stage of plasma focus.

In this phase, the magnetic compression pressure caused by the $\boldsymbol{J} \times \boldsymbol{B}$ force on the outer side of plasma column creates a shockwave inside the plasma column. The shockwave moves into the center of the anode and compresses the gas inside the plasma column. The shockwave will leave the ionized gas in its backside that forms a plasma layer in the radial phase. The plasma layer

moves radially into the center of plasma by a magnetic pressure. Due to the open end of plasma column, it is expected that the shockwave also moves in the axial direction and causes an elongation of the plasma column in the axial direction. By using Eq. 2-14, and the plasma column inductance $\mu / 2\pi \, Z_f(t) \ln(b / r_p(t))$, where Z_f is the length of plasma column, the time derivative of the discharge current in the compression phase can be expressed by Eq. 2-20.

$$\frac{dI}{dt} = \frac{V_0 - \int \frac{Idt}{C} - (R_0 + r(t))I - f_c \frac{\mu}{2\pi}\left(\ln\frac{b}{r_p}\right) I \frac{dZ_f}{dt} + f_c \frac{\mu}{2\pi}\frac{Z_f}{r_p} I \frac{dr_p}{dt}}{L_0 + f_c \frac{\mu}{2\pi}(\ln c) Z_0 + f_c \frac{\mu}{2\pi}\ln\left(\frac{b}{r_p}\right) Z_f} \tag{2-20}$$

Eq. 2-20 shows that increasing the plasma inductance or resistance will result in a drop in the discharge current during the compression phase.

The dynamics of the shockwave and the plasma can be explained by the theory of shockwaves and thermodynamics of plasmas during the compression phase. As mentioned, the magnetic pressure drives the shockwave in the filling gas. The shockwave velocity can be derived by Eq. 2-21, where P_B is magnetic pressure and V_s is the shock wave velocity (i.e. $\frac{d}{dt} r_s$).

$$P_B = \frac{2}{\gamma + 1} \rho_0 V_s^2 \tag{2-21}$$

Where $\gamma = \frac{c_p}{c_v}$ is the ratio of the specific heats at constant pressure (c_p) and volume (c_v). By substituting the magnetic pressure, $P_B = \left(\mu I f_c / 2\pi r_p \right)^2 \Big/ 2\mu$, the shock velocity can be expressed by Eq. 2-22 where f_{mr} is radial mass fraction.

$$\frac{dr_s}{dt} = -\left[\frac{\mu(\gamma+1)}{\rho_\circ}\right]^{1/2} \frac{f_c}{\sqrt{f_{mr}}} \frac{I}{\sqrt{8\pi}\, r_p} \tag{2-22}$$

The negative sign shows the inward movement of shockwave in the compression phase.

By assuming the time duration when the plasma current reaches to the center of anode (t_r) as the characteristics time and the anode radius (a) as characteristic length (i.e.$\frac{dr_s}{dt} \approx \frac{a}{t_r}$), Eq. 2-22 gives

$$V_r = \frac{a}{t_r} = \frac{\left[\mu(\gamma+1)\right]^{1/2}}{4\pi} \frac{f_c}{\sqrt{fmr}} \frac{I_\circ / a}{\sqrt{\rho}} \tag{2-23}$$

Eq. 2-24 can be used to estimate the radial compression phase in a plasma focus based on the anode radius, the operating pressure, and the discharge current.

$$t_r = \frac{4\pi}{\left[\mu(\gamma+1)\right]^{1/2}} \frac{\sqrt{f_{mr}}}{f_c} \frac{a}{\left(I_0 \big/ a\sqrt{\rho}\right)} \tag{2-24}$$

The plasma column is an open-end column, and the compression of the gas in the radial direction creates a shockwave in the axial direction. Based on the propagation theory of shockwaves in the radial and axial directions, the axial velocity of shockwave can be expressed in terms of radial velocity of the shockwave by Eq. 2-25.

$$\frac{d\,Z_s}{dt} = -\left(\frac{2}{\gamma+1}\right)\frac{dr_s}{dt} \tag{2-25}$$

By assuming $Z_s \simeq Z_f$, Eq. 2-25 can define the elongation of the plasma column in the compression phase.

As can be seen in Eq. 2-20, the change in discharge current ($\frac{dI}{dt}$) column depends on the change of the plasma radius ($\frac{dr_P}{dt}$). By assuming that the plasma resistance is a negligible term, the compression of the plasma can be an adiabatic process (i.e. $PV^{\gamma} = constant$).

The differential from the magnetic pressure gives $\frac{dp}{p}$ can be expressed by Eq. 2-26

$$\frac{dp}{p} = 2\left[\frac{dI}{I} - \frac{dr_p}{r_p}\right] \tag{2-26}$$

The differential of $PV^{\gamma} = constant$ can be expressed by Eq. 2-27

$$\frac{\gamma\, dV}{V} + \frac{dP}{P} = 0 \tag{2-27}$$

Expressing the plasma volume as $V = \pi\left(r_p^2 - r_s^2\right)Z_f$ the dV can be expressed by Eq. 2-28.

$$dV = 2\pi\left(r_p\, dr_p - r_s\, dr_s\right)Z_f + \pi(r_P^2 - r_S^2)dZ_f \tag{2-28}$$

Substituting Eq. 2-27 and Eq. 2-28 in Eq. 2-26, gives

$$\frac{2\gamma\left(r_p dr_p - \frac{2}{\gamma+1} r_s dr_s\right) z_f + \gamma\left(r_p^2 - r_s^2\right) dz_f}{z_f\left(r_p^2 - r_s^2\right)} + 2\frac{dI}{I} - \frac{2dr_p}{r_p} = 0 \qquad (2\text{-}29)$$

The time rate of the change of plasma column radius can be expressed by Eq. 2-30

$$\frac{\gamma\left(r_p \frac{dr_p}{dt} - \frac{2}{\gamma+1} r_s \frac{dr_s}{dt}\right) z_f + \frac{\gamma}{2}\left(r_p^2 - r_s^2\right)\frac{dz_f}{dt}}{z_f r_p \left(1 - \frac{r_s^2}{r_p^2}\right)} + \frac{r_p}{I}\frac{dI}{dt} = \frac{dr_p}{dt} \qquad (2\text{-}30)$$

Eq. 2-20 and Eq. 2-30 are coupled equations that Lee solved numerically for I and r_p by considering electrical constants C_0, V_0, R_0, ρ_0 (based on operating pressure), geometry of electrodes and Eq. 2-20 and Eq. 2-25 .

2.2.3 Reflected Shockwave Phase

The shockwave will be reflected radially in the outward direction after hitting the center of the anode; this time would be the onset of the radially reflected shockwave phase as can be seen in Fig. 2.5. Based on the shockwave theory, the speed of reflected shockwave can be presented by Eq. 2-31

$$\frac{dr_{Rs}}{dt} = -0.3\left(\frac{dr_s}{dt}\right)_{on-axis} \qquad (2\text{-}31)$$

The axial elongation of the plasma column will continue with the velocity expressed by Eq. 2-32

$$\frac{dZ_f}{dt} = -\left(\frac{2}{\gamma+1}\right)\left(\frac{dr_s}{dt}\right)_{on-axis} \qquad (2\text{-}32)$$

In this phase, the time derivative of the discharge current can be expressed by Eq. 2-20. The time rate of the plasma column radius can be calculated by Eq. 2-30 by substituting $\frac{dr_s}{dt} = 0$ (as the volume of plasma column will not decrease due to reflection of shockwave), and $r_s \simeq 0$ at the time of the maximum compression of gas at the center of the anode by the shockwave.

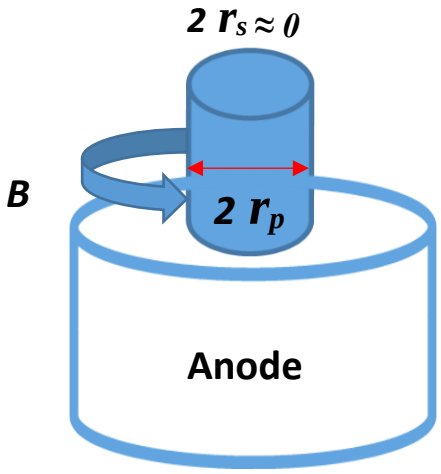

Fig. 2.5: The reflected shockwave phase in plasma focus.

$$\frac{dr_p}{dt} = \frac{-\frac{r_p}{\gamma I}\frac{dI}{dt} - \frac{r_p}{Z_f}\frac{dZ_f}{dt}}{\frac{\gamma-1}{\gamma}} \qquad (2\text{-}33)$$

This phase will end when the reflected shockwave hits the plasma layer (i.e. $r_s = r_p$).

2.2.4 Slow Compression Phase

The slow compression phase starts when $r_s = r_p$ as the reflected shockwave produces a pressure in the opposite direction of the magnetic pressure. At this time, the plasma column is compressed to its minimum radius when the inner plasma pressure reaches its magnetic pressure. By considering the plasma density and the plasma current, and using the Bennet equation, the peak of the plasma temperature is estimated.

The plasma resistance has to be taken into account due a small plasma column radius. Plasma radiation is significant due to a high density and temperature of the plasma, and the compression of plasma is not adiabatic in this phase.

Eq. 2-20 presents the time derivative of the discharge current. To find the time rate of the plasma radius, Lee used the first thermodynamics law $dh = dQ + Vdp$, where h is the enthalpy of the plasma. Considering the energy gain and loss terms, dQ can be expressed by Eq. 2-34.

$$dQ = d\left(Q_{jouleheating} + Q_{radation} - E_{ion}\right) \tag{2-34}$$

where $Q_{joule\ heating}$ is caused by plasma resistance. $Q_{\text{radiation}}$ includes all the x-ray radiation for a compressed plasma, and E_{ion} is the amount energy that is consumed to ionize the atoms. Enthalpy can be also expressed by Eq. 2-35

$$h = \frac{\gamma}{\gamma - 1} PV \tag{2-35}$$

By differentiating the enthalpy, the first law of thermodynamics gives

$$dh = \frac{\gamma}{\gamma - 1}(dPV + PdV) = dQ + Vdp \tag{2-36}$$

$$\gamma p dV + V dP = (\gamma - 1) dQ \tag{2-37}$$

By doing the same process for finding *dV* and *dP* in the first stage of the compression phase, the time rate of the plasma column radius can be expressed by Eq. 2-38

$$\frac{dr_p}{dt} = \left(-\frac{r_p}{\gamma I}\frac{dI}{dt} - \frac{1}{\gamma + 1}\frac{r_p}{Z_f}\frac{dZ_f}{dt} + \frac{4\pi(\gamma - 1)}{\mu\gamma Z_f}\frac{r_p}{f_c^2 I^2} \times \frac{dQ}{dt} \right) \Big/ \frac{\gamma - 1}{\gamma} \tag{2-38}$$

The change of plasma column length in this phase will be derived by considering the internal pressure of plasma. This pressure can create a shockwave in the axial direction with the velocity expressed by Eq. 2-39. The maximum change in plasma column length can be expressed by Eq. 2-39 when the internal pressure of plasma reaches to magnetic pressure.

$$\frac{dZ_f}{dt} = \left[\frac{\mu}{4\pi^2(\gamma + 1)\rho_0} \right]^{1/2} \frac{I f_c}{r_p} \tag{2-39}$$

Eq. 2-38 and Eq. 2-20 can be solved numerically by calculating the plasma resistance and energy loss by x-ray radiation in this phase. Lee incorporated the classical term of plasma resistance, power loss by the line and Bremsstrahlung radiations into the model, and predicted the dynamics of plasma in this phase.

It should be mentioned that incorporating the x-ray radiation and self-absorption of plasma Lee could predict the radiation-enhanced compression of plasma that is the subject of many theories related to DPF [71]. Radiation-enhanced-compression is caused by a drop of internal plasma pressure due to the extreme x-ray radiation from the plasma. In this thesis, the occurrence of radiation-enhanced-compression will be shown experimentally.

2.2.5 Instability Phase

When the plasma reaches to its maximum compression, the plasma column may also be unstable in a very short period of time due to the occurrence of instabilities in the plasma. The occurrence of instabilities in plasma makes the plasma resistance anomalous in the post pinch phase.

Lee also incorporated the anomalous resistance in the code to explain the energy consumption after the pinch phase [45]. In this thesis, the predicted anomalous resistance in the post pinch phase that is the subject of many types of research on plasma focus devices will be measured experimentally. The time variation of anomalous resistance is usually assumed to be $R = R_0\left[e^{\frac{-t}{t_2}} - e^{\frac{-t}{t_1}}\right]$ where t_1 is the characteristic rising time of anomalous resistance, t_2 is the characteristic fall time of anomalous resistance, and R_0 is in the order of 1 Ω. In the Lee model it is assumed that the plasma resistance becomes anomalous after the pinch phase.

Lee also developed his model to predict the ion numbers produced per shot from a plasma focus [72]. In this research, the predicted ion number will be examined experimentally.

2.3 Lee Code

Lee uses an excel code to run his model. To run the Lee code, the required input parameters are the capacitance (C_0) , static inductance(L_0), the geometry of electrodes (a, b), and filling pressure(P_0) of operating gas. The code is use to reproduce the experimental discharge current and tube voltage as can be seen in Fig. 2.6.

The output of the code based on the simulated electrical signals of a plasma focus (i.e. discharge current and tube voltage) are the plasma dynamics in the axial and compression phases, plasma temperature and density, the number of neutrons generated per shot, soft x-ray yield, and the ion beam yield. All the output results are plotted separately in an excel sheet. The parameters have been used to produce the current and voltage are a= 1.5 cm, b= 4.5 cm, gas pressure p=3 Torr, C_0= 4.5 µF, and V_0= 30 kV.

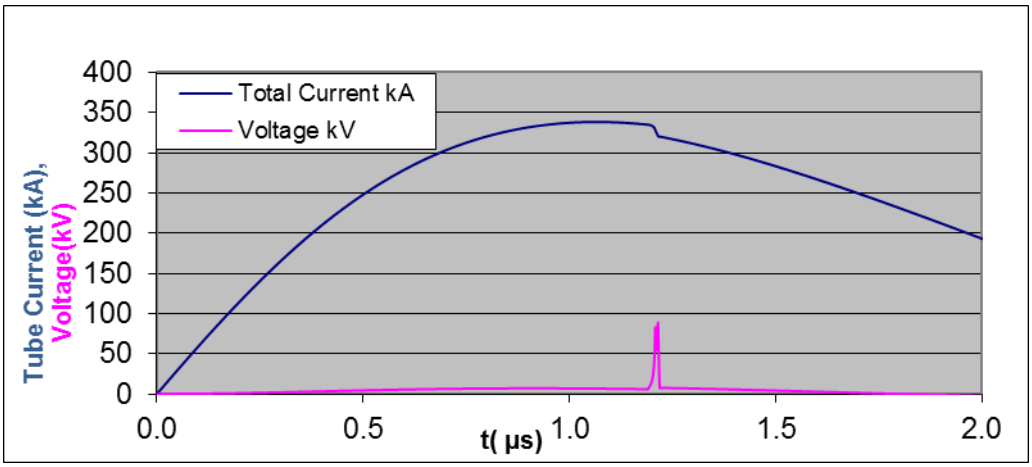

Fig. 2.6: The discharge current and voltage waveforms simulated using Lee code.

Chapter 3

DPF UOFS-1

3.1 Introduction

The design and fabrication of any dense plasma focus machine can generally be divided into two main steps. The first step is the simulation and fitting process to find the best configuration of the coaxial discharge tube composed of the cathode and anode. The important parameters in this step are the characteristics of the capacitor bank and the types and pressure of the filling gas. The second step involves fabrication and assembly of the vacuum chamber, spark gap, trigger and control circuits, discharge tube, and transmission line and diagnostic tools.

The type of dense plasma focus can be chosen by the available bank energy. Many reports presented an efficient operation of a Mather-type plasma focus with a low stored energy. In this thesis, a low energy capacitor bank, Mather-type plasma focus has been implemented. The aim of the optimization of the discharge tube is to get an achievable compression of the plasma near the peak discharge current of the capacitor bank. To reach this goal, two key parameters are important. The first parameter is the energy density, which is expressed as $\frac{E}{a^3}$, and the second is the drive parameter $\frac{I}{ap^{0.5}}$, where *E, a, I* and *p* are stored energy, anode radius, peak discharge current, and pressure, respectively. The energy density and the drive parameter is in the same range in all Mather-type plasma focus devices, almost independent of the stored energy. In all DPF machines with different stored energies, the drive parameter is in the range of 60 and 120 $\frac{\mathrm{kA}}{\mathrm{cm}\cdot\mathrm{mbar}^{0.5}}$ and the energy density is in the range of $(1-10)\times 10^{10}\ \frac{\mathrm{kJ}}{\mathrm{cm}^3}$ in deuterium gas.

3.2 Optimization of DPF UofS-I as an Ion Source

After considering the static inductance of the capacitor and transmission line used in the experiment(L_0), the maximum stored energy of the device (E≈2 kJ), the estimated peak discharge current (I) based on magnetic and electrostatics energy balance ($E \approx L_0 I^2$) , the aforementioned scaling parameters have suggested a feasible range of anode radius between 0.8cm and 1.7cm. To optimize the drive parameter of a DPF machine as an ion source for a fixed stored energy, the operating pressure, and plasma sheath velocity must be considered. The operating pressure plays an important role in the beam loss. Plasma sheath velocity is important as it is related to the pinch formation and the induced diode voltage. Taking these aspects into account in the optimization process for deuterium gas (explained in the following parts), the drive parameter has been chosen to be 90 $\frac{\mathrm{kA}}{\mathrm{cm}\cdot\mathrm{mbar}^{0.5}}$ (a = 1.5 cm, p = 1 Torr , and I_{peak} =140 kA) for the DPF UofS-I machine.

To produce the positron emitting isotopes, one of the possible medical applications of a DPF device, two main parameters are crucial for the ion beam production. The first is the energy of ions, and the second is the ion beam current. The higher energy and number of the ions lead to a higher rate of isotope production. It should be noted that the minimum ion energy to produce nitrogen-13 using deuteron beam is 340 keV.

The energy of the ion beam and the ion beam current generated in DPF devices are governed by the discharge current, plasma sheath velocity, gas pressure, anode shape and circuit parameters. The higher discharge current and better optimization of the anode shape generate more energetic ions, and the lower operating pressure beam leads to a lower beam loss, or a higher ion

number per shot. Plasma sheath velocity is another important optimization parameter for a DPF device.

In order to optimize the parameters of the DPF UofS-I device to maximize the isotope production, the Lee model has been used. The Lee model gives good estimations on the total number of generated ions, the beam energy, and the beam current, which are important parameters for isotope production.

The simulation results show that the total number of generated ions, beam energy and current are maximized with the following parameters: the anode radius a=1.5 cm, anode length b=7 cm, and the deuterium gas at working pressure of 1mbar. By choosing the maximum radius of the anode, the best focusing effect can be achieved under low operating pressures, leading to a higher sheath velocity and minimum beam loss effect in the machine. Maximum anode radius corresponds to a lower inductance of discharge tube and a higher discharge current. According to previous studies on ion beam emission from DPF machines (operating in deuterium gas) the highest sheath velocity of 10 cm/μs is optimum for good focusing effect and production of high energetic deuterons. This velocity is limited by a suitable plasma sheath thickness for strong focusing effect. The DPF UofS-I simulation results show a peak discharge current that can reach up to 140 kA, as can be seen in Fig. 3.1. The current drop shows the transfer of energy to plasma during the pinch. The Lee model also shows a lifetime of focused plasma about 20 nsec.

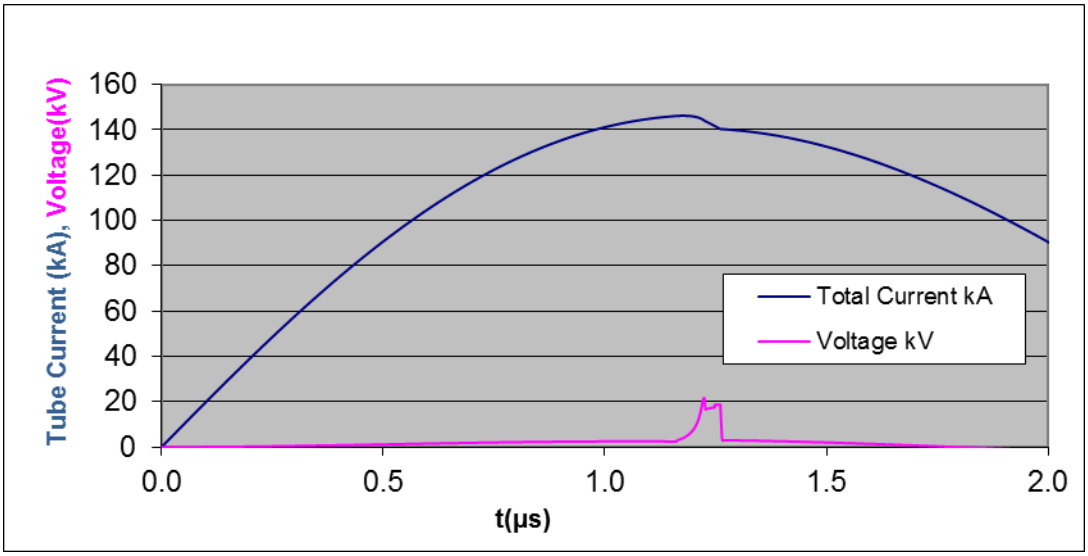

Fig. 3.1: The peak tube current approximately 140 kA and tube voltage reaches up to 30 kV. The operating pressure is 1 Torr.

The peak axial velocity about 10 cm/μsec can be achieved under the operation conditions assumed in the simulation code, as can be seen in Fig. 3.2.

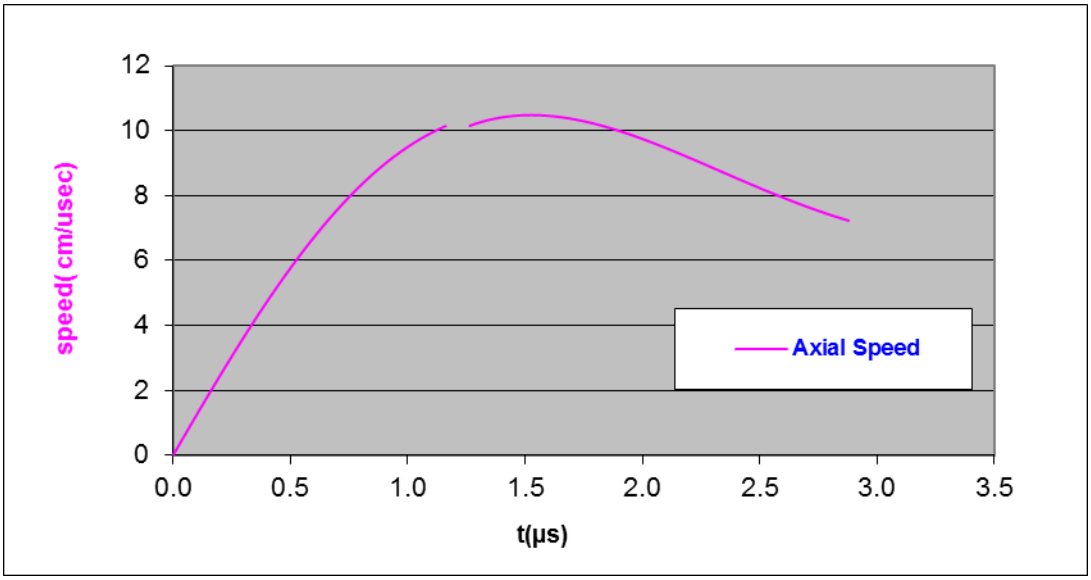

Fig. 3.2: The peak axial velocity about 10 cm/μsec under the operation conditions.

The simulation also shows that, in the pinch phase, the plasma density can reach 10^{17} ions/cm^3, and that the plasma temperature is about 1 keV, as can be seen in Fig. 3.3. The Lee model predicts: 10^{15} ions per shot, beam energy of 12 J, and beam current of about 15 kA, for the optimized operating condition of the device; the amount of energy that is transferred to the pinch is about 10 percent of the stored energy, and less than 10 percent of the stored energy in the focused plasma will be converted to ion beam energy, making 1% energy efficiency for ion beam production.

The parameters of the DPF UofS-I are listed in Table 3.1. It should be noted that the insulator material and length are two important parameters to be optimized experimentally in the device. In the DPF UofS-I, a Pyrex tube with 2 mm thickness is used as an insulator. The insulator length can be changed up to 7 cm to cover the whole anode length.

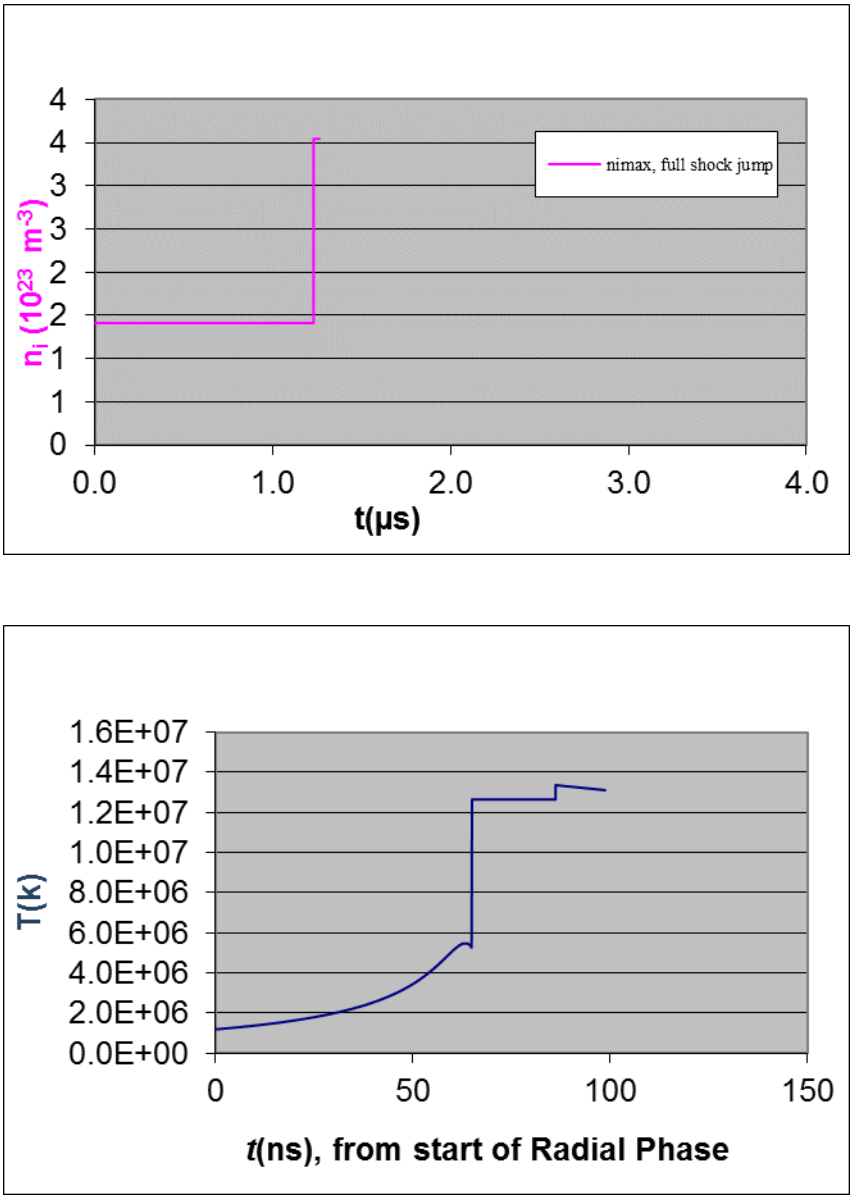

Fig. 3.3: The simulated plasma temperature and ion density in DPF UofS –I.

Table 3.1: The parameters of DPF UofS-I.

Parameter	**Value**
Capacitance (C_0)	4.9 μF
Inductance (L_0)	150 nH
Charging voltage (V_0)	18-30 kV
Stored energy (E_0)	2 kJ
Peak discharge current	140 kA
Anode radius (*a*)	1.5 cm
Cathode radius (*b*)	5 cm
Anode length (*L*)	7 cm
Insulator length (*d*)	3 cm
Insulator material	Pyrex
Electrodes material	Copper
Cathode type	rods
Number of rods	12
Operating gases	H_2, N_2, Ar
Operating pressure	0.1 to 5 Torr

3.3 Experimental Setup of DPF UofS-I

Fig. 3.4 shows the DPF UofS-I with a stored energy of 2 kJ that is built at the University of Saskatchewan. The DPF-UofS-I consists of a discharge tube and a vacuum chamber, a spark gap, a capacitor bank, a 30 kV power supply, and a trigger circuit. A Faraday cage was used for the oscilloscopes to record signals so the noises are minimized.

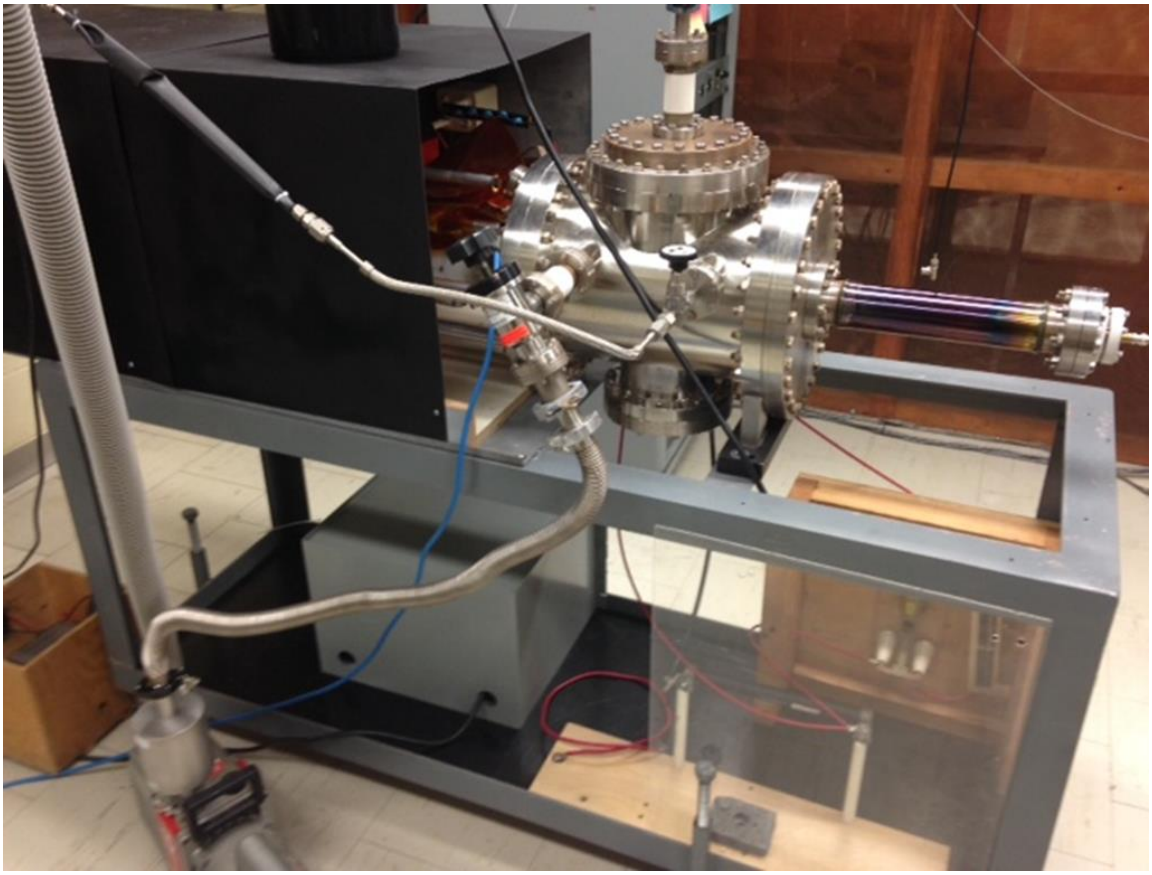

Fig. 3.4: The DPF UofS-I that was built in the University of Saskatchewan.

The schematic of the electrode assembly and the vacuum chamber of the DPF UofS-I can be seen in Fig. 3.5. The Faraday cup was placed on the top of the anode. The soft x-ray detector was placed on the side of the chamber to face the plasma column. A pinhole is placed in the opposite side of soft x-ray detector for visible imaging. Two ports were used for pumping and gas inlet in the chamber.

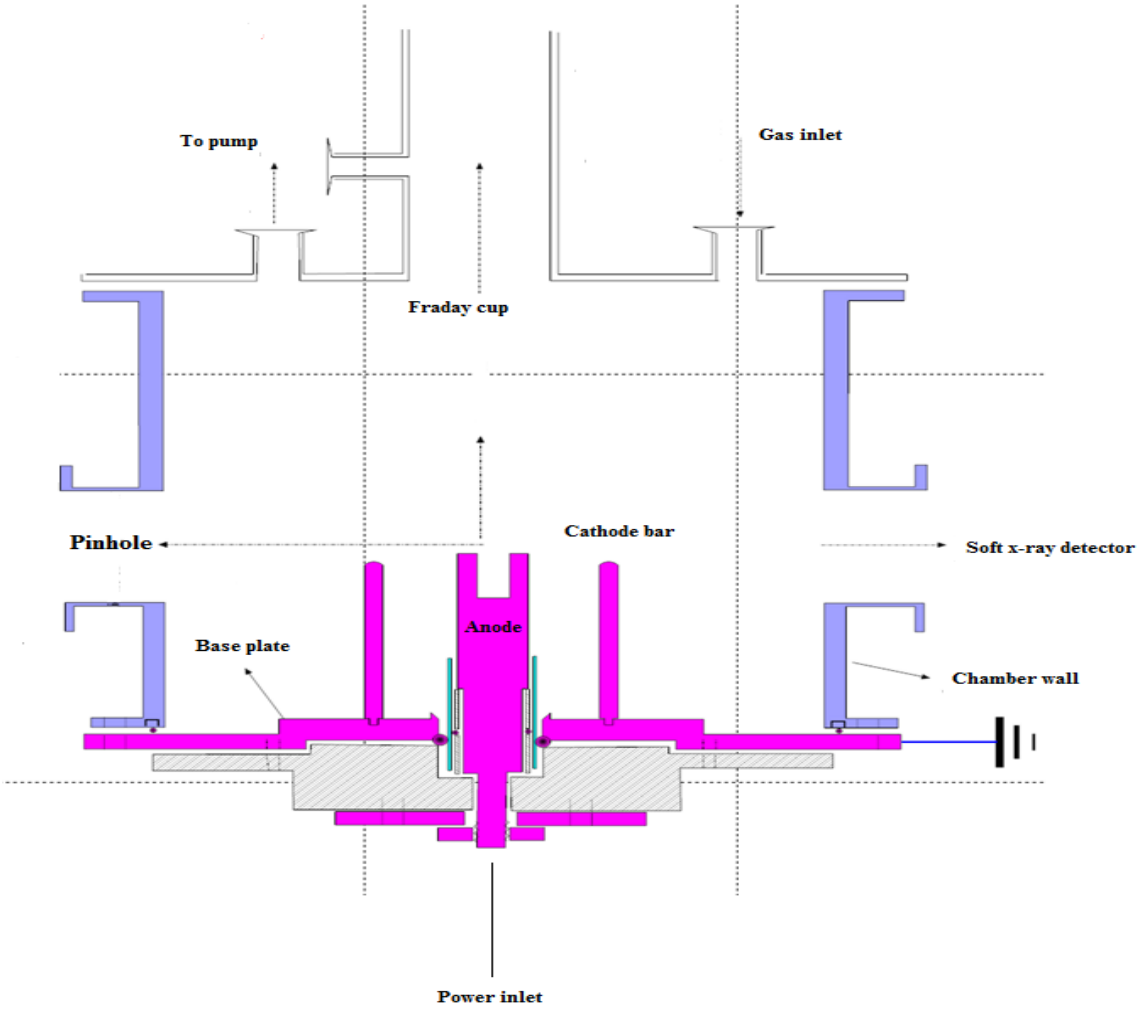

Fig. 3.5: The assembly of electrodes and detectors on vacuum chamber.

The discharge electrodes include 12 cathode bars surrounding the anode electrode. A knife edge (to form a uniform discharge around the insulator) was made on a copper plate for uniform formation of current in the break-down phase. The electrodes are made from copper and are isolated electrically by a Pyrex tube, as can be seen in Fig. 3.6.

Fig. 3.6: Electrodes and insulator configuration after thousands of shots inside the vacuum chamber.

A spark gap switch operating in high pressure was made to carry current from the capacitor to the discharge tube. The electrodes were designed in such a way that the gap between them can be changed. An SF6 gas and its pressure can be used to control the breakdown voltage of the spark gap. The electrodes are made of copper, and the housing of spark gap is made by Delrin plastic material to insulate the anode and cathode. A cylindrical plate was used as the trigger electrode. A negative pulse with a peak voltage up to 40 kV was used to trigger the spark gap. A high voltage transformer is used for electrical isolation of pulse generator from the capacitor bank. The schematic of the spark gap used in the DPF UofS-I can be seen in Fig. 3.7. The spark gap is placed in a symmetric configuration made by 8 cathode rods to reduce the inductance of the transmission line. The coaxial transmission line also reduces the discharge noise during the operation of the device. The capacitor and transmission lines were placed inside a grounded shielding box for safety issues, as can be seen in Fig. 3.4.

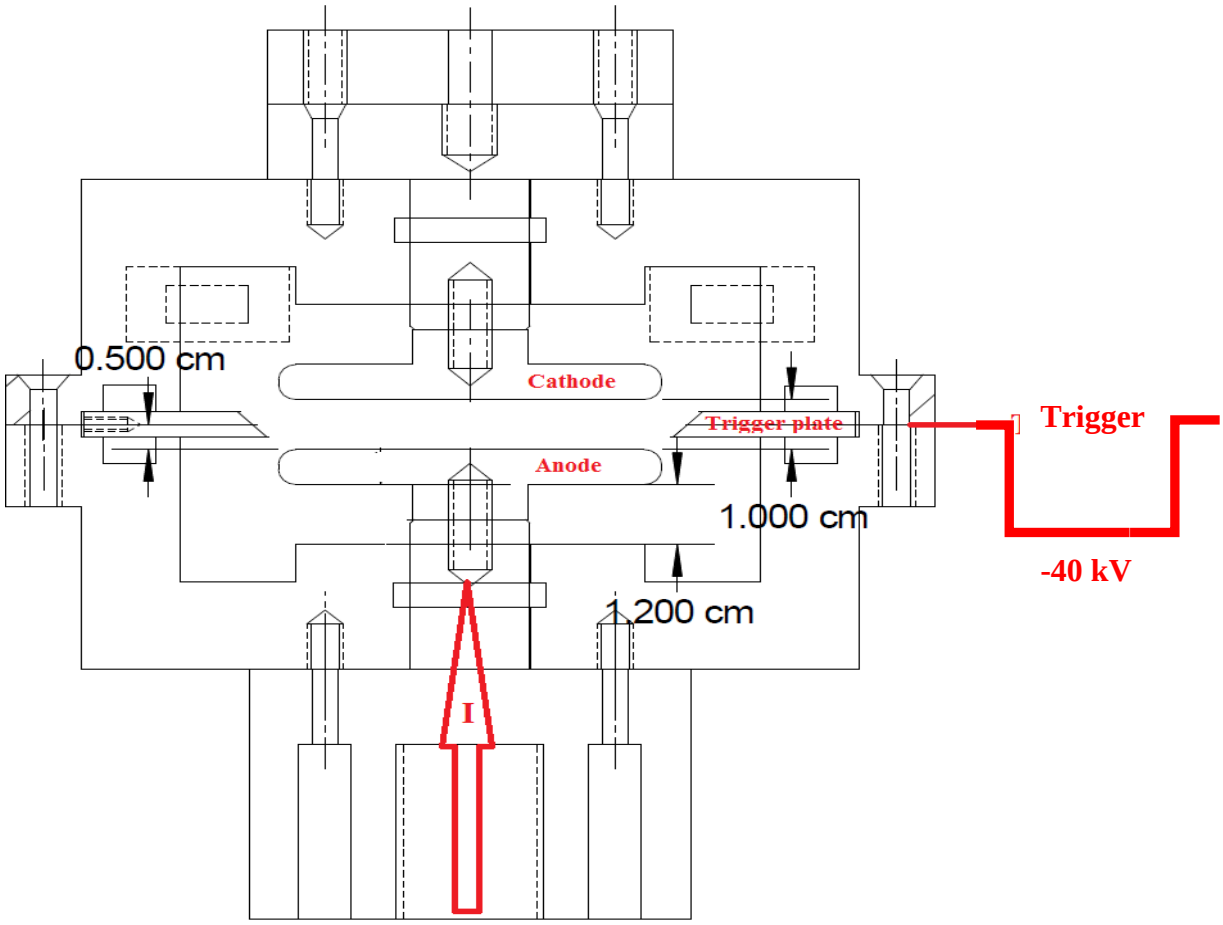

Fig. 3.7: The schematic of spark gap used in DPF UofS-I. The bottom part of e spark is connected to capacitor while the upper part of spark gap is connected to chamber.

For charging the capacitor, a 100 Ω charging resistor, along with a power supply, were used. The voltage can be set on the power supply, and the capacitor discharge through a spark gap by manual or automatic trigger switch is connected through an optical fiber to a trigger box. Discharging the capacitor bank can also been done manually by a high voltage relay connected to a mega-ohm resistance. The charging time of the device is about 30seconds, and the damping time

of the capacitor is about $RC \simeq 5$ min through the dump resistor. The high voltage relay and the damping resistance were tested up to 30 kV.

To evacuate the chamber, a two-stage rotary pump has been used to attain a low, ultimate pressure of 10^{-3} mbar. A vacuum gauge was used to monitor the background and filling pressures.

All signals from the device were transmitted through 50 Ω coaxial cables to the Faraday cage. Three Tektronix oscilloscopes (model 2014 c) with USB ports were used to record all signals simultaneously. All oscilloscopes were trigged by a discharge trigger signal. To operate the DPF UofS-I, the following steps are required:

1. Pumping the vacuum chamber by a rotary pump up to 10^{-3} Torr.
2. Filling the vacuum chamber with gas up to operating pressure.
3. Charging the capacitor bank.
4. Trigging the spark gap to discharge the capacitor.
5. Closing the discharge relay to clear the residual charge in the capacitor.

A Faraday cage that was set up in the plasma focus lab is used for the shielding of electromagnetic pulse (EMP) generated during the capacitor discharge. The Faraday cage was made of copper mesh and was grounded to effectively reduce the electromagnetic noise level. Copper is a good conductor that absorbs high frequency electromagnetic noise. To prevent a ground loop, the Faraday cage is connected to the DPF device on a single point.

Finding the optimum experimental charging voltage and filling pressure of the device to produce a strong focusing is the most important step for running a plasma focus device. Changing the operating gas can change the operating charging voltage and pressure. As mentioned earlier,

argon, nitrogen, and hydrogen are used as the operating gases. The operating conditions of the DPF UofS-I in different gases can be seen in Table 3.2.

Table 3.2: The operating conditions of DPF UofS-I.

Operating gas	**Charging voltage (kV)**	**Operating pressure (Torr)**
Argon	15- 28	0.1 - 0.5
Nitrogen	15-28	0.1 - 0.7
Hydrogen	15-28	1 - 6

It should be noted that operating the DPF UofS-I in light and heavy gases is a unique feature of the device as it is a low energy device.

Fig. 3.8 shows the discharge current (*I*) and anode voltage (*V-Anode*) of DPF UofS-I operating in argon gas. The drop of the current and the peak of the anode voltage shows the pinching effect. As can be seen in Fig. 3.8, the duration of the current drop is about 500 ns, and anode voltage shows two main peaks. The discharge current shows a 50 percent drop during the final stage of the plasma focus, indicating a very strong pinch result.

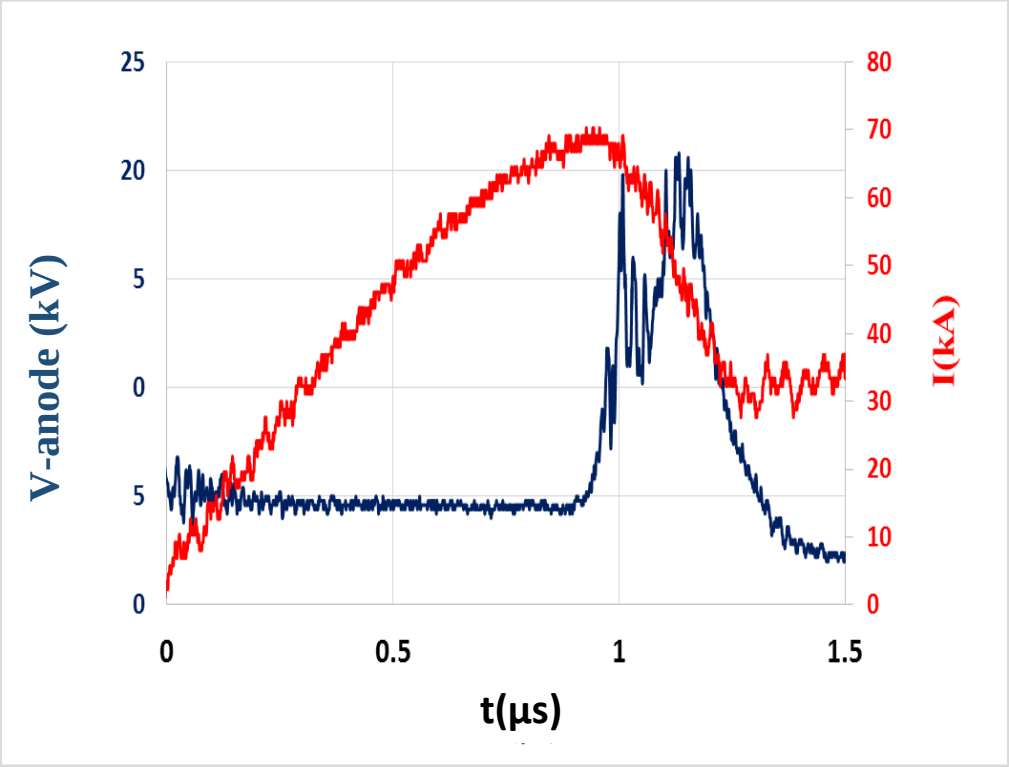

Fig. 3.8: The focusing effect of DPF UofS-I operating in argon gas. V =28 kV, P=0.1 Torr.

Chapter 4
DPF UOFS-1 DIAGNOSTICS

4.1 Introduction

In order to study the time-resolved signals of the charged particles and x-rays from the pinching plasma, different detectors, such as an ion beam detector, electron beam detector, a soft x-ray detector, and hard x-ray detector, had to be developed. The main goal in developing these detectors is to measure the flux (number per shot) and the energy spectrum of the ions, the energy spectrum of radiated soft and hard x-rays, and electron beam current. As mentioned in the previous Chapter, the DPF UofS-I is developed as an ion source. In order to find the best operating condition of this device to produce energetic ions, the combination of the ion beam, electron beam, and x-ray detectors are also required. Plasma temperature is another important parameter to be measured during the compression phase. The measurement of plasma temperature can be done by soft x-ray spectroscopy.

Another important part, regarding the ion beam production, is related to the optimum operating parameters to increase the flux and energy of the charged particle beams from the device, which can be understood by considering the correlation of the energetic ion beam emission with the x-ray and electron beam emission from the device. In this chapter, charged particles and x-ray diagnostics that were developed and used in the DPF UofS-I will be described, and the technical details will be presented.

4.1.1 Discharge Current and Anode Voltage Probes

In general, to measure the discharge current derivative, a fast Rogowski coil can be used in a plasma focus. The current that pass through the coil induces a voltage across the coil, as can be seen in Fig. 4.1. R_C and L_C are the resistance and inductance of the coil, respectively. R is the external resistance that is connected to the coil. Rogowski coils is a solenoid tightly wound on a flexible form so it can be bent to let the two ends meet. Rogowski coils can be either work as a self-integrator, or can be connected to a proper external integrator to measure the current. When a Rogowski coil is used as a self-integrator, the output of the coil is proportional to discharge current.

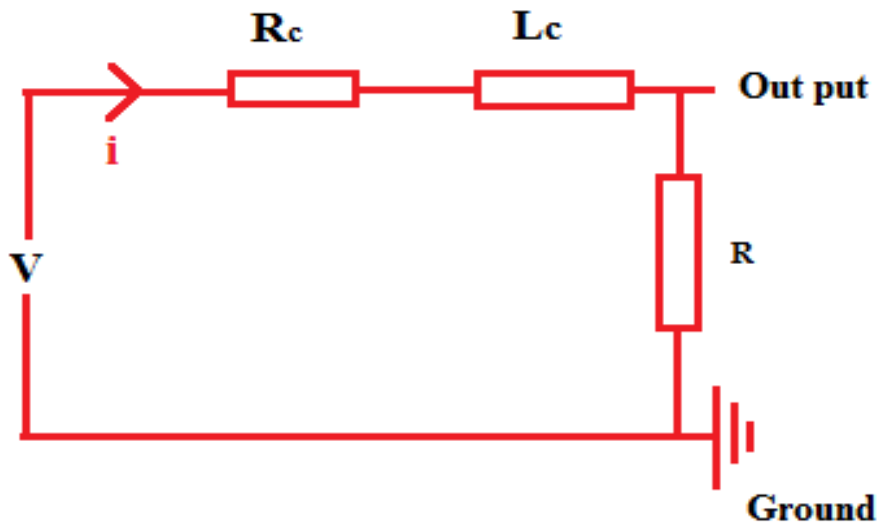

Fig. 4.1: Rogowski coil equivalent circuit.

The voltage across the coil can be presented by Eq. 4-1, where I is the discharge current and i is the current passing through the Rogowski coil.

$$L_c \frac{di}{dt} + (R + R_c) i = k \frac{dI}{dt} \tag{4-1}$$

Eq. 4-1 shows that if $L_c \frac{di}{dt} >> (R + R_c) i$, the output of the coil is given by Eq. 4.2 where the Rogowski coil works as a self-integrator coil.

$$V_{out} = Ri = R\left(\frac{k}{L_c}\right) I \tag{4-2}$$

If $(R + R_c) i >> L_c \frac{di}{dt}$, then the output of the coil can be shown by Eq. 4-3, where an external integrator is needed for measuring the discharge current.

$$V_{out} = R\ i = \left(\frac{Rk}{R + R_c}\right) \frac{dI}{dt} \tag{4-3}$$

In DPF UofS-I, a commercial Pearson fast current probe (with a response time less than 1 ns) was used to measure the discharge current. The current probe was connected to the ground side and is insulated from the high voltage.

To measure the anode voltage, a fast Tektronix high voltage probe (P6015-A) with a maximum operating voltage of 40 kV and response time of 2 ns was connected to the anode. The current probe and high voltage probe can be seen in Fig. 4.2.

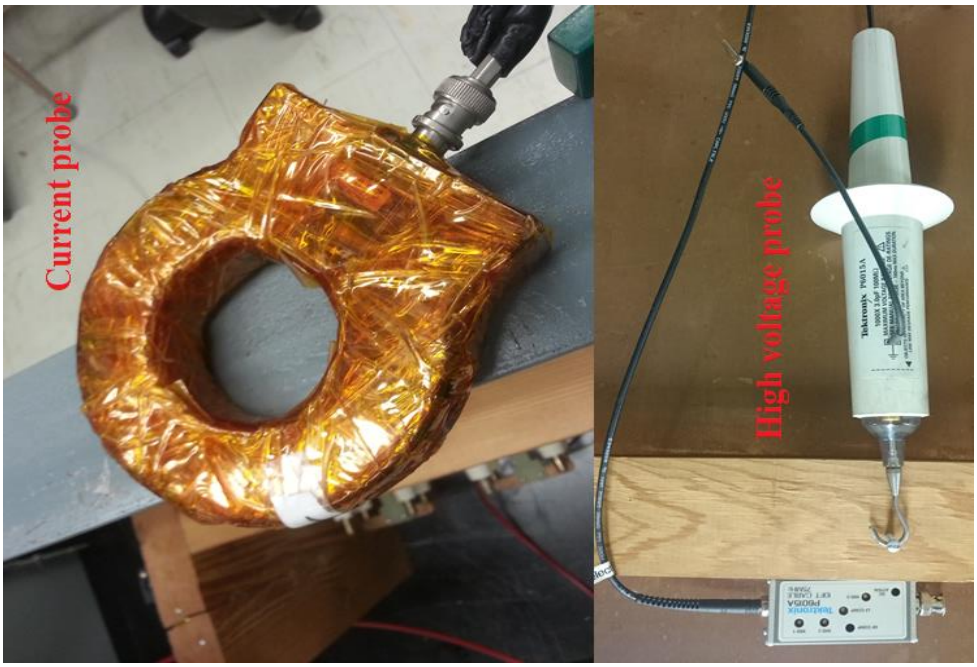

Fig. 4.2: The current probe and high voltage probe were used in DPF UofS-I.

4.1.2 Faraday Cup

One of the first detectors that has been built is a Faraday cup, which works in the secondary electron emission (SEE) mode. The cup has been made for collecting ion beams, and has been designed and biased for minimum possible noise ratio and good impedance matching. It should be noted that the Faraday cup is a useful detector to measure the ion beam flux. In order to measure the energy of the ion beam based on the time of flight measurement, a configuration with a Faraday cup and an x-ray detector are required.

Based on the time-of-flight (TOF) method, the kinetic energy of ion beam can be estimated by measuring the velocity and mass of a charged particle. The velocity is equal to the distance between plasma region and the faraday cup position divided by the interval time between the peak of the hard x-ray signal (onset of ion beam emission) and the peak of ion beam signal. Fig. 4.3

shows the Faraday cup assembly used in DPF-I. The Faraday cup was placed 75 cm away from the pinching plasma. A pinhole with 500 microns in diameter was used to attenuate the ion beam intensity before reaching the cup.

The inner cup was made of copper and an aluminum cage was used for EMP shielding. The impedance of the cup based on the geometry of inner and outer cup was chosen to be matched with the 50 Ω coaxial cable to avoid a pulse reflection.

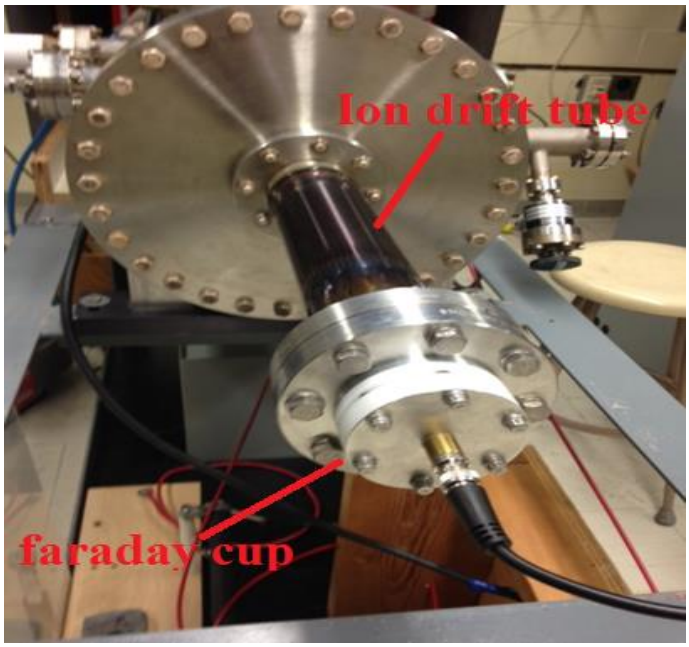

Fig. 4.3: The Faraday cup assembly used in DPF-I.

The configuration of the Faraday cup can be seen in Fig. 4.4. The inner cup is negatively biased to -1000 V. A cylindrical insulator (Teflon) was used to insulate the inner and the outer cup.

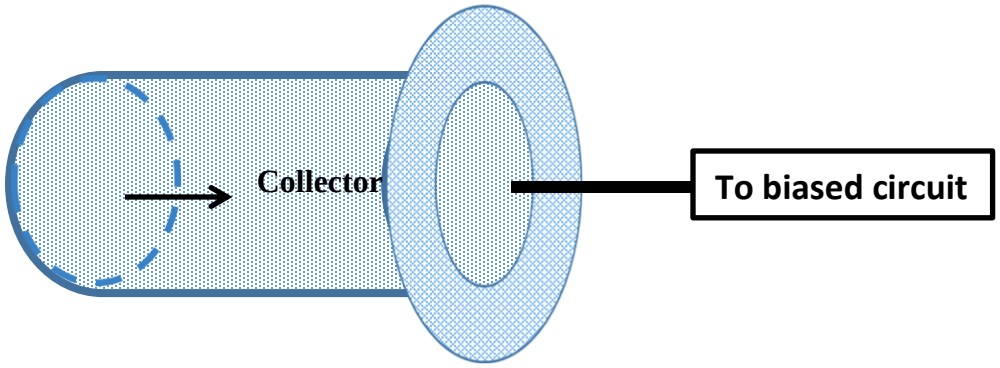

Fig. 4.4: The configuration of Faraday cup was used to monitor the generated ion beam.

The typical signals of the ion beam current (*IB*) and the discharge current (*I*) can be seen in Fig. 4.5. The duration of the beam is about 100 ns.

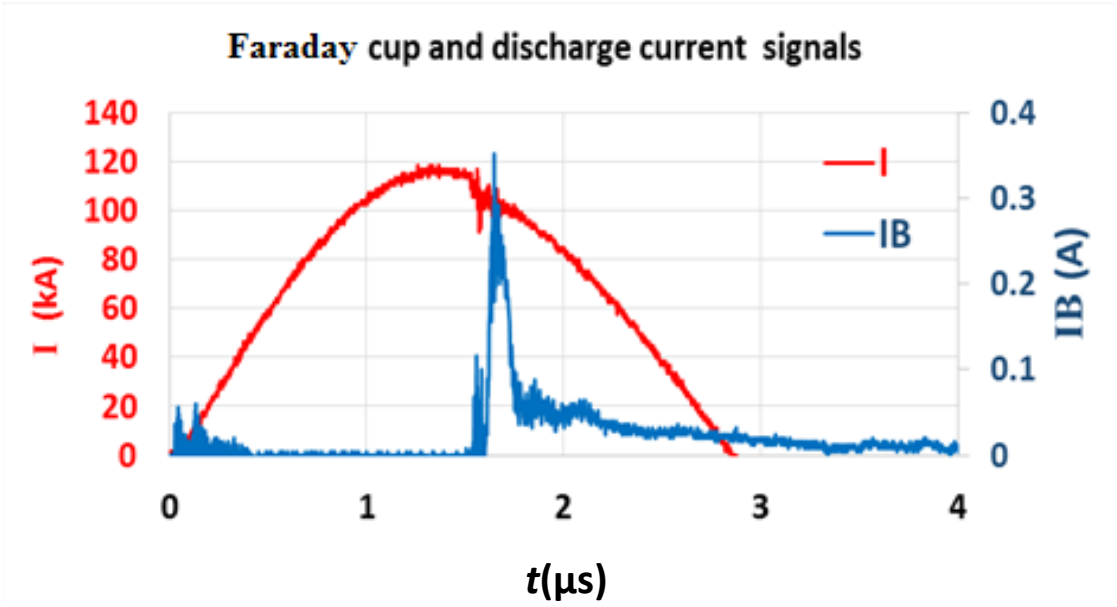

Fig. 4.5: Ion beam current (IB) and discharge current (I) signals.

To measure the ion current, the Faraday cup signal has to be converted from a voltage signal to a current signal. The output signal of the cup is the voltage across a 50 Ω resistance. The

current signal (*IB*) can be expressed by $IB = \frac{dQ_{Total}}{dt}$, where Q_{Total} is the charge collected by the Faraday cup.

The total collected charge by the cup can be presented by Eq. 4-4, where *dq* is the number of the secondary electrons that is produced by the interaction of energetic ions by the inner cup, *k* is the escape factor of a secondary electron from the inner cup, and *dQ* is a total charge of the ions. The escape factor is equal to the ratio of the radius to the length of the collector. The ion collector is usually negatively biased to push the secondary electron out of the cup.

$$dQ_{Total} = dQ + kdq \tag{4-4}$$

The number of secondary electrons (*g*) produced by the interaction of the energetic ion with the collector can be calculated based on the energy of the ion and the incident angle of the ion with respect to the normal of the collector surface. The coefficient *g* is called the electron stopping power, and can be expressed by Eq. 4-5, by considering the electron stopping power as $(dE/dx)_e$ and θ as the incident angle of ion.

$$g = \frac{\Lambda}{\cos\theta}\left(\frac{dE}{dx}\right)_e \tag{4-5}$$

The coefficient, Λ, depends on the material of the collector. The value of Λ given for copper is 0.22 Å/eV, based on the SRIM software.

By considering the charge and energy of the incident ion *(Z(E))*, *kdq* can be expressed by Eq. 4.6.

$$kdq = dQ\ (\frac{k\,g}{Z(E)}) \tag{4-6}$$

By considering $dQ = dN\ e\ Z(E)$ where e is charge of electron, and dN is the number of ions with an energy between E and $E+dE$, dQ_{Total} can be expressed by Eq. 4-7.

$$dQ_{Total} = dQ\left(1 + \frac{k\,g}{Z(E)}\right)\left(1 + \frac{k\,g}{Z(E)}\right) = dN\ e\ Z(E)\left(1 + \frac{k\,g}{Z(E)}\right) \tag{4-7}$$

By using Eq. 4-6, the total current that is measured by the cup can be expressed by Eq. 4-8

$$I = \frac{dQ_{Total}}{dt} = \frac{dN}{dt}\ e\ Z(E)\left(1 + \frac{k\,g}{Z(E)}\right) \tag{4-8}$$

By using the chain rule $\frac{dN}{dt} = \frac{dN}{dE}\frac{dE}{dt}$,$E_{Ion} = \frac{1}{2}m\ \times v^2$, and $v = L/t$ where L is distance between the ion collector and pinching plasma , Eq. 4-8 gives

$$I = \frac{dQ_{Total}}{dt} = \frac{(2E)^{\frac{3}{2}}}{L\,M^{\frac{1}{2}}}\ e\ Z(E)\left(1 + \frac{k\,g}{Z(E)}\right)\frac{dN(E)}{dE} \tag{4-9}$$

Eq. 4-9 can be used to find $\frac{dN(E)}{dE}$ versus the ion energy by using the *IB* signal, the mass of ion, the charge of ion, and the distance of the Faraday cup from the pinch. To use Eq. 4-9 to plot $\frac{dN(E)}{dE}$ -*E* one needs to convert *IB* –*T* to *IB*-*E*. In the following chapter, the *IB*-*E* plot will be presented for different operating gases.

Optimization of a Faraday cup can be done by biasing the voltage, adding a magnetic field, and reducing the photoelectric effect. The beam loss effect due to the interaction of the ion beam with the background gas is another issue that can be resolved by reducing the pressure inside drift tube. It should be noted that measuring the exact number of ions generated from the pinching plasma is an unsolved technical problem.

4.1.3 Electron Beam Measurement

A plasma focus is an energetic electron beam source. The electron beam current can reach to several kA, and the energy of the electrons can reach up to MeV. The duration of the electron beam generation is on the order of 100 ns in a plasma focus. Due to the generation of the electron beam in a short period of time, a fast Rogowski coil is required to monitor the electron beam current.

To extract the electron beam from plasma focus, a hollow anode has to be used. The hollow anode has to be connected to the drift tube and a current probe, which ensure the electron beam current to pass through the tube. A Pyrex tube was used to extract the electron beam from the bottom of the hollow anode. The distance between the collector and pinch is about 30 cm. To avoid a discharge of the capacitor bank through electron beam collector, a 5 Ω resistance has been used in the ground side of the collector. A Faraday cup can be biased negatively to measure the energy of the electron. An electron with an energy less than the biased voltage cannot reach the cup.

A self-biased Faraday cup is another method to measure the electron energy. In this method, a resistance R can cause a negative voltage by passing the electron current through the resistance (i.e. $V=R\,I_{\text{E-beam}}$). Adding filters to block the low energy electrons is another method to distinguish the low energy and high energy electrons generated from the pinching plasma. The energy spectrum of the radiated hard x-ray can also give a good estimation of the energy of the generated electron by the pinching plasma. A correlation of the ion and electron beams can give an idea about possible mechanisms of electron beam generation from the pinching plasma.

Figure 4.6 shows the typical signal of an electron beam (*I-E-beam*) generated from the DPF UofS-I. The duration of the beam is about 100 ns. The electron current can reach up to 2 kA in DPF UofS-I. It should be noted that DPF UofS-I is a unique low energy device in terms of having these charged particle detectors.

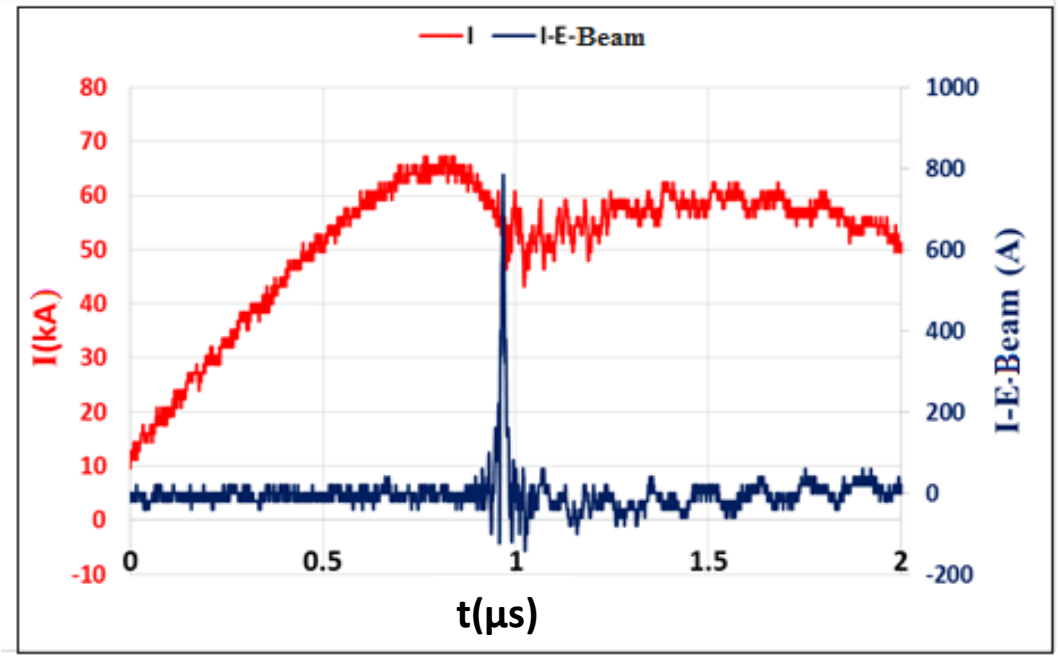

Fig. 4.6: A typical signals of electron beam (I-E-beam) generated from DPF UofS-I.

4.1.4 Hard X-ray Measurement

In a plasma focus device, hard x-rays are generated due to bombardment of the anode tip by energetic electrons. The duration of hard x-ray radiation in a plasma focus is about 100 ns. Hard x-rays can be detected by a plastic scintillator in front of a photo-multiplayer tube (PMT). Two hard x-ray detectors were made in this project to detect the generated x-rays from the device. The

detectors were placed inside a Faraday cage three meters away from the pinching plasma. A 1cm stainless thick steel plate was used to filter the hard x-rays.

The PMT tube can be biased negatively up 1600 V. Increasing the biased voltage will intensify the signal of the hard x-rays. The delay time between the hard x-ray detectors is about 30 ns measured in the lab. Figure 4.7 shows the typical signal of the hard x-ray from DPF UofS-I.

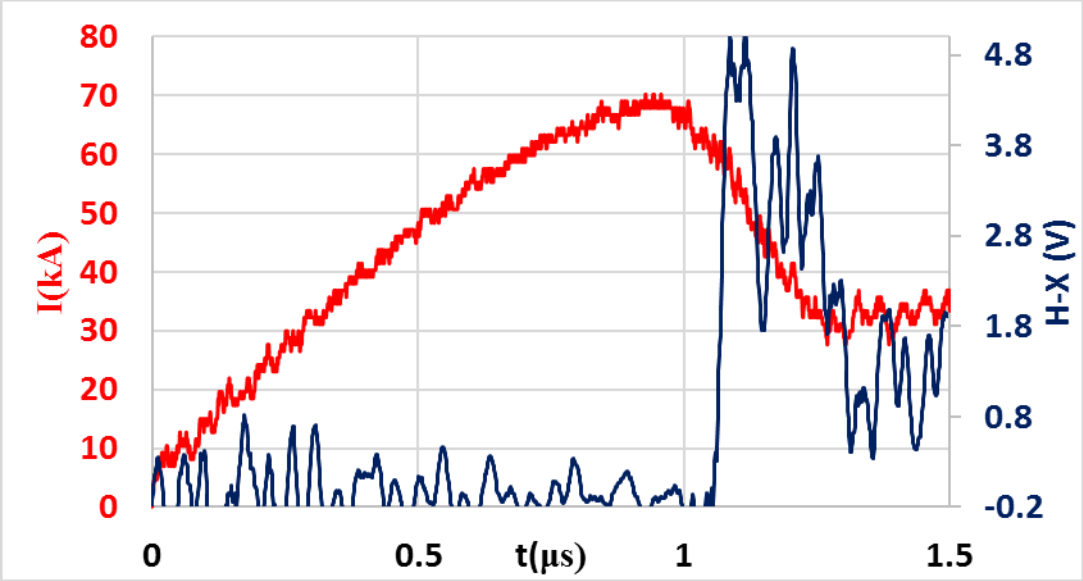

Fig. 4.7: The typical signals of hard x-ray from DPF UofS-I.

4.1.5 Soft X-ray Measurement

The definition of soft and hard x-rays is based on the energies of the x-ray. In general, in a plasma focus, the x-ray energy less than 4 keV is considered as soft x-ray. The energy spectrum of the radiated x-ray from the pinching plasma gives an idea about the energy of an electron and stage of ionization of atoms inside the plasma column. The number of ionization of atoms inside

the plasma column gives an estimation of the plasma temperature during the compression of the plasma.

To measure the energy spectrum of the radiated x-rays from DPF UofS-I, two diode based x-ray spectrometers were developed. Aluminum, cobalt, titanium, and beryllium filters, with different thickness, were used to measure the energy spectrum of the x-ray. The proper filters can be chosen by considering the operating gas.

To build the diode based x-ray spectrometer, four fast photodiodes (BPX-65) with a response time of less than 1 ns were biased negatively to about -50 volts. Figure 4.8 shows the biasing circuit of the BPX-65 diode. A 10 pF capacitor has been used to filter the noise.

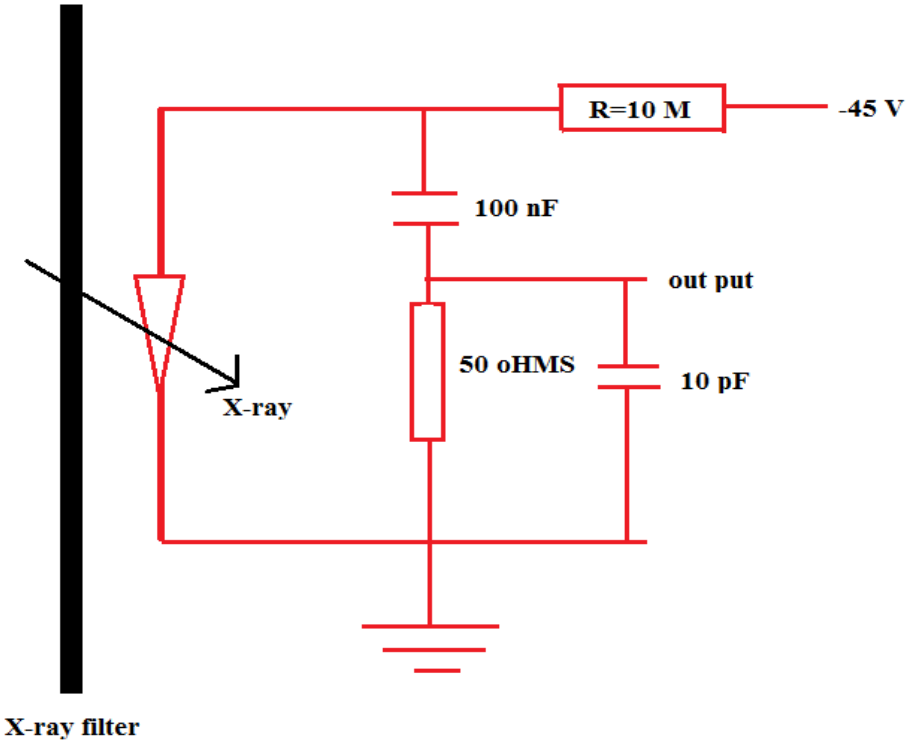

Fig. 4.8: The biasing circuit of BPX-65 diode.

The radiated x-rays with energy less than 30 keV can be absorbed by the active layer of the diode. Absorption of x-rays by diodes produces electron holes (i.e. empty place of an electron) that can carry current. It should be noted that the BPX-65 photodiode response is almost constant to the energy-spectrum of soft x-rays between 0.5 keV to 4 keV, and reaches its maximum in that same range. Therefore, the output of diodes can give an estimation of the number of photons that is absorbed by a diode in that range. Figure 4.9 shows the sensitivity of the BPX-65 diode to the energy spectrum of x-rays between 0.5 keV to 4 keV (i.e. $0.3\ \text{nm} < \lambda < 2\ \text{nm}$).

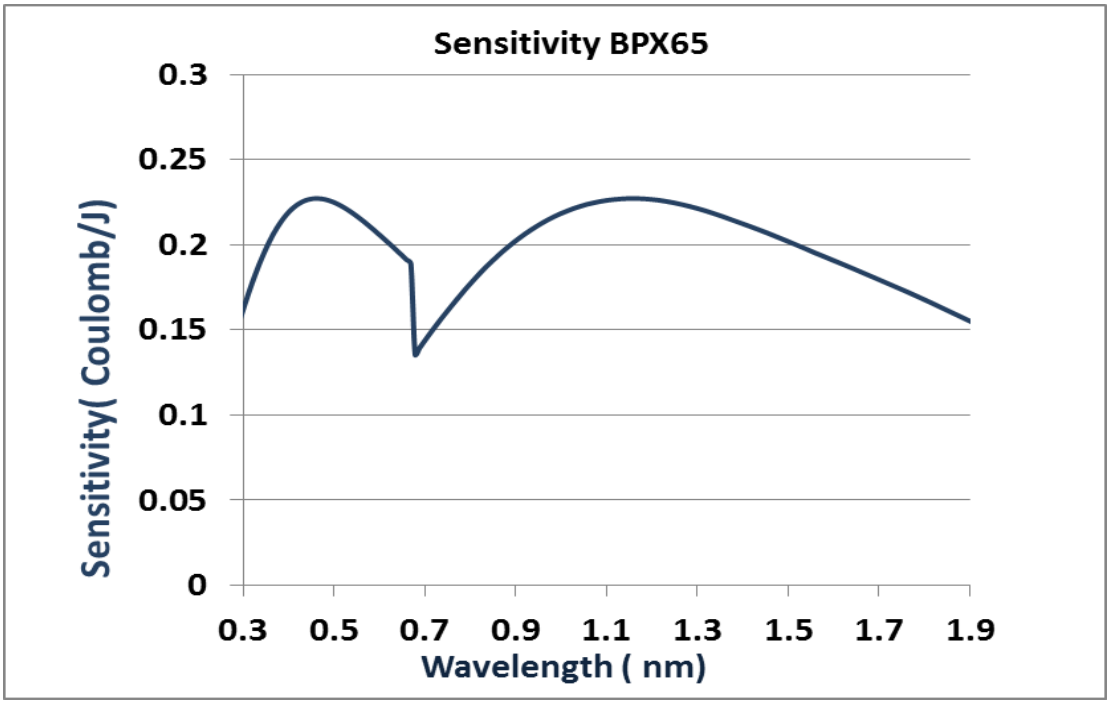

Fig. 4.9: The sensitivity of BPX-65 respect to energy spectrum of x-ray.

In a plasma focus, the copper K-lines have a significant contribution to the radiated x-rays from the pinching plasma. The energy of the copper K-lines is about 8keV. The sensitivity of the

BPX-65 diode is about 0.02 C/J in that range, which is not significant compared to the sensitivity of the BPX 65 diode in the energy range of 0.5 keV to 4 keV, as can be seen in Fig. 4.9.

The total sensitivity of the detector can be calculated based on the transmission of the filters, the gas, and the sensitivity of the diode. To convert the signal from the diode to energy, the following steps have to be considered.

1. The voltage from the oscilloscope should be converted to current by dividing the voltage by 50 Ω output resistance.
2. The total charge has to be calculated by integration of the current over time.
3. The total charge should be divided by the sensitivity of diode in the particular wavelength that is absorbed by the diode.

The area of the diode is about 1 $mm^{2.}$ The total energy of the radiated x-ray from the pinching plasma can be calculated by Eq. 4-10, where *r* is diode distance from the pinch in mm. The distance of diodes from the pinch is about 40 cm.

$$E_{Total} = E_{Absorbed\ by\ diode} \times 4\pi r^{2} \qquad (4\text{-}10)$$

The two soft x-ray detectors with 8 active channels were connected to the chamber on the top and on the side of the chamber. The detectors were isolated from the chamber by a ceramic break to break the ground loop and to reduce the noise from the pinch. Fig. 4.10 shows the two soft x-ray detectors that were connected to the chamber. Numbers 1 and 2 show the side and top side detectors, respectively.

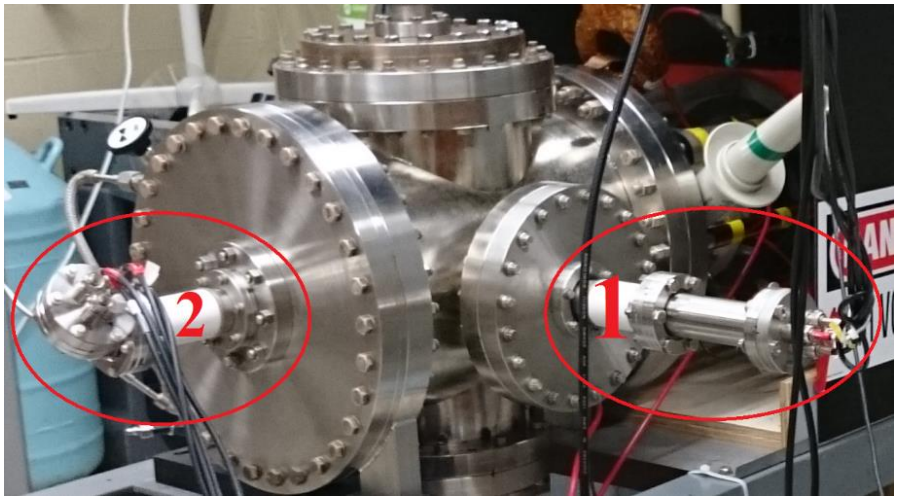

Fig. 4.10: The two soft x-ray detectors were used in DPF UofS-I.

The typical signal of the soft x-ray detector from one channel of soft x-ray detectors can be seen in Fig. 4.11. The duration of the x-ray signal is about 300 ns.

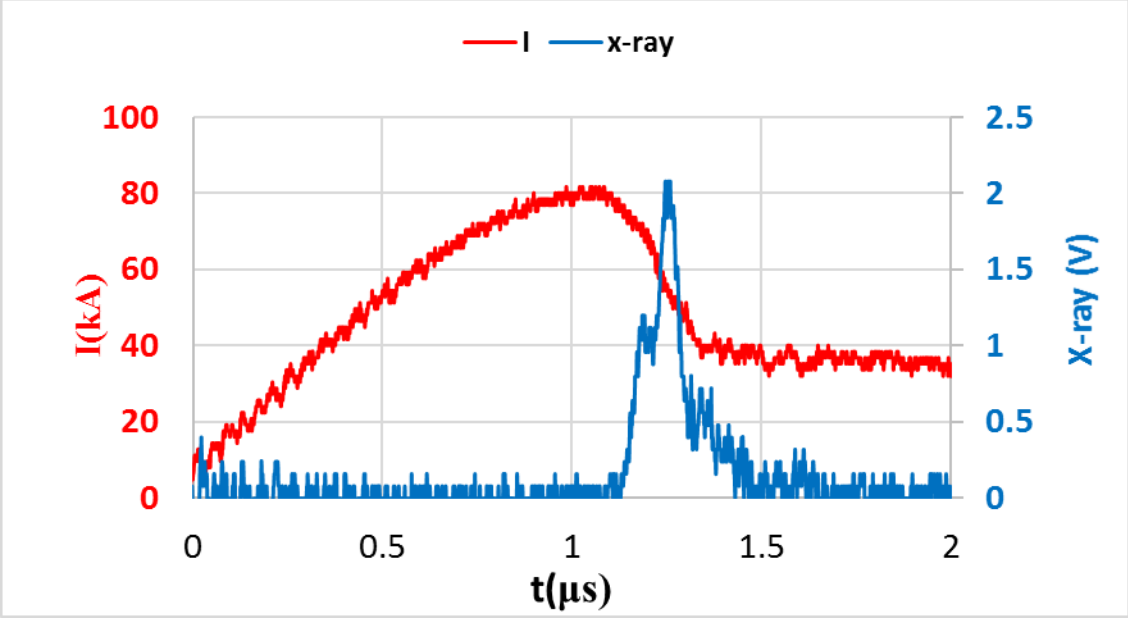

Fig. 4.11: The soft x-ray signal from DPF UofS-I.

Moreover, the plasma temperature measurement based on the ratio method is one of the significant data that has been obtained by soft x-ray spectroscopy in DPF UofS-I.

4.1.5 Signal Recording System

All signals from the ion beam detector, electron beam detector, hard and soft x-ray detectors, along with the discharge current and anode voltage, were recorded with three oscilloscopes. The three digital storage oscilloscopes (Tektronix, 2014 C model) were triggered at the same time at the start of the discharge current.

All signals were stored in a USB connected to each oscilloscope in excel format. A standard 50 Ω coaxial cable was used to transfer signals from the sensors on the device to the Faraday cage.

Chapter 5

EXPERIMENTAL RESULTS AND DISCUSSION

5.1 Introduction

In this chapter, the experimental results on charged particle emission and x-ray radiation will be presented. In the first part, the effect of the atomic number of gas on x-ray radiation and ion beam emission will be presented. Based on the measured plasma inductance, the effect of the atomic number of gas on the compression of plasma will also be discussed. The measured ion energy and ion current density will be compared with the plasma voltage. The ion current density generated from the pinching plasma will be compared with the Lee model.

In the second part, by analyzing the electrical signals, a new method to estimate the plasma resistance in a plasma focus device will be introduced. Anomalous plasma resistance is one of the main mechanisms of the energetic charged particle generation from a pinching plasma. The effect of the atomic number of the gas on the occurrence of anomalous resistance will be discussed. To measure the plasma resistance, the plasma voltage and inductance will be derived by analyzing the waveforms of the discharge current and the anode voltage of the device.

In the third part, the required electric field to generate runaway charged particles from the pinching plasma will be discussed. The Dreicer theory and the avalanche process will be discussed. By measuring the plasma voltage and inductance, the electric field across the plasma column for

runaway charged particle generation will be calculated and compared with the Driecer electric field. The time rate of the runaway electron generation will be calculated in a plasma focus. The effect of anomalous heating on a required electric field for runaway charged particle production will be studied experimentally. By using soft x-ray spectroscopy, anomalous heating in the post pinch-phase will also be shown experimentally.

In the last part of this chapter, a new type of a DPF device with semi-active electrodes (DPF-SAE) will be introduced. Technical details of an SAE-type plasma focus will be presented. The electrical discharge signals of the device will be analyzed. The generation of charged particles and x-rays from the device will be investigated. The results corresponding to the charged particles and x-ray radiations from a DPF-SAE and DPF UofS-I will be compared.

5.2 Charged Particle Emission in Light and Heavy Gases

In this experiment, the generation of charged particles and x-rays from argon, nitrogen, and hydrogen plasma will be presented. Different observed regimes of the focusing in the operating gases will be discussed. The energy spectrum of the ion beam in three operating gases will be presented and compared with the measured plasma voltage. The change in plasma inductance will be measured by analyzing the discharge current and anode voltage.

Fig. 5.1 shows the different regimes of the focusing exhibited in the typical signals of the discharge current and high voltage probe signals in argon and hydrogen gases. As can be seen, the duration of the current drop and the peak of anode voltage in argon gas is about 400 ns. In the case of hydrogen, the duration of the discharge current and the anode voltage is about 100 ns. These features have been observed in all operating pressures of the device in argon and hydrogen gases. The long duration of x-rays and ion beams have been observed in argon gas, and have been

compared to the hydrogen and Nitrogen gases. Table 5.1 shows the duration of ion beams and x-rays generated from the DPF UofS-I in the three operating gasses.

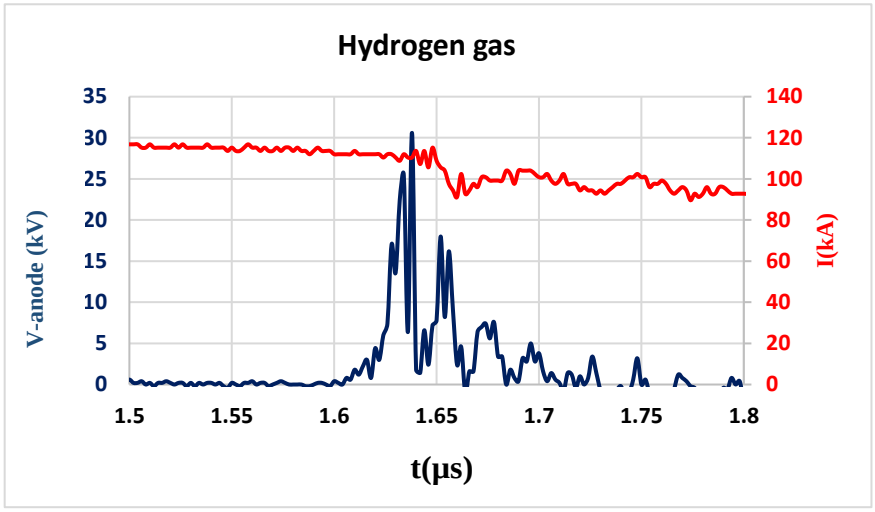

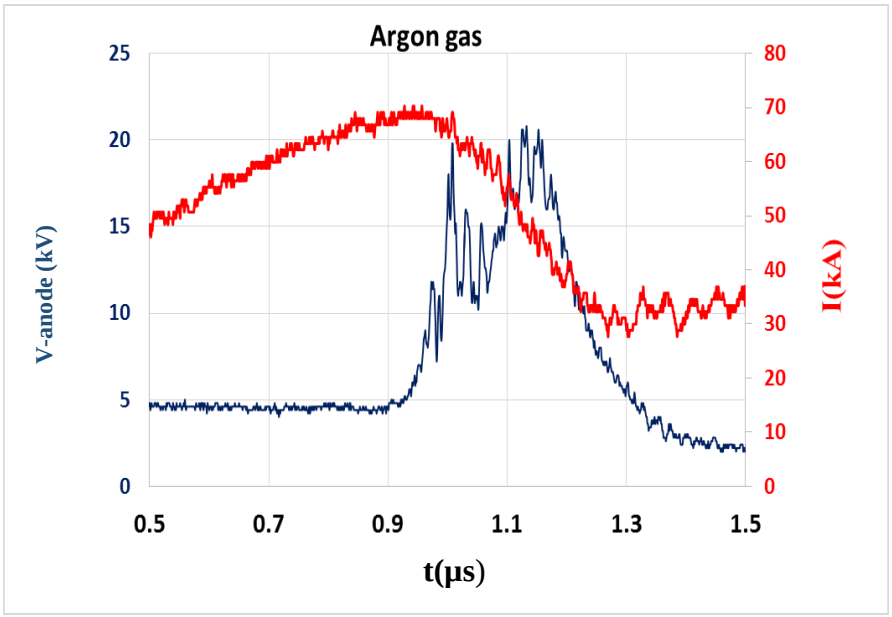

Fig.5.1: The different regimes of focusing in argon and hydrogen gasses.

Table 5.1: The main features of the experimental observations for plasma foci operating in argon and hydrogen gasses.

Operating GasGas	Hydrogen	Nitrogen	Argon
Operating Pressure (Torr)	4 – 6	0.1-0.6	0.1- 0.5
dI/dt (A/s)	$\leq 8\times10^{11}$	$\leq 6\times10^{11}$	$\leq 1.2\times10^{12}$
Current drop (kA)	≤ 15	≤ 30	≤ 60
Anode Voltage (kV)	≤ 30	≤ 30	≤ 45
Current drop duration (ns)	≤ 50	≤200	≤ 300
Hard x-ray duration(ns)	≤ 20	≤ 50	≤150
Charged Particles duration (ns)	≤ 100	≤ 200	≤ 250
Soft x-ray duration(ns)	Noise level	≤150	≤300

The waveforms of the discharge current and anode voltage of the DPF UofS-I can interpreted by a circuit analyses [73-78]. The tube voltage can be calculated through the discharge current and anode voltage, based on Eq. 5-1, where $V_A(t)$ is the anode voltage, $I(t)$ is the discharge current, R_{Pl} is the plasma resistance, and L_0 is the inductance of the discharge circuit from the voltage probe to the discharge electrodes. Considering that $L_0 = 40\ nH$, the tube voltage can be expressed by Eq.5-1.

$$V_{Tube}(t) \simeq IR_{Pl} + \frac{d}{dt}[L_{tube}\ (t)I(t)] \simeq V_A(t) - (\ L_0)\ \frac{dI}{dt} \qquad (5\text{-}1)$$

The power into the discharge tube can be calculated by $V_{Tube}(t)I(t)$. Figure 5.2 shows the tube voltage in argon gas corresponding to the anode voltage and the discharge current in Fig. 5.1. Numbers 1 and 2 correspond to the pinch and post-pinch phases.

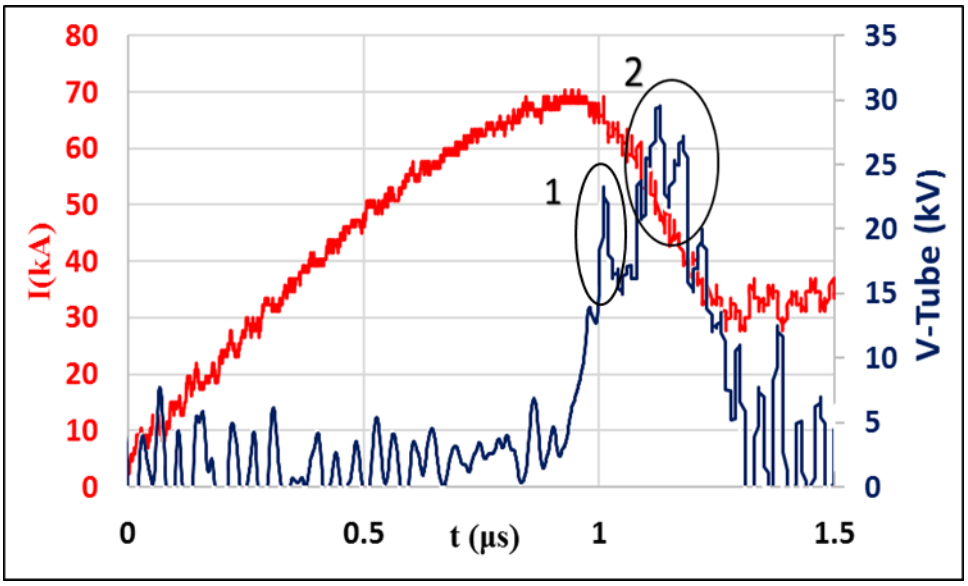

Fig. 5.2: Discharge current and tube voltage in argon gas during the compression phase.

Since the inductance of the electrode is about 12 nH, the voltage across the plasma in the compression phase can be calculated by assuming L_0 = 52 nH (i.e. inductance of the discharge circuit from the voltage probe to the tip of the discharge electrodes). The estimated voltage across the plasma column during the pinching time reaches up to 65 kV in hydrogen, 57 kV in nitrogen and up to 100 kV in the argon plasma.

The tube inductance can be calculated by measuring the tube voltage and the discharge current by Eq.5-2, where t_0 is the start time of the discharge.

$$L_{Tube}(t) = \frac{\int_{t_0}^{t}[V_{Tube}(t) - I(t)R_{Pl}(t)]dt \; + \; L_{Tube}(t_c)\, I(t_c)}{I(t)} \qquad (5\text{-}2)$$

Fig. 5.3 shows the typical measured change in tube inductance in hydrogen gas. The rapid change in tube inductance, which is correlated with the first peak in the plasma voltage, has been considered as the change in plasma inductance during the pinch phase. As can be seen in Fig. 5.3,

the change in the tube inductance during the compression phase can reach up to 40 nH in argon gas, while in hydrogen and nitrogen gases is about 10 nH.

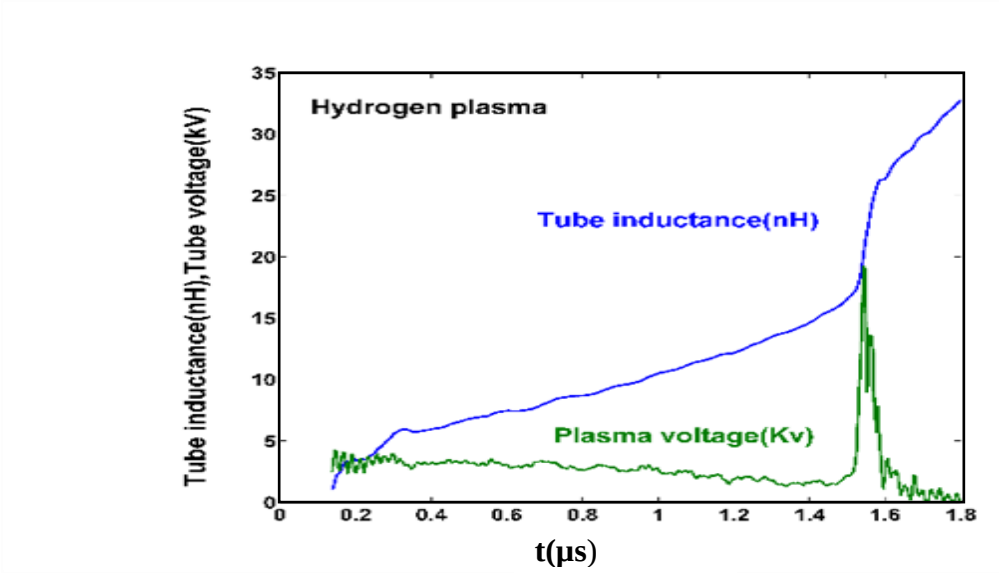

Fig. 5.3: Change in tube inductance in hydrogen gas.

The significant change in plasma inductance in argon gas compared to the nitrogen and hydrogen gases can explain the radiation-enhanced compression in high-z gases. The theoretical study of radiation-enhanced compression of a DPF by Braginski and Pease shows the feasibility of radiation cooling of plasma during the pinch phase [79]. Intense radiation of x-ray leads to decreasing the static pressure of the plasma. Decreasing the static pressure of the plasma causes a radiation-enhanced compression of the plasma column in the pinch phase. The increased compression of the plasma is eventually terminated by the plasma self-absorption as the plasma becomes highly dense.

The Lee model was used in argon and hydrogen gases to simulate the dynamics of the plasma in the compression phase. The simulated current waveform is fitted to the measured current waveform based on electrodynamics and thermodynamics of the measured situation, both in the

axial and the radial phases, for particular shots, as shown in Fig. 5.4. The simulation results show the radial and axial trajectories of the plasma during the pinch phase in both (a) hydrogen, and (b) argon gases, as presented in Fig. 5.4.

The minimum ratio of the pinch plasma radius to the anode radius in the hydrogen gas is 0.14, compared to the argon with a very small value of 0.012. Based on the minimum radius of the plasma column, the change in plasma inductance is about 8 nH in the hydrogen gas, and is about 40 nH in the argon gas. These results are in agreement with the measured results shown in Fig. 5.4, and could explain the measured large inductance of the argon pinch. The smaller radius of the plasma in argon gas can be explained by the plasma energy gain/loss during the compression phase. Based on the simulation results, the pinching plasma in argon gas loses 60 J over a radiative period of around 15 ns. During the most intense period, 30 J is radiated in FWHM time of 4 ns. In an argon pinch plasma, the thermal energy stored at the start of the radiation is computed to be 200 J. Therefore, 30% of the pinch thermal energy is radiated away during the pinch time. This level of radiation is sufficient in argon to fulfill the condition of energy depletion for strong radiative-enhanced compression of the pinching plasma. The analysis for the hydrogen shot shows that the loss of energy due to the x-ray radiation is only a small fraction during a pinch. Thus, the x-ray radiation from the hydrogen pinching plasma is not significant to cause a reduction of the pinch radius.

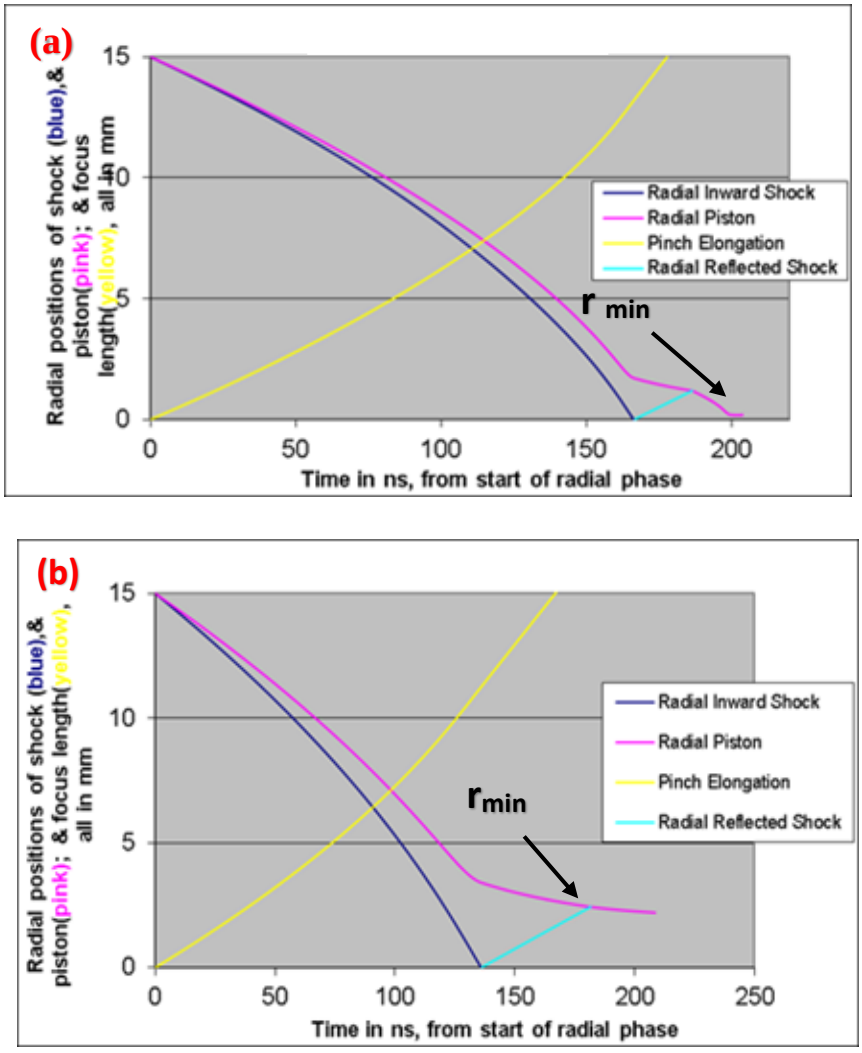

Fig. 5.4: The simulated radial and axial trajectories of plasma in (a) hydrogen gas, and (b) argon gas.

The power into the discharge tube can be calculated using$V_{Tube}(t)I(t)$. Fig. 5.5 shows the power into the plasma in argon gas, corresponding to the anode voltage and discharge current, in Fig. 5.1. Numbers 1 and 2 correspond to the pinch and post pinch phases.

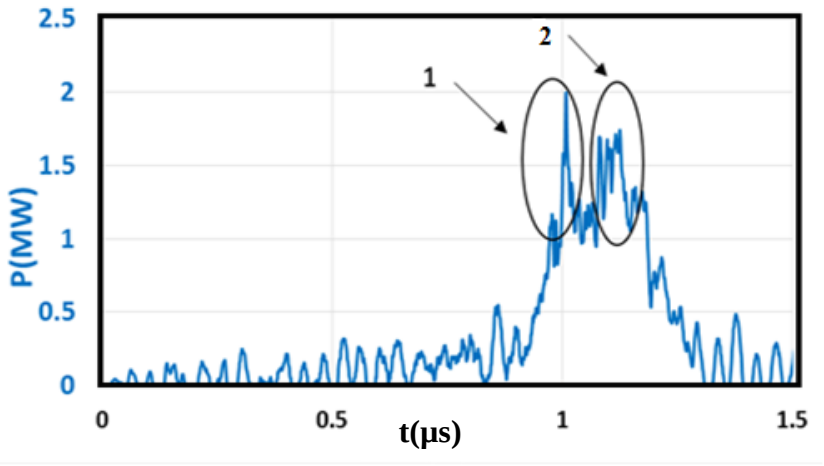

Fig. 5.5: Power into plasma in argon gas during the compression phase.

Based on the measured voltage across the plasma in the compression phase, and power into plasma, integrating the power over time during the compression phase gives the total energy injected into plasma in argon gas. This gives about 500 J in argon gas, 250 J in nitrogen gas, and 200 J in hydrogen gas. It is interesting to note that simulating the long drop of the discharge current shown in Fig. 5.1, based on Lee model for argon gas, requires anomalous resistance to explain the significant injected energy into plasma after the pinch duration [45, 12, 73]. In the following parts, the simulated results corresponding to the plasma anomalous resistance will be analyzed by circuit analysis of the device.

The effect of the atomic number of gas on the energy spectrum of ions generated from the pinching plasma was studied by measuring the ion beam energy based on the time of flight method. To measure the ion energy, the peak of the anode voltage (peak 1) is considered as the start of the ion emission. Peak 2 shows the hard x-ray signal. As can be seen in Fig. 5.6, the delay time between V-anode and H-X traces is about 30 ns. Peak 3 shows the proton beam signal.

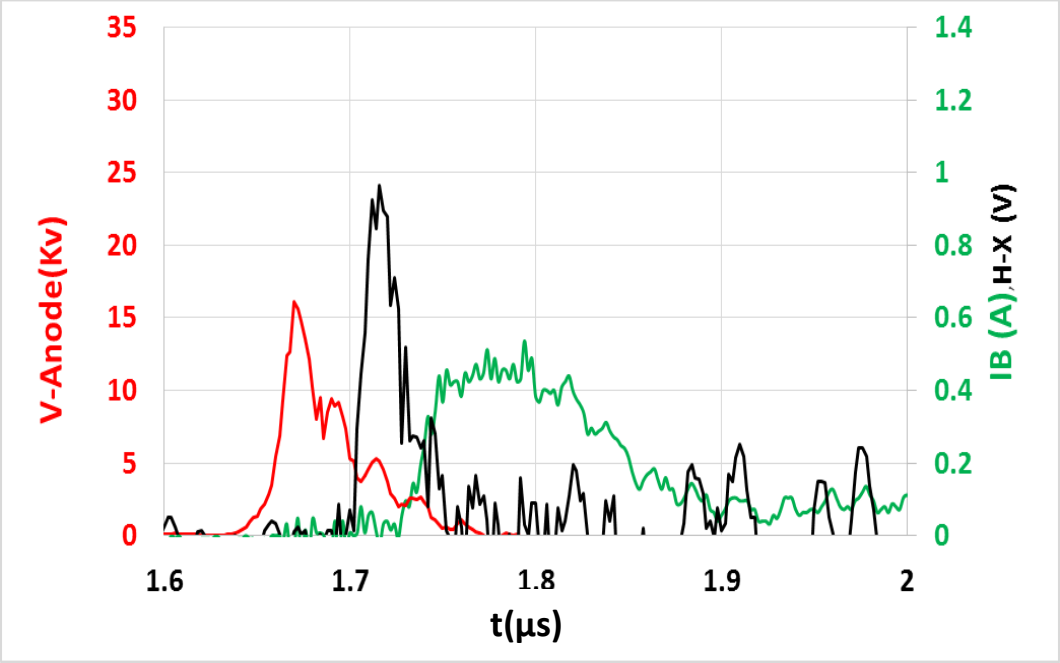

Fig. 5.6: Anode voltage, hard x-ray and ion beam signals in hydrogen gas.V_0 =28 kV, *P=5* Torr.

Based on the time of flight method, the typical energy spectrum of the proton generated from the DPF UofS-I in maximum charging voltage and different pressures can be seen in Fig. 5.7. Protons with energies between 15 keV to 20 keV contributed significantly in the peak of the proton current density. In the case of nitrogen, the ions with energies between 80 keV to 140 keV contributed significantly in the peak of ion current density. In the case of argon, ions with energies between 150 keV to 400 keV contributed significantly in the peak of the ion current density.

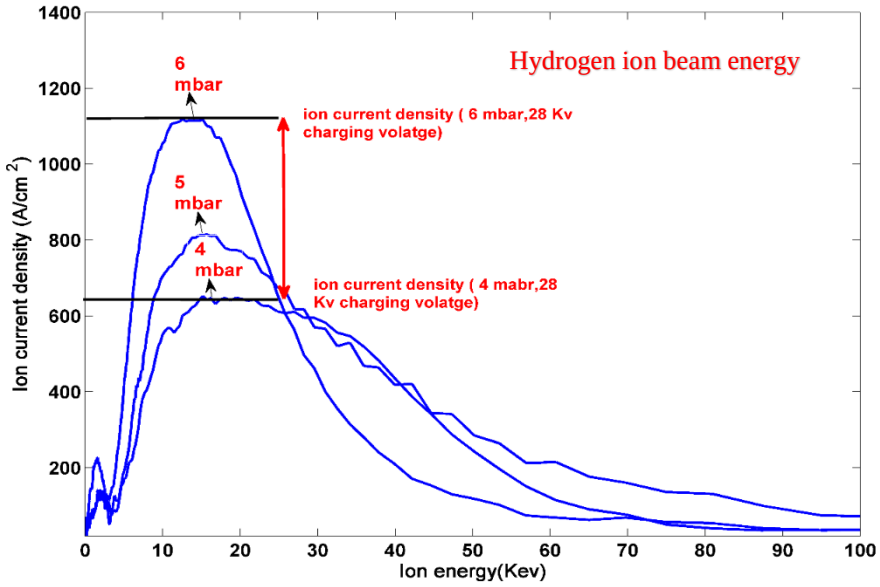

Fig. 5.7: Energy spectrum of proton generated from DPF UofS-I in maximum operating charging voltage.

The peak of ion current does not depend on the plasma voltage. However, increasing the plasma voltage shifts the energy spectrum of the generated ions to higher values.

The Lee model was used to predict the ion current density in the operating gases and pressures. A comparison of the experimental with the measured results in the three operating gases can be seen in Fig. 5.8. The results show that the simulated and measured ion current density have the same order of magnitudes in the operating gases and pressures.

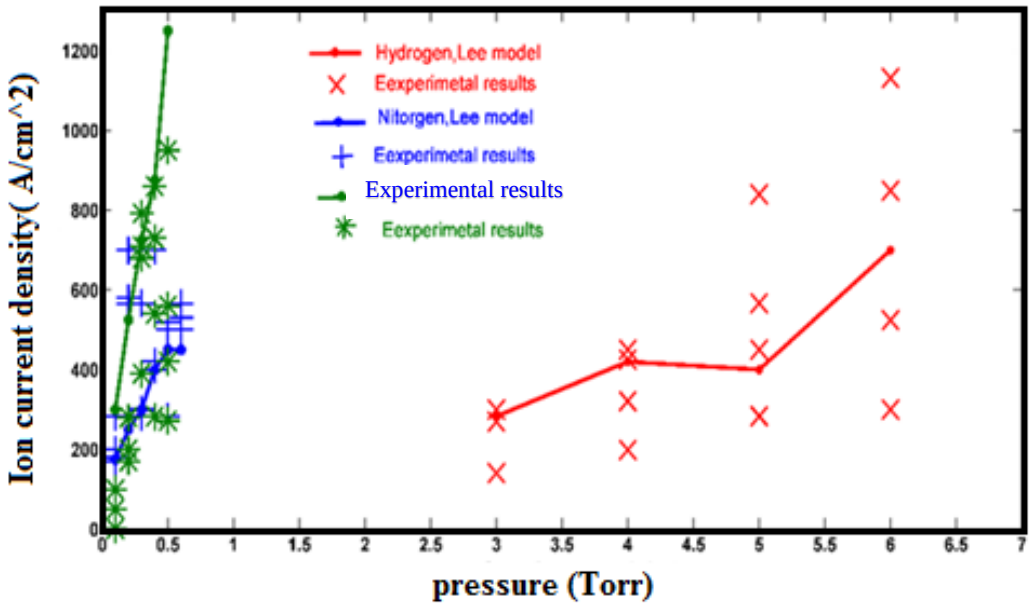

Fig. 5.8: The simulated and measured ion current densities in DPF UofS-I.

5.3 Anomalous Resistance and Injected Energy into Plasma

The inductive and resistive nature of the plasma impedance in a plasma is an unsolved issue. The time variation of the plasma voltage during the compression phase may be interpreted based on two scenarios. In the first scenario (inductive scenario), it is assumed that the plasma resistance during the final stage of the plasma focus is negligible [74]. In the second scenario (inductive-resistive scenario), it is assumed that plasma resistance becomes anomalous after the pinch phase ($t > t_{pinch}$), and that the inductive and resistive plasma voltage drops should be considered simultaneously [28].

The amount of energy that is injected into the plasma in argon gas is more than that in nitrogen and hydrogen gases, as experimentally obtained. To simulate the current trace and the tube voltage in argon gas in the DPF UofS-I, anomalous resistance has to be taken into account in the Lee model. Fig. 5.2 shows that the tube voltage, after the pinch (i.e. peak 2), is higher than the tube voltage during the pinch (i.e. peak 1). Considering that the tube voltage is given by Eq. 5-1, the difference between the tube voltages at time 2 and 1 gives Eq. 5-4

$$V_{Tube}(t_2) - V_{Tube}(t_1) = \underbrace{\left(IR_{Pl}(t_2) - IR_{Pl}(t_1)\right)}_{0} + \underbrace{\left(\frac{dL_{tube}(t_2)}{dt} I(t_2) - \frac{dL_{tube}(t_1)}{dt} I(t_1)\right)}_{0} + \underbrace{\left(\frac{dI(t_2)}{dt} L_{tube}(t_2) - \frac{dI(t_1)}{dt} L_{tube}(t_1)\right)}_{0} \quad <0 \tag{5-4}$$

The plasma resistance is negligible before the pinch (i.e. $IR_{Pl}(t_1) \simeq 0$). The change in plasma inductance reaches to its maximum during the pinch ($\frac{dL_{tube}(t_2)}{dt} I(t_2) - \frac{dL_{tube}(t_1)}{dt} I(t_1) < 0$). Because the time rate of change of current is negative, and its magnitude at t_1 is smaller than its magnitude at t_2, as measured, then the 3rd term is also negative for the case when the plasma inductance at t_2 is larger than that at the earlier time t_1 (i.e. $L_{tube}(t_2) > L_{tube}(t_1)$). Even if $L_{tube}(t_2) < L_{tube}(t_1)$, the magnitude, $\left|\frac{dI(t_1)}{dt} L_{tube}(t_1)\right| < 3$ kv ($L_{tube}(t_1) \approx 30$ nH), and $\frac{dI(t_1)}{dt} \simeq 10^{-11}$ (A/s), By subtracting the tube voltage at the time t_2 from that at t_1, Eq.5-4 gives

$$IR_{Pl}(t_2) > 7 \text{ kV} \tag{5-5}$$

Considering that the discharge current is about 50 KA, $R_{Pl}(t_2) \simeq 0.2\,\Omega$, which is considered as anomalous resistance [28, 73]. This result verifies the occurrence of anomalous resistance in the post-pinch phase in argon gas as the classical resistance of plasma in the order of 1 mΩ.

The injected energy during the compression phase reaches its maximum in the argon plasma. According to Fig. 5.5, the injected power into the tube after the pinch (i.e. peak 2) is significant compared to the pinch phase (i.e. peak 1). The injected energy into the plasma in argon focus after pinch is consumed by the anomalous resistance, as calculated by Eq. 5-5.

A significant increase of the plasma resistance at the post-pinch phase in the argon plasma might be related to the occurrence of a lower hybrid drift instability (LHDI) in such a phase [80-81]. The LHDI in the plasma is plausible when the drift velocity of the electrons (V_d) reaches the ion sound speed *(V_{Ion}) (i.e.* $\frac{V_d}{V_{Ion}} \geq 1$ *).* The ratio of V_d and V_{ion} can be expressed by Eq. 5-6, where Z is the effective charge of the ion, M is the ion mass, and N is linear plasma density [80-81].

$$\frac{V_d}{V_{Ion}} \alpha \sqrt{\frac{(Z+1)M}{N\,Z^3}} \qquad (5\text{-}6)$$

Eq.5.6 shows that the ratio of V_d to the V_{ion} depends on the density, the atomic mass, and the charge of the ionized atom. The LHDI is more plausible when the plasma density drops, or if the number of the ionization of the gas decreases. In a DPF, the plasma density decreases in the post-pinch phase, as compared to the pinch phase. It is interesting to note that decreasing the plasma temperature in the post-pinch phase, as compared to the pinch phase, can be followed by decreasing the effective charge of the ion (Z) in heavy gasses. The combination of the drop of plasma density and temperature can significantly increase the likelihood of the occurrence of

LHDI. This could explain the significant contribution of the anomalous resistance in the argon gas than in the hydrogen and nitrogen gases.

Plasma heating by an anomalous resistance (caused by the LHDI) can be expressed as

$P_J = (1 + 4\chi)\, P_{classic}$ in a plasma focus, where $P_{classic}$ is the plasma heating by classical resistance, and χ can be expressed by the following Eq.5-7 [80-81].

$$\chi = 7.95 \times 10^{47} \frac{I^4 A^{1/2} a}{N^{7/2} Z^{7/2} (Z+1)^{1/2}} \quad (5\text{-}7)$$

Here, a is the plasma radius, and A is the ion mass number. Eq.5-7 shows that the drop of the linear plasma density, and decreasing the atomic number of the gas, can significantly increase the injected power into the plasma by the anomalous joule heating process. The anomalous joule heating could terminate the radiation – enhanced compression in the argon gas.

5.4 Plasma Heating and the Emission of Runaway Charged Particle

The anomalous resistance can heat the plasma through the anomalous joule heating process. This Section will discuss the effect of the anomalous joule heating on runaway charged particle emission and x-ray generation during the post-pinch phase.

A test particle in a plasma becomes runaway when the decelerating force (imposed on the test charge by other charge particles) becomes negligible compared to the accelerating force exerted by the electric field. According to the Dreicer theory, this condition will be satisfied when the accelerating force on a test charge becomes greater than the critical electric field, as defined in Eq. 5.8 in a plasma, where n and T are the electron density and temperature, respectively [23]. It should be noted that based on the Dreicer theory, all particles become runaway in a time period

shorter than the collision time if the electric field across the plasma becomes larger than the critical field.

$$E(\mathrm{Vm^{-1}}) \approx 3.9 \times 10^{-10} \frac{n(\mathrm{cm^{-3}})}{KT(\mathrm{eV})} \quad (5\text{-}8)$$

The avalanche process is the secondary process that generates runway electrons in a plasma. In this process, the energetic electrons can produce secondary runaway electrons by coulomb collisions between two electrons.

The generation of runaway electrons and hard x-rays in a plasma focus based on Dreier condition yields a good agreement in a low energy DPF [78]. In a plasma focus, the electron density can reach up to 10^{19} cm^{-3}, and the plasma temperature can reach to 1 keV during the pinch phase [78]. The estimated plasma density and temperature in a plasma focus give 40 $kVcm^{-1}$ as the critical electric field. Assuming the pinch length is on the order of the anode radius which is 1.5 cm, the calculated critical voltage across the plasma column to produce runaway electrons is approximately 60 kV. In this experiment, the minimum required plasma voltage, about 25 kV (i.e. 16 $kVcm^{-1}$ for the electrical field), is required to generate hard x-rays from the device.

It is interesting to calculate the time rate of runaway electron generation in a pinching plasma by considering the minimum required electric field for hard x-ray radiation from the plasma. Eq.5-9 shows the time rate of primary runaway generation (based on Dreicer theory) in a plasma, where v_e is the collision frequency of the thermal electron (that is about 10^9 /s in pinching plasma), $\alpha = E/E_c$, where E is the electric field and E_c the critical electric field, and n_e the density of the background electrons [82]. By considering the experimental electric field for hard x-ray

generation is at minimum (16 kVcm^{-1}in argon gas, Z_i=10) , the estimated time rate of primary runaway density in plasma is about $S_D \simeq 10^4 n_e$ (cm^{-3} s^{-1})

$$S_D \simeq n_e v_e \alpha^{-\frac{3(Zi+1)}{16}} \exp\left(-\frac{1}{4\alpha} - \sqrt{\frac{(Zi+1)}{\alpha}}\right) \quad (5\text{-}9)$$

The time rate of the runaway electron emission based on avalanche process can be estimated as $S_a = n_r / \tau_{av}$ where $\tau_{av} \propto E^{-1}$ and is about 10^{-9} s (based on an electron collision frequency in pinching plasma), where n_r is the density of the runaway electrons, and $S_a \simeq 10^9 \times n_r$ (cm^{-3} s^{-1}) in a plasma focus. In the absence of the loss mechanism, the time rate of the runaway density can be expressed as $dn_r/dt = S_D + S_a$. The solution can be presented by Eq. 5-10, where t is in the unit of ns.

$$n_r = 10^{-5} n_e (e^t - 1) \quad (5\text{-}10)$$

It is interesting to note that the lifetime of the pinch is on the order of ten nanoseconds, $n_r \simeq 10^{-3} n_e$. Considering the ratio, $S_a/S_D = (e^t - 1)$, shows that the rate for runaway generation by the avalanche process becomes greater than the primary process within less than 1 ns in the pinching plasma, suggesting that the avalanche process plays an important role in the runaway electron generation in a plasma focus. The generation of hard x-rays has been observed when E/n_e is on the order of 10^{-16} and $n_r \simeq 10^{-3} n_e$ in a tokamak [82]. Considering that $n_e \simeq 10^{16}$ cm^{-3} in tokamaks, the minimum experimental electric field (≈1 V/m) for the hard x-ray generation gives the same ratio of electric field to the electron density that is observed in a Tokamak although the two devices are working in two different time scales [83].

The comparison between the required electric field to generate hard x-rays in the pinch and post-pinch phases of the anomalous resistance shows that the required electric field to generate hard x-rays in the post-pinch phase is less than the required electric field to generate hard x-rays in the pinch phase. Considering that the elongation speed of plasma column is about 10^5 m/s, according to simulation result, the length of the plasma column can increase up to 1 cm in 100 ns. Comparing the intensity of the plasma voltage at peaks numbered 1 and 2 in Fig. 5.10 (a) and the time difference of about 120 ns between the two main peaks, the electric field across the plasma then is about 11 kV/cm in the post-pinch phase.

The comparison between the peaks numbered 1 and 2 in Fig. 5.9 (a) and (b) shows the approximately the same peak intensity of hard x-ray signals in the post-pinch phase was generated, and the electric field across the plasma in the post-pinch phase is smaller than the electric field across the plasma in the pinch phase.

The signature of the anomalous resistance has been found during the post-pinch phase. The lower required electric field to generate hard x-rays can be interpreted by considering the anomalous Joule heating and the drop of plasma density in that same phase. Moreover, intense radiations of soft x-rays have been observed in the post-pinch phase in DPF UofS-I, as can be seen in Fig. 5.10.

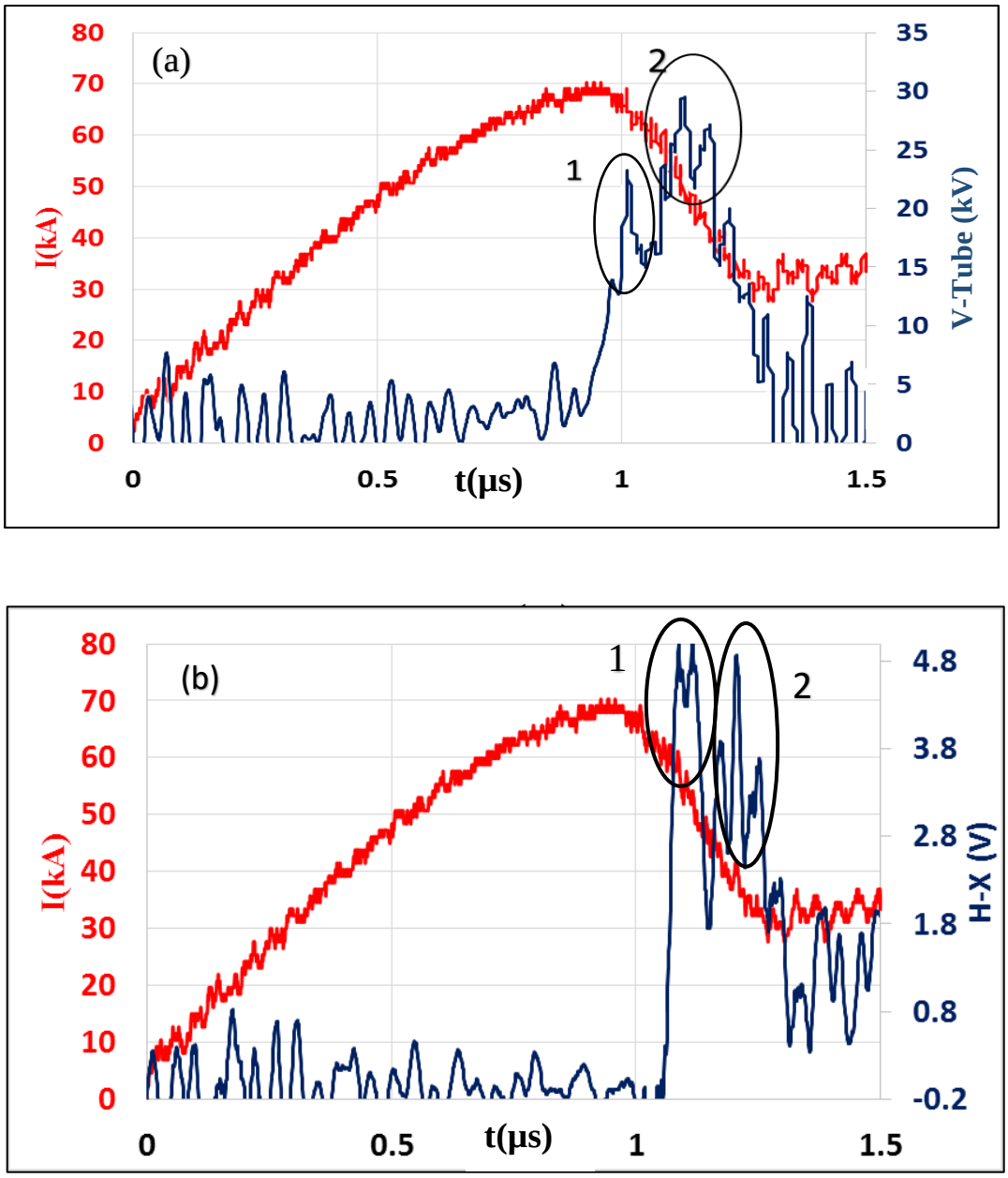

Fig. 5.9: (a) tube voltage and discharge current, and (b) discharge current and hard x-ray signals.

The peaks numbered 1 and 2 are correlated with the peaks numbered 1 and 2 in tube voltages and hard x-rays in Fig. 5.10. This feature can also be interpreted as the effect of the plasma Joule heating in that same phase.

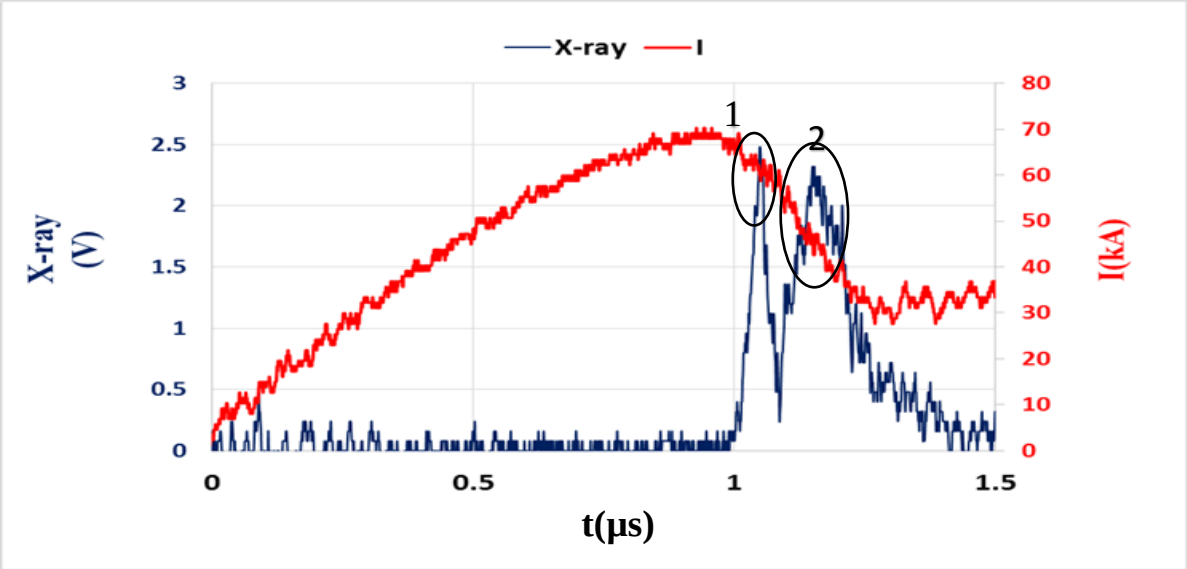

Fig. 5.10: Soft x-ray signal from DPF UofS-I.

It is interesting to estimate the falling and rising time of the x-ray signal based on the measured plasma resistance and inductance. The time evolution of the plasma resistance can be estimated by $R_0\left[e^{\frac{-t}{t_2}} - e^{\frac{-t}{t_1}}\right]$, where R_0 is a constant on the order of 1 Ω [28,45], t_1 is the characteristic rising time of the anomalous resistance, and t_2 is the characteristic falling time.

The x-rays generated by the anomalous resistance has a fast rising time due to a sudden occurrence of instabilities. Fig. 5.11 shows the fast rising time of the x-ray signal within 50 ns and the fast rising time of the second peak of x-ray signal within 10 ns (which is even shorter than the rising time of the observed during the first peak of the hard x-ray signal). The falling time of the x-ray signal is about 250 ns.

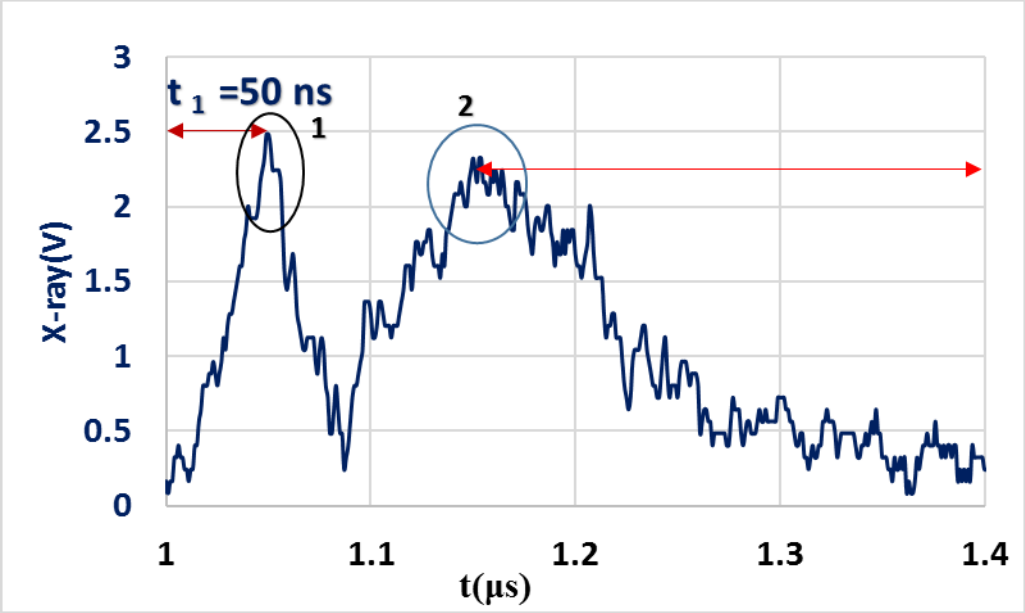

Fig. 5.11: Rising time and falling time of x-ray signal.

The observed hard x-ray falling time can be estimated *by* $t_2 = L_{Plasma} / R_{Anomalous}$ (a characteristic time to transfer energy from the stored magnetic energy into the plasma through anomalous resistance). Experimentally, the falling time of the second x-ray peak is on the order of hundreds of nanoseconds. By considering the plasma inductance on the order of 10^{-8} nH, as discussed earlier, and the plasma resistance in the order of 0.1 Ω, the falling time t_2 is then around 10^{-7} s, corresponding to the observed falling time of the x-ray signal.

5.5 DPF Device with Semi-Active Electrodes (DPF-SAE)

Fusion research on a DPF device was put on hold due to the saturation of the neutron yield with increasing stored energy of a DPF device. Moreover, operating a high-energy DPF device causes many technical problems due to the impurities and instability effects that prevents formation of the focusing plasma. To solve these problems, a staged-plasma focus is implemented by using two plasma focus devices that can be placed in front of each other, and combined through a mid-plane disk. Furthermore, it has been suggested to increase the neutron yield beyond the established scaling law for a single-gun DPF device [84]. However, the main problem in these configurations is the timing of the focusing event in each of the DPF device. It should be noted that the delay time between the two focusing events in the two DPF devices with the same operating conditions is mainly caused by the delay time between the switching of spark gaps, and the delay time between the occurrence of breakdown in the two discharge tubes. The time difference of two focusing events can be improved in a hypocycloidal pinch [85], which consists of two cathode disks with a common anode disk. In this configuration, two focusing events could generate charged particles in the opposite directions.

In this Section a new configuration of a DPF device built will be introduced. In the first part, the technical details of an SAE-type plasma focus will be presented. In the second part, the electrical discharge signals of the device will be shown and analyzed. In the third part, the generation of charged particles and x-rays from the device will be presented. The results corresponding to the charged particles and x-ray radiations from a DPF-SAE and the DPF UofS-I will be compared.

5.5.1 Configuration of DPF-SAE

The cross view of an SAE-type plasma focus is shown in Fig. 5.12. The system is the same as DPF UofS-I except the electrode head. In the SAE-type plasma focus, three electrodes that are isolated by insulators from each other are used to form two discharge tubes. The inner electrode (1) is connected to the capacitor bank through a spark gap switch. The middle electrode (2) is isolated electrically from the capacitor bank. The electrode 2 is termed the semi-active electrode in this thesis. The outer electrode (3) is connected to the capacitor bank through the ground connection. Two current layers can be formed between the two discharge tubes after the discharge of a single capacitor bank. The current layers are then accelerated by the $\boldsymbol{J} \times \boldsymbol{B}$ force in the axial and radial phases. The electrodes 1 and 2 are cylindrical copper electrodes, and electrode 3 is made of 12 copper rods. Fig. 5.13 shows the equivalent circuit of an SAE-type plasma focus.

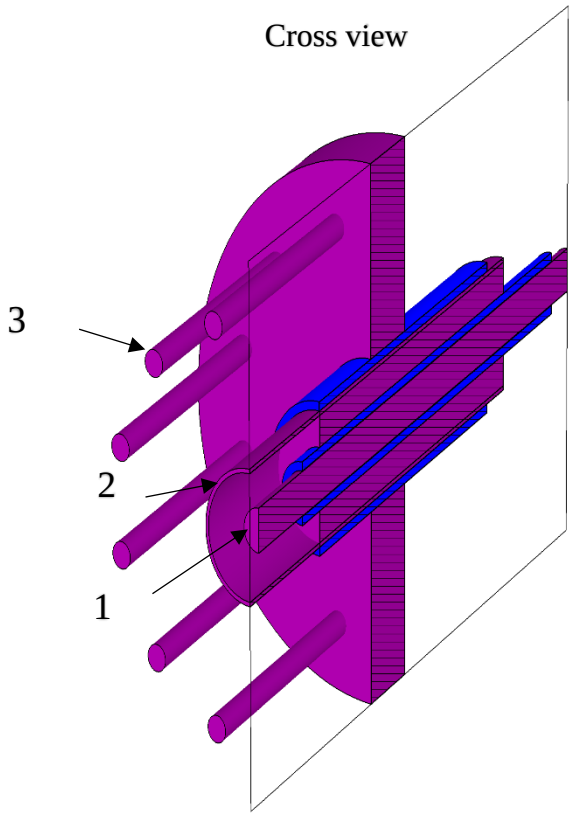

Fig. 5.12: Cross view *of DPF-SAE, The red color shows the copper and blue color shows the insulator.*

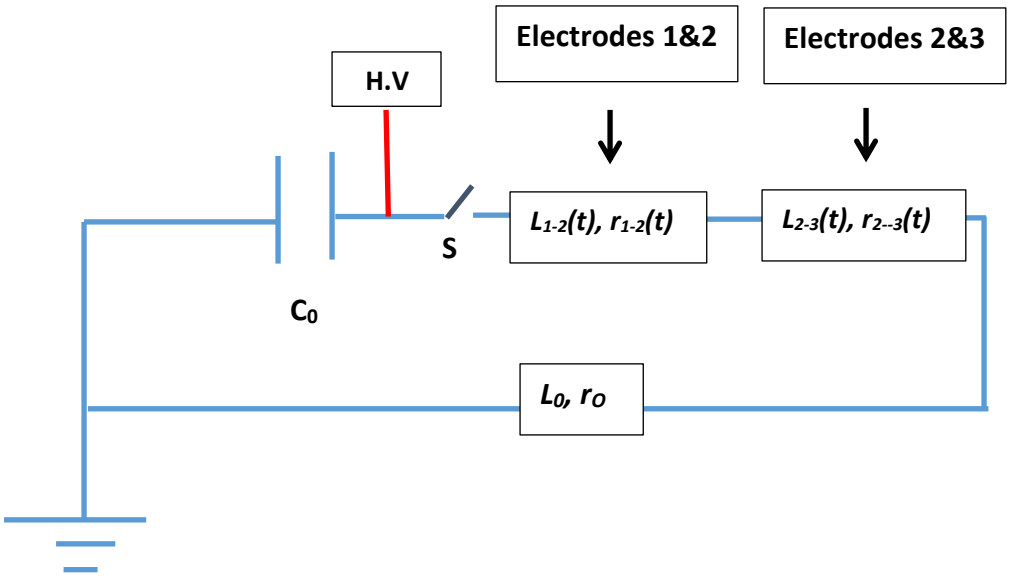

Fig. 5.13: The equivalent circuit of SAE type plasma focus.

Fig. 5.14 is a picture of the DPF-SAE assembly. To optimize the geometry of the three electrodes, the Lee model has been used for two independent DFP devices. Assuming that DPF UofS-I is a combination of electrodes 1 and 2, the Lee model gives a length of 0.5 cm for the radius of electrode 1, and 1.5 cm for the radius of electrode 2, to achieve the good focusing conditions in a deuterium gas at a pressure of 3 Torr. Assuming DPF-II as a combination of electrodes number 2 and number 3, Lee model gives 1.5cm for the radius of electrode number 2 and 5 cm for the radius of electrode number 3 to achieve best focusing conditions in Deuterium gas at 3 Torr. Figure 5.15 shows the focusing effect in the DPF-I and DPF-II, based on simulation results. The Lee model gives a rough estimation of the dimensions of three electrodes. A new code has to be developed to optimize the geometry of the electrodes for the SAE-type dense plasma focus devices.

The timing of the two focusing events can be synchronized by: (a) a proper length of electrodes, and (b) a proper length of insulators between the electrodes. It should be noted that in an SAE-type plasma focus, the spark gap and the transmission line are common between the

electrodes. The breakdown between electrodes happens at the same time as they are in series. Table 5.2 shows the parameters predicted by the Lee model for an SAE-type plasma focus device.

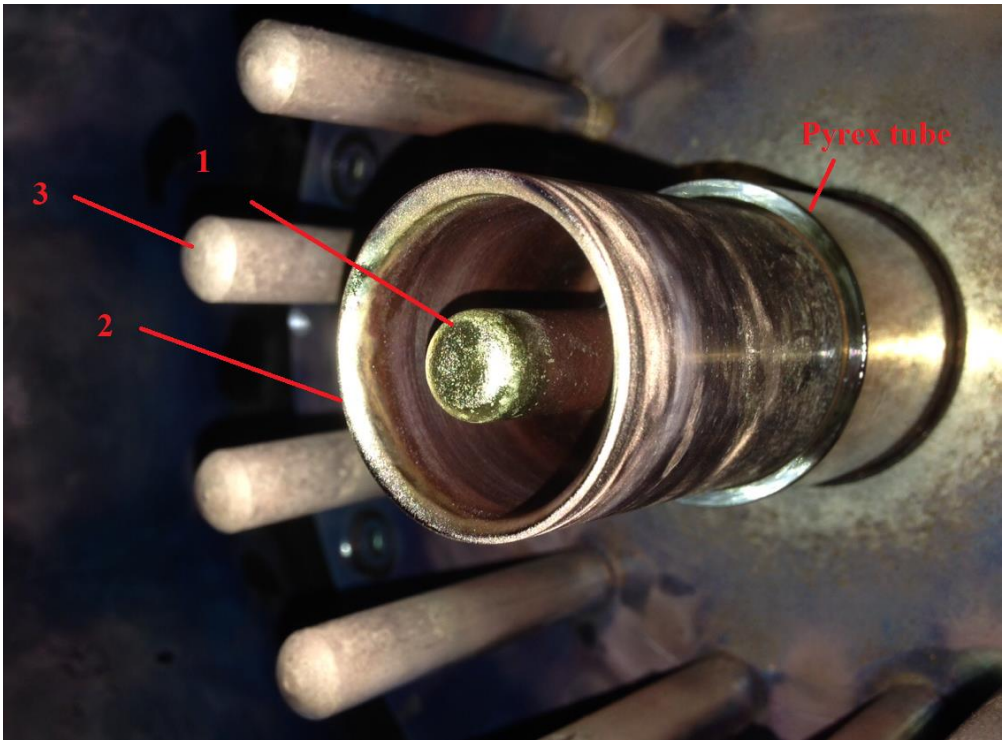

Fig. 5.14: Experimental set-up of electrodes in SAE type plasma focus.

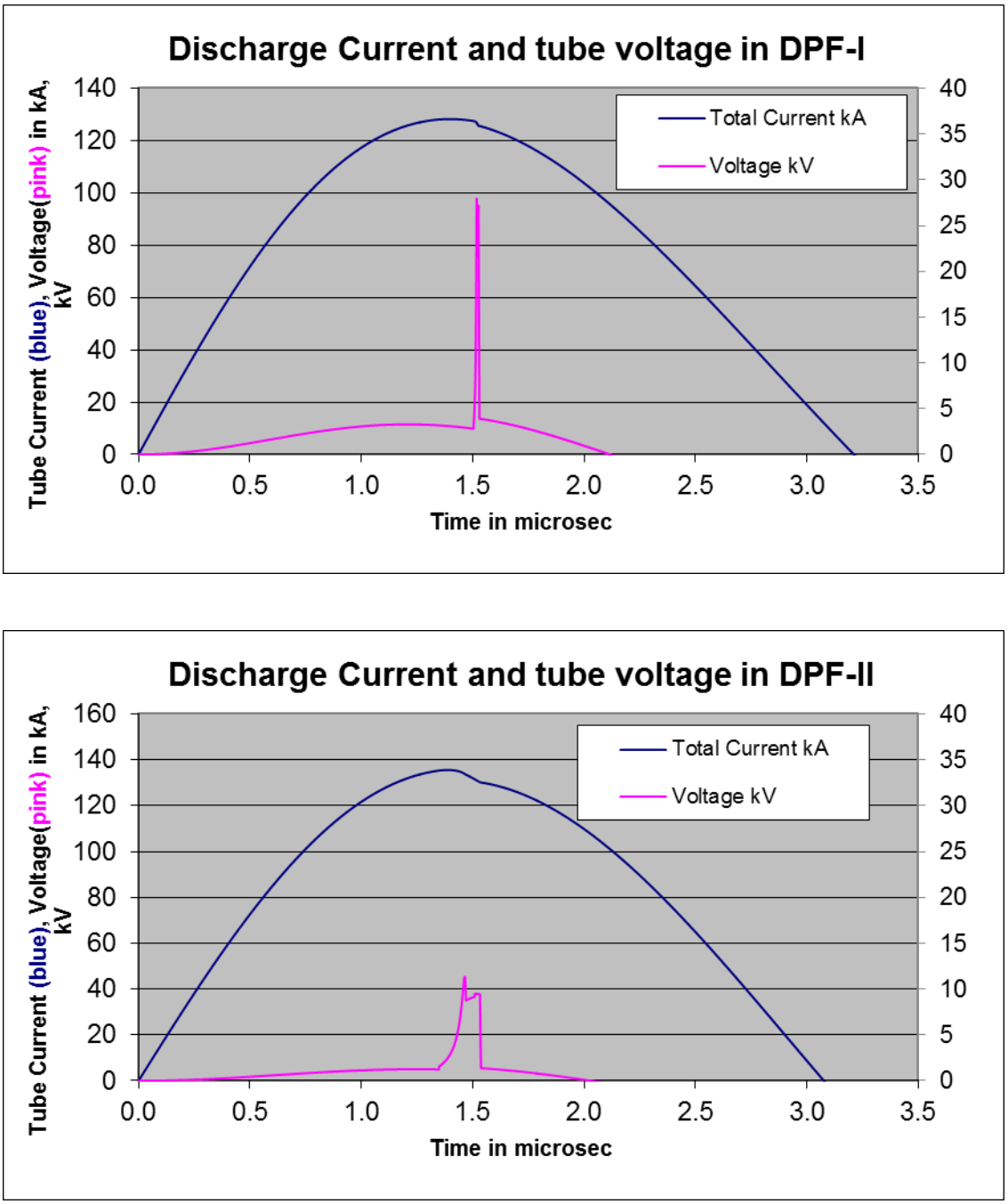

Fig. 5.15: Simulated discharge current and tube voltage using Lee model separately for DPF-I and DPF-II.

Table 5.2: Parameters predicted by Lee model for SAE type plasma focus.

Parameter	Value
Capacitance (C_0)	4.9 μF
Inductance e (L_0)	150 nH
Charging voltage (V_0)	28 kV
Stored energy (E_0)	2 kJ
Peak discharge current	140 kA
Electrode number 1 radius (a)	0.5 cm
Electrode number 2 radius(b)	1.5 cm
Electrode number3 radius(c)	5 cm
Electrode number 1ength (L-1)	15 cm
Electrode number 2 length (L-2)	4 cm
Electrode number 3 length (L-3)	4 cm
Operating pressure	3 Torr

An SAE type-plasma focus has been operated in hydrogen, nitrogen, and argon gas. To measure the discharge current and voltage, a current probe and two high voltage probes have been used. The connection of the probes can be seen in Fig. 5.16. V_1 and V_2 are the measured voltages of the central electrode 1 and the semi-active electrode 2 with the grounded cathode 3. The current probe measures the current to the anode. The semi-active electrode is insulated from from the anode and cathode and is connected to the anode and cathode through the plasma.

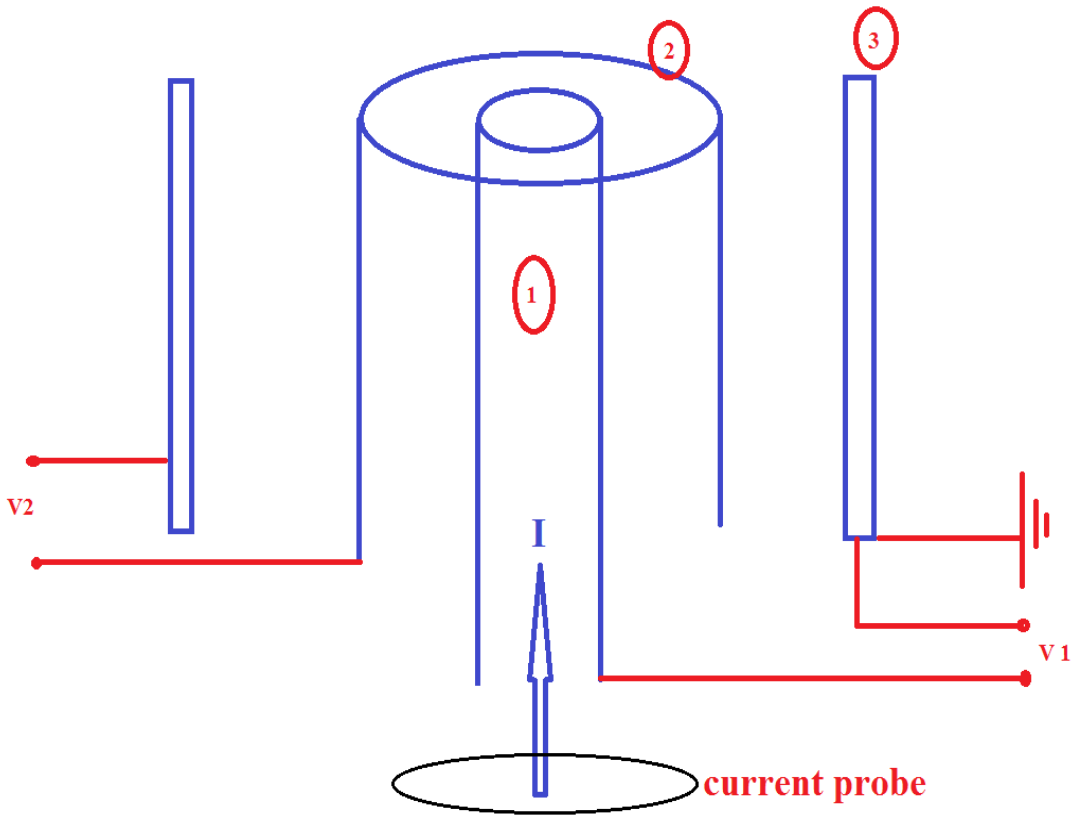

Fig. 5.16: Connection of current probe and two high voltage probes.

The measured waveforms of the discharge current and tube voltages in an SAE-type plasma focus operating in argon gas are shown in Fig. 5.17. The first drop of current shows the focusing effect in DFP-I, and the second current drop shows focusing effect in DPF-II. Figure 5.17 shows that the second focusing event starts right after the first focusing. The operating pressure can vary the timing and the number of focusing events, as can be seen in Fig. 5.18. To measure the voltage across the plasma between each pair of electrodes, circuit analyses based on the waveforms of the discharge current and high voltages are necessary.

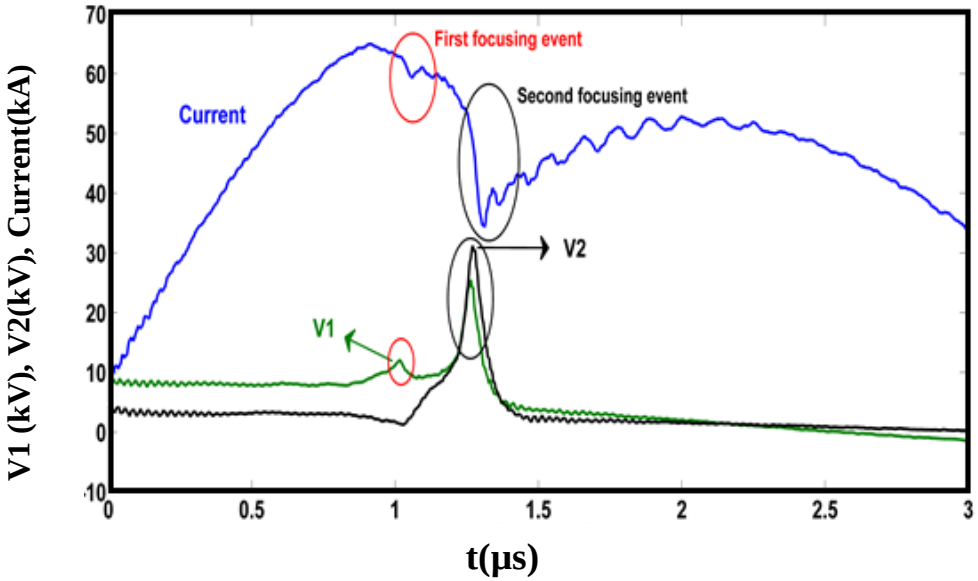

Fig. 5.17: Discharge current and tube show two focusing events occur almost at the same time. The operating pressure P≈ 0.1 Torr, argon gas.

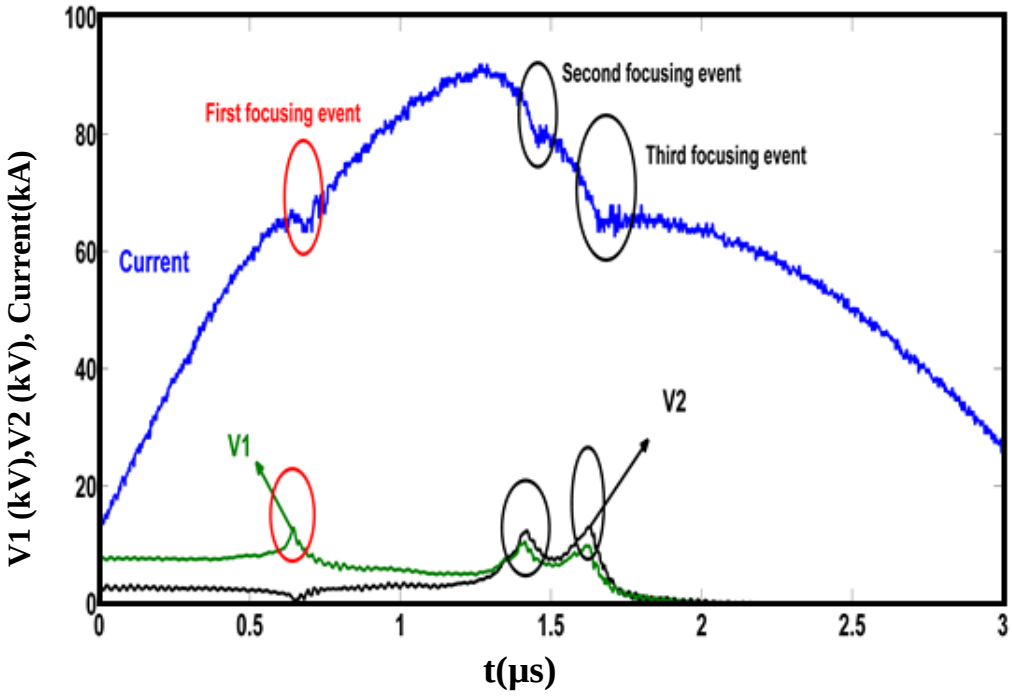

Fig. 5.18: Discharge current and tube voltages show three focusing events occur at different time. The operating pressure P ≈0.2 Torr, argon gas.

5.5.2 Discharge Circuit Analyses in DPF-SAE

The voltage across the discharge electrodes *($V_1 = V_{tube}$)* can be expressed by Eq. 5-11,

$$V_{Tube} = V_1 = \frac{d}{dt}\left[L(t)\right] f_c I + L(t) f_c \frac{dI}{dt} + r(t) f_c I = V_0 - \int \frac{Idt}{c_0} - R_0 I - L_0 \frac{dI}{dt} \qquad (5\text{-}11)$$

where f_c is the fraction of the discharge current that passes through the plasma, V_0 is the charging voltage of the capacitor, C_0 is the capacitance. $L(t) = L_{1\text{-}2}(t) + L_{2\text{-}3}(t)$, and $r(t) = r_{1\text{-}2}(t) + r_{2\text{-}3}(t)$. $L_{1\text{-}2}(t)$ and $r_{1\text{-}2}(t)$ refer to the plasma inductance and resistance that is formed between electrodes 1 and 2. $L_{2\text{-}3}(t)$ *and* $r_{2\text{-}3}$(t) refer to plasma inductance and resistance between electrode number 2 and 3.

The tube voltage can be calculated using the discharge current and anode voltage, based on Eq. 5-12,

$$V_{Tube}(t) \simeq V_A(t) - L_0 \frac{dI}{dt} \quad (5\text{-}12)$$

where $V_A(t)$ is the anode voltage, $I(t)$ is the discharge current, and L_0 is the inductance of the discharge circuit from the voltage probe to the discharge electrodes. Considering that $L_0 = 70$ nH in the experiment, the measured tube voltages can be seen in Fig. 5.19, where three peaks of voltages correspond to the three focusing events. The voltage between the electrodes 2 and 3 *(i.e.* V_2*)* and the difference between V_1 and V_2, can be seen in Fig. 5.20.

The voltage corresponding to V_2 shows one peak, while the voltage difference $V_1 - V_2$ shows two main peaks. The last peak in the $V_1 - V_2$ signal is correlated with the peak voltage in V_2. A voltage drop can be observed in the V_2 signal when the peak of the voltage appears in V_1. Increasing the impedance of the plasma between the electrodes 1 and 2 causes a drop of voltage in V_2 since the voltage V_1 is divided between the electrodes 1 and 2 and the electrodes 2 and 3 (i.e. V_2). Increasing the plasma impedance between electrodes 2 and 3 causes a peak voltage in the V_2 signal.

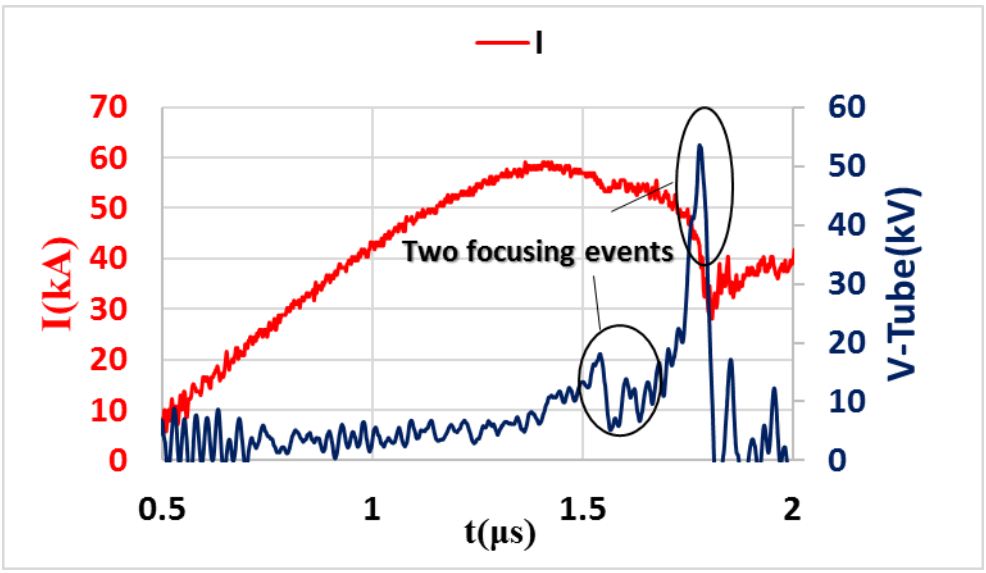

Fig. 5.19: The waveforms of the tube voltage and discharge current in DPF-SAE. P≈0.1 Torr, *argon gas.*

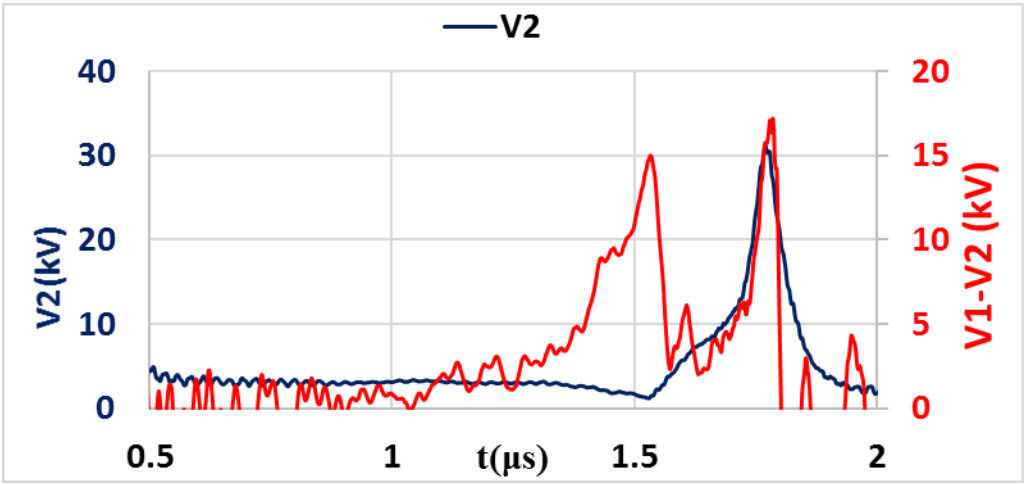

Fig. 5.20: The voltage on electrodes number 2 and the difference between V_1 and V_2.

Three peaks in $V_1 - V_2$ shows an increase of plasma impedance between the electrodes 1 and 2 in three different stages. The single peak in the V_2 signal shows an increase of plasma impedance between electrodes 2 and 3 in a single stage. The first peak in $V_1 - V_2$ corresponds to the

first focusing event between electrodes 1 and 2. The second peak in $V_1 - V_2$ appears at the starting time of the main peak in V_2. The third peak in $V_1 - V_2$ is correlated with the first peak in V_2. The duration of this peak is shorter than the duration of the main peak in V_2. The main peak in V_2 corresponds to the focusing of the plasma between electrodes 2 and 3. It should be noted that the nature of the second and third peaks in $V_1 - V_2$ signals is not yet clear.

5.5.3 Charged Particle Emission and X-ray Radiation from the DPF-SAE Device

Fig. 5.21 shows the ion beam and hard x-ray signals from the DPF-SAE device together with the current signal. The corresponding V_1 and $V_2 - V_1$ signals were presented in Fig. 5.20. There are three peaks in the ion beam signal and two peaks in hard x-ray signal. The energy of the hard x-ray exceeds 100 keV based on the filter used. The duration of the hard x-ray radiation can reach up to 500 ns, and the duration of the ion beam can reach up to 1μs. It is interesting to note that the second peak in the hard x-ray signal appears after the second peak in ion beam signal. Figure 5.22 shows the waveforms of ion beam emissions and hard x-ray radiations from another DPF-SAE discharge which resulted in three peaks in both signals (the number of peaks vary between two and three peaks in the experiment). The first peak of ion beam signal is correlated with the first focusing event of the plasma between electrodes 1 and 2 in the SAE-type plasma focus. The second peak of the ion beam appears before the second focusing event. The third peak of ion beam signal is correlated with the second focusing event of the plasma between electrodes 2 and 3.

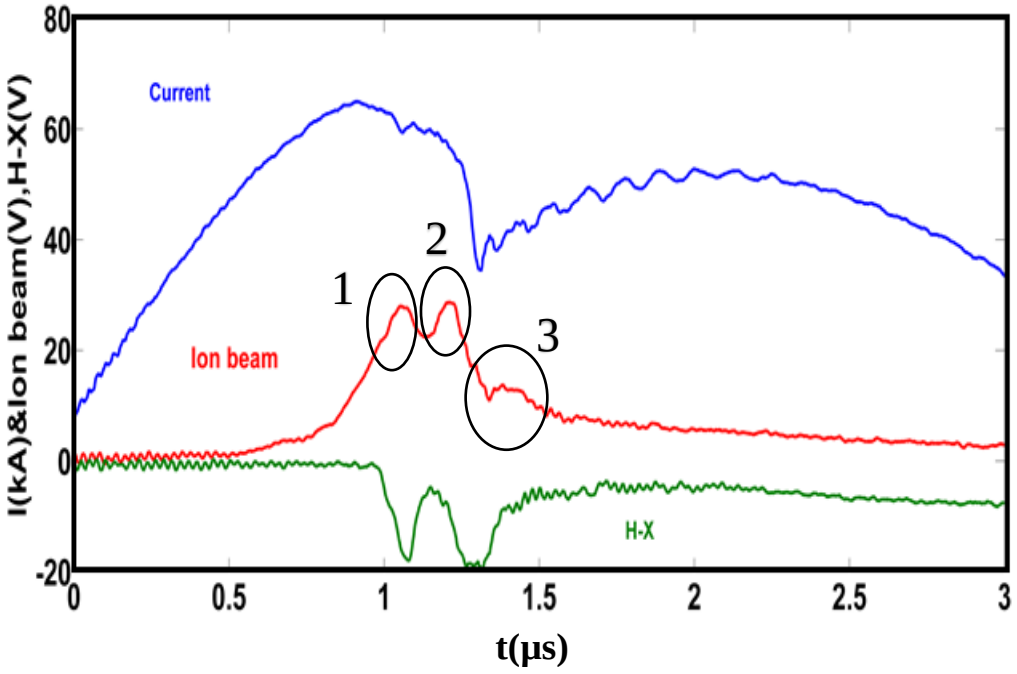

Fig. 5.21: Three periods of ion beam emissions and hard x-ray radiations from DPF-SAE.

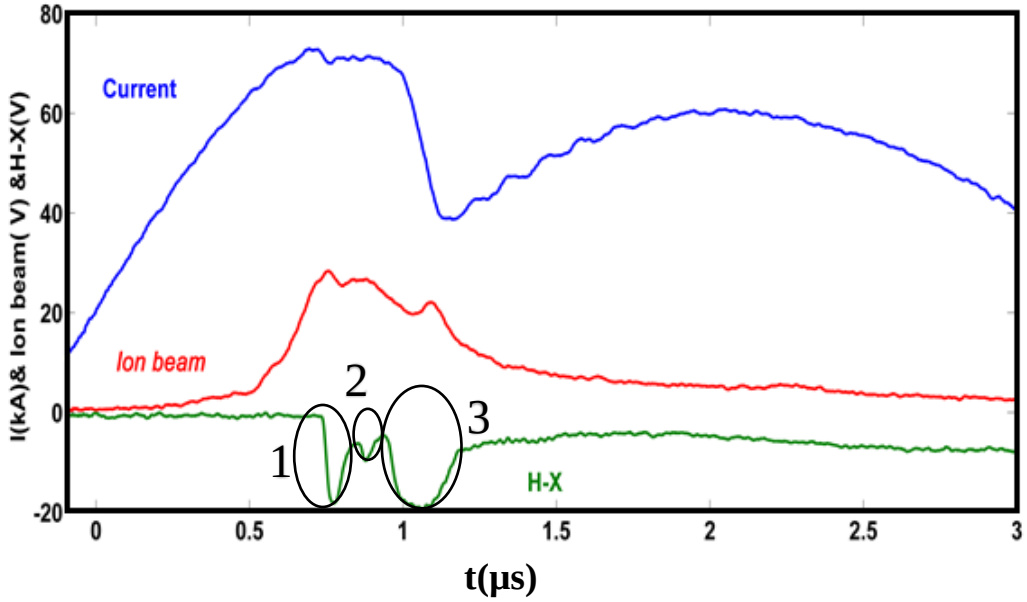

Fig. 5.22: Three periods of ion beam emissions and hard x-ray radiation from DPF-SAE.

Based on the strong radiations of hard x-rays and energetic ions, significant radiation of the electron beams, soft x-rays, and neutrons from the device, are also expected. Anomalous resistance, rapid change in plasma inductance, and magnetic reconnection of the two current layers, might be the possible mechanisms of charged particle and x-ray radiations from the plasma.

The occurrence of two focusing events in a proper time frame can enhance the duration of charged particle emissions and x-ray radiations from the DPF-SAE device. Further experiments are needed to synchronize the two focusing events by changing the geometry of electrodes, the working pressure, and the insulator length.

5.5.4 Comparison of Ion Emissions and X-ray Radiations between DPF-SAE and DPF UofS-I Devices

The DPF-SAE and the DPF UofS-I devices were operated under the same conditions, e.g., with the same stored energy (2 kJ). Figure 5.23 shows comparison of the ion beam signals from the two different DPF configurations. The longer duration of the ion beam with a higher intensity in the SAE-type plasma focus can be explained by the longer duration of the current drop and the tube voltage.

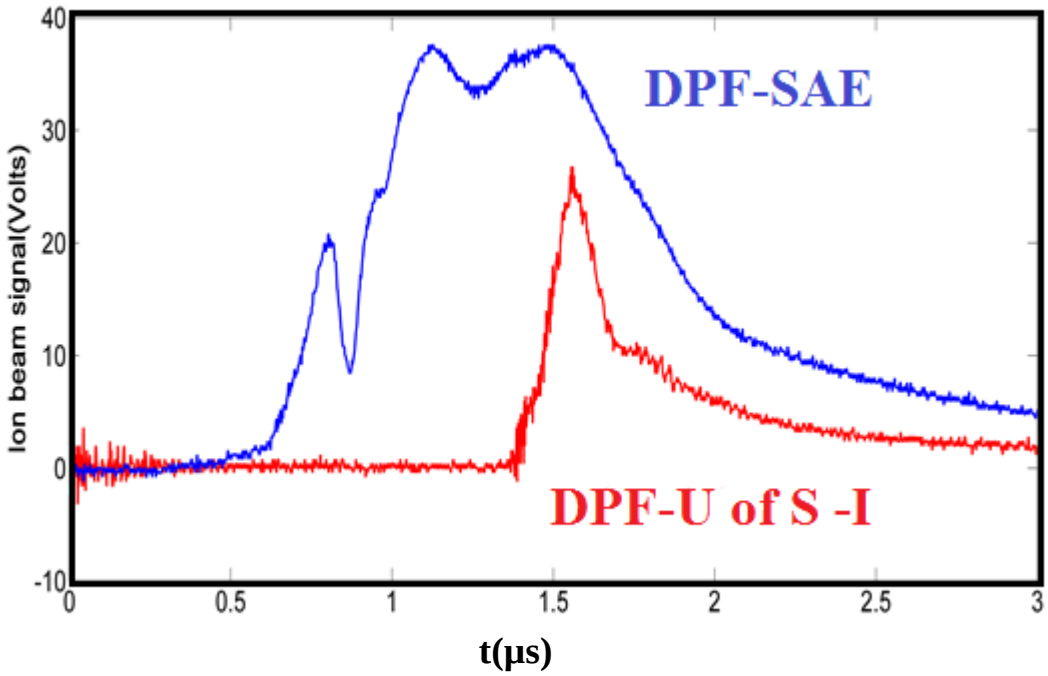

Fig. 5.23: Comparison of ion beam garnered from DPF-SAE and DPF-UofS-I devices.

Figure 5.24 shows the comparison between the hard x-ray signals in the DPF-SAE and the DPF UofS-I devices. The duration of hard x-ray signal that is generated by the DPF-SAE is about 500 ns, while the hard x-ray signal from the DPF UofS-I lasts only up to 300 ns. A significant increase in hard x-ray intensity generated from the DPF-SAE device compared to DPF UofS-I device shows a more effective operation in the DPF-SAE as a new type of hard x-ray based on DPF. Intense radiations of hard x-rays show strong bombardment on electrodes due to energetic electrons**.** The first peak in the hard x-ray signal is correlated with the first focusing event of the plasma between electrodes 1 and 2, while the second peak of the ion beam appears before the second focusing event. The third peak of the hard x-ray signal is correlated with second focusing event occurring between electrodes 2 and 3 in the SAE-type plasma focus.

The results corresponding to the tube voltage, ion beam emission, and hard x-ray radiation from the DPF-SAE device, compared to DPF UofS-I device, show a higher injected energy into the plasma, and a better operation overall as an ion and x-ray source. The study of soft x-ray radiations and neutron emissions from the SAE-type plasma focus are some of the interesting future research that can be implemented.

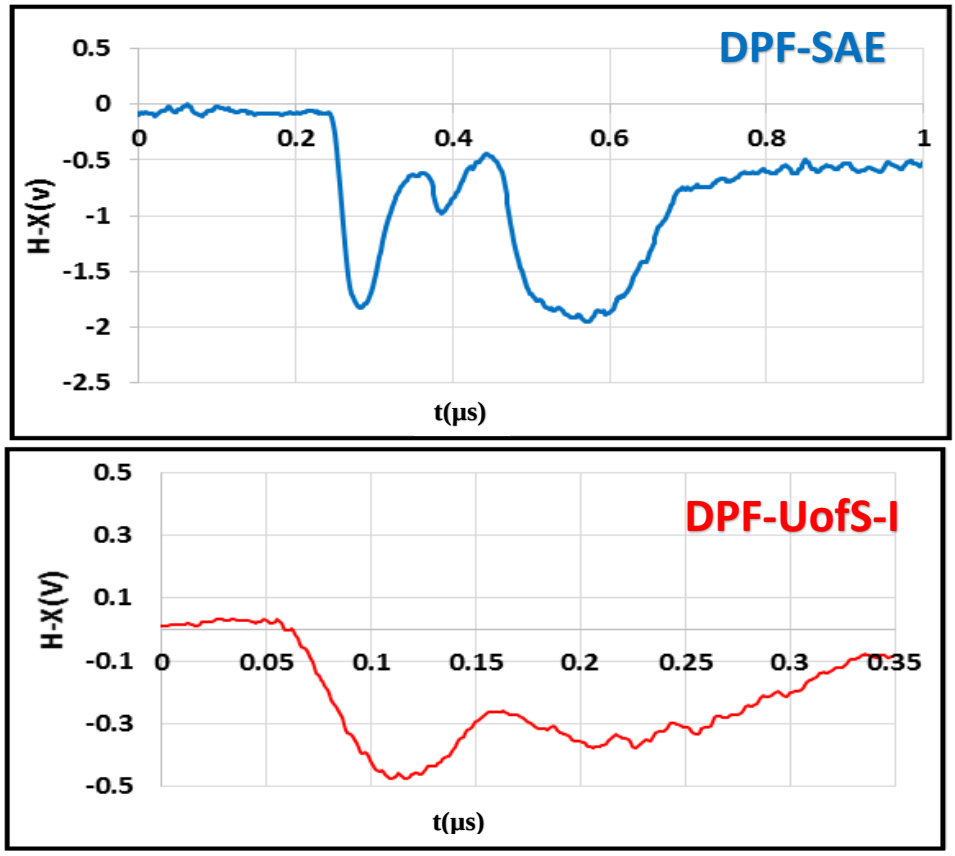

Fig. 5.24: The comparison of hard x-ray signals in DPF-SAE and DPF UofS-I device.

Chapter 6

SUMMARY

6.1 Summary

In this thesis, a brief introduction on magnetic pinch devices has been presented. The Lee model, a well-known model in simulating the phenomena in a focusing plasma, has been introduced. The design and optimization of a low energy plasma focus in enhancing charged particle emissions and x-ray radiation from the device have been discussed. The design and the technical details of a dense plasma focus have been explained. The Lee model has been used to predict the optimum ion current emission from the device. Several detectors, such as a Faraday cup, a soft x-ray detector, a hard x-ray detector, and an electron beam detector, have been developed, and the technical details have been introduced.

A series of experiments have been performed on the DPF UofS-I. Different regimes of focusing have been observed in three operating gases (i.e. hydrogen, nitrogen, and argon). The results show that the duration of the current drop and the injected energy into the plasma increased significantly in the argon gas compared to the hydrogen gas. For all three operating gasses, a circuit analysis has been performed to study the plasma voltage, the plasma inductance, and the injected energy into the plasma. The plasma voltage, plasma inductance, and injected energy into plasma are maximized in DPF UofS-I in argon gas. The maximum duration of the current drop has also

been observed when argon is used as the operating gas. Based on simulation results, the radiation-enhanced-compression of the plasma and the anomalous resistance have been adopted as the mechanism to explain the measured plasma inductance and plasma voltage in a focused argon plasma. Circuit analysis has been performed to verify the simulation results. The measured and simulated inductance in the argon plasma agree with each other. The measured plasma resistance can also verify the simulation results regarding the occurrences of the anomalous resistance in the post-pinch phase. The measured anomalous resistance reaches up to 0.2ohms after the pinch phase. This result also confirms the inductive or resistive nature of the current drop and the peak of the plasma voltage after the pinch phase.

A significant contribution of the plasma resistance, in the energy consumption by a pinching plasma in argon gas, has been related to the required condition of LHDI in plasmas as one of the main instabilities that makes the plasma resistance anomalous. A drop of temperature in the post pinch-phase decreases the effective charge of the ion in that phase. Decreasing the effective charge of the heavy ions and plasma density in the post-pinch phase is the favourable condition for LHDI in plasmas. The occurrence of the anomalous Joule heating by the onset of the anomalous resistivity in the post pinch phase can also terminate the radiation-enhanced compression of the plasma. The energy spectrum of the ions generated in three operating gases show that the ion energy depends on the plasma voltage and the effective charge of the ion. Increasing the atomic number of the gas could enhance the energy of generated ions. The results corresponding to the ion current density are in agreement with the simulation results based on the Lee model.

The required experimental E-field across the plasma to generate significant runaway electrons and hard x-rays during the pinch phase and the phase with anomalous resistance, have been studied. The results show the significant generation of charged particles and hard x-rays at smaller E-field across the plasma column in the phase of anomalous resistances compared to the pinch phase. The signature of the anomalous resistance has been found in the post-pinch phase. The anomalous plasma heating process may enhance generation of runaway charged particle density in the plasma during the phase of anomalous resistance due to reduced Dreicer field. This result shows that plasma heating can enhance the efficiency of the plasma focus as a charged particle source.

Runaway electron generation in plasma focus devices and tokamaks have been compared by considering the primary (Dreicer theory) and secondary (Avalanche theory) runaway electron production. It has been found that the runaway electron generation conditions in tokamaks and plasma focus devices are consistent in terms of ratios between E and n_e, and between n_r and n_e. This is one of the important results that could open a new insight regarding runaway electron generation in large fusion reactors.

Further enhancement of the plasma focus efficiency as a charged particle source has been implemented through a new configuration of the discharge electrodes. The SAE-type plasma focus, with a combination of three electrodes to produce several focusing events, has been developed for the first time. Analysis of the discharge circuit of the device shows the occurrence of the three focusing events. The preliminary results corresponding to ion beam emissions and hard x-ray radiations from a DPF-SAE device are very promising. The long duration and high

intensity of ion beam and hard x-ray signals from a DPF-SAE show a higher efficiency of this device as a charged particle source for medical and industrial applications.

6.2 Suggested Future Research

Runaway electron generation by considering loss process in a plasma focus is one the interesting research areas that can be pursued on DPF UofS-I. Beside, LHDI instability in pinching plasma can be studied by using ultrafast oscilloscope (10 GHZ) to see the effects of this instability on occurrence of anomalous resistance in plasma. Plasma temperature measurement in post pinch phase of anomalous resistances also can provide extra evidence of anomalous heating in that phase. Modeling of pinching plasma in a DPF-SAE device based on electrodynamics and thermodynamics of the plasma can be an interesting theoretical research area to predict the behavior of plasma in the new plasma focus configuration. Optimization of DPF-SAE device based on geometry of discharge electrodes and insulator length can be a matter of new research to enhance beam generation from the device.

Mechanisms of charged particle and x-ray generation in a SAE type plasma focus, energy spectrum of ion beam, electron beam and x-rays generated from an SAE type plasma focus, and plasma temperature measurement during focusing phase in an SAE type plasma focus can also give an understanding about formation and interaction of several pinch accelerators in a plasma focus device.

Neutron emission from a SAE type plasma focus is another subject of research that can be studied after some lab safety considerations. Measuring the energy and number of neutrons would also give some information about the interaction of several pinch regions in the plasma.

Operation of medium and high stored energy SAE type plasma focus, and developing an SAE type plasma focus for medical and industrial applications also are suggested future work that can be planned based on the outcome of this thesis.

REFERENCES

[1] M.G. Hanies, Plasma Phys. Control. Fusion 53, 093001 (2011).

[2] N.V. Filippov, T.I. Filippova, and V.P. Vinogradov, Nucl. Fus. Suppl. Pt. 2, 577 (1962).

[3] J.W. Mather, Phys. Fluids 8, 366 (1965).

[4] S. Lee and A. Serban, IEEE Trans. Plasma Sci. 24(3), 1101-1105 (1996).

[5] A. Bortolotti, J.S. Brzosko, I. Ingrosso, F. Mezzetti, V. Nardi, C. Powell and B.V. Robouch, Nucl. Instrum. and Meth. Phys. Res. B 63(4), 473-476 (1992).

[6] F. Castillo-Mejía, M.M. Milanese, R.L. Moroso, J.O. Pouzo and M.A. Santiago, IEEE Trans. Plasma Sci. 29(6), 921-925 (2001).

[7] S. Javadi, M. Habibi, M. Ghoranneviss, S. Lee, S. H. Saw and R.A. Behbahani, Phys. Scr. 86(2), 5801 (2012).

[8] R.S. Rawat, W.M. Chew, P. Lee, T. White and S. Lee, Surf. Coat. Technol. 173 (2), 76–84 (2003).

[9] M.V. Roshan, S.V. Springham, R.S Rawat, P Lee, IEEET. Plasma Sci. 38 (12), 3393–3397 (2010).

[10] M.G. Haines, Nuclear Instruments and Methods 207, 179-185 (1983).

[11] V. Zambreanu and C.M. Doloc, J. Plasma Phys. Control. Fusion 34 (8), 1433 (1992).

[12] R.A. Behbahani and F.M. Aghanir, Physics of Plasmas 18, 103302 (2011).

[13] F.M. Aghanir and R.A. Behbahani, Journal of Applied Physics 109, 043301 (2011).

[14] S. Lee *et al*, Am. J. Phys. 56, 62-68(1988).

[15] S. Lee, IEEE Trans. Plasma Sci. 19, 912-919 (1991).

[16] S. Lee and S.H. Saw, J. Fusion Energy 27, 292-295 (2008).

[17] S. Lee, S.H. Saw, P.C.K. Lee, R.S. Rawat and H. Schmidt, Appl. Phys. Lett. 92, 111501 (2008).

[18] S. Lee and S.H. Saw Appl. Phys. Lett. 92, 021503(2008).

[19] S. Lee, P. Lee, S.H. Saw and R.S. Rawat, Plasma Phys. Control. Fusion 50, 065012 (2008).

[20] R.A. Behbahani, T.D. Mahabadi, M. Ghoranneviss, M.F. Aghamir, Plasma Physics and Controlled Fusion 52(9), 095004 (2010).

[21] F.M. Aghamir and R.A. Behbahani, J. Plasma Fusion Res. SERIES 8, 1262-1268 (2009).

[22] L.H. Lim, S.L. Yap[1], L.K. Lim, M.C. Lee, H.S. Poh, J. Ma, S.S. Yap and S. Lee, Physics of Plasmas 22, 092702 (2015)

[23] H. Dreicer, Phys. Rev. 115, 238 (1959).

[24] J.M. Bernstein, Phys. Fluid 13, 2858 (1970).

[25] Y. Kondoh, K. Hirano, Phys. Fluid 21, 1617 (1978).

[26] V. Zambreanu, C.M. Doloc, Plasma Phys. Control. Fusion 34, 1433 (1992).

[27] S. Gary, Phys. Fluid 17, 2135 (1974).

[28] A. Bernard, H. Bruzzone, P. Choi, H. Chuaqui, V. Gribkov, J. Herrera, K. Hirana, A. Krejei, S. Lee, C. Luo, F. Mezzetti, M. Shadowski, H. Schmidt, K. Ware, C.S. Wong, V. Zoita, Moscow J Phys. Soc. 8, 93 (1998).

[29] B.A. Trubinkov and S.K .Zdanov, ZTEP 70, 92 (1976).

[30] W. Neff, R. Noll, F. Ruhll, R. Lerbert, Nucl. Instrum. Meth. in Phys.Res. A 258,253 (1989).

[31] K. Hirano, N. Hisatome, T. Yamamoto, and K. Shimoda, Rev. of Sci. Instrum. 65(12), 3761–3765 1994).

[32] M. Zakaullah, I. Akhtar, A. Waheed, K. Alamgir, A. Z. Shah, and G. Murtaza, Plasma Sources Science and Technology 7(2), 206–218 (1998).

[33] F. N. Beg, I. Ross, A. Lorenz, J. F. Worley, A E. Dangor, and M.G. Haines, Journal of Applied Physics 88(6), 3225–3230 (2000).

[34] H. Herold, H. J. Kaeppelar, H. Schmidt *et al*., in Proceedings of the 12th International Conference on Plasma Physics and Controlled Nuclear Fusion Research 2, 587 (1988).

[35] F.M. Farzin M. Aghamir and R.A. Behbahani, Chinese Physics B 23, 6 (2014).

[36] M. Zakaullah, K. Alamgir, M. Shafiq, M. Sharif, A. Waheed, and G. Murtaza, Journal of Fusion Energy 19, 143–157 (2000).

[37] V. A. Gribkov, A. Banaszak, Bienkowska, A.V. Dubrovsky, I. Ivanova-Stanik, L. Jakubowski, R.A. Miklaszewski, M. Paduch, M.J. Sadowski, M. Scholz, A. Szydlowski and K. Tomaszewski J. Phys. D: Appl. Phys. 40, 3592-3607 (2007).

[38] J.S. Brzosko and V. Nardi, Phys. Lett. A 155, 162 (1991).

[39] J.S. Brzosko, V. Nardi, J.R. Brzosko, D. Goldstein, Phys. Lett. A 192, 250(1994).

[40] J.S. Brzosko, K. Melzacki, C. Powell, M. Gai, R.H. France III, J.E. McDonald, G.D. Alton, F.E. Bertrand, J.R. Beene, Application of Accelerators in Research and Industry, 16th International Conference, eds J.L. Dugganand I.L. and Morgan, AIP 277 (2001).

[41] M.V. Roshan, S.V. Springham, R.S. Rawat, P. Lee, IEEET. Plasma Sci. 38 (12), 3393–3397 (2010).

[42] E. Angeli, A. Tatari, M. Frignami, V. Mollinari, Nucl.Technol.Radiat.Protection, 20(1), 33-37 (2005).

[43] H. Kelly and A. Marquez, Plasma Phys. Control. Fusion 38(11), 1931–1942 (1996).

[44] M.V. Roshan, S.V. Springham, A. Talebitaher, R.S. Rawat, and P. Lee, Phys. Lett. A 373 (8/9), 851–855 (2009).

[45] S. Lee, S.H. Saw, A. E. Abdou and H. Torreblanca, J. Fusion Energy 30, 277-282 (2011).

[46] M.V. Roshan, S. Razaghi, F. Asghari, R.S. Rawat, S.V. Springham, P. Lee, S. Lee, T.L. Tan, Physics Letters A 378, 2168–2170 (2014).

[47] S. Javadi, M. Habibi, M. Ghoranneviss, S. Lee, S.H. Saw and R.A. Behbahani, Phys. Scr. 86(2), 5801 (2012).

[48] R.S. Rawat, W.M. Chew, P. Lee, T. White and S. Lee, Surf. Coat. Technol. 173 (2), 76–84 (2003).

[49] R.S. Rawat, P. Lee, T. White, L. Ying and S. Lee, Surf. Coat. Technol. 138, 59–65 (2001).

[50] R. Gupta and M.P. Srivastava, Plasma Sources Sci. Technol. 13, 371–374 (2004).

[51] J.N. Feugeas, G. Sanchez, C.O. De Gonzalez, J.D. Hermida and G. Scordia, Radiat. Eff. Defects Solids 128, 267–75 (1993).

[52] J.N. Feugeas, E.C. Llonch, C.O. de Gonzalez and G. Galambos, J. Appl. Phys. 64, 2648–51(1988).

[53] P. Agarwala, S. Annapoorni, M.P. Srivastava, R.S. Rawat and P. Chauhan, Phys. Lett. A 231, 434–8(1997).

[54] M.P. Srivastava, S.R .Mohanty, S. Annapoorni and R.S. Rawat, Phys. Lett. A 21, 563–7 (1996).

[55] Z.Y. Pan, R.S. Rawat, M.V. Roshan, J. Lin, R. Verma, P. Lee, S.V. Springham and T.L. Tan J. Phys. D: Appl. Phys. 42, 175001 (2009).

[56] T. Hussain, R. Ahmad, I.A. Khan, J. Siddiqui, N. Khalid, A. S. Bhatti and S. Naseem, Nucl. Instrum. Methods Phys. Res. B 276, 768–72 (2009).

[57] M. Sadiq, S. Ahmad, M. Shafiq, M. Zakaullah, Naseem, Nucl. Instrum. Methods Phys. Res B 252(2), 219–224 (2006).

[58] M. Sadiq, S. Ahmad, A. Waheed and M. Zakaullah**,** Plasma Sources Sci. Technol**.** 15, 295 (2006).

[59] A. Henriquez, H. Bhuyan, M. Favre, B. Bora, E. Wyndham, H. Chuaqui, S. Mändl, J .W. Gerlach and D. Manova , J. Phys.: Conf. Ser. 370, Conference 1, 2010 (2012).

[60] M.T. Hosseinnejad, M. Ghoranneviss, G.R. Etaati, M. Shirazi, Z. Ghorannevis, Applied Surface Science 257(17), 7653-7658 (2011).

[61] L.T. Lue, C.K. Yeh , Y.-Y. Kuo, IEEE Electron Device Letters 4(12), 457-459 (1983).

[62] R. Gupta and M.P. Srivastava, Plasma Sources Sci. Technol. 13(3), 371-374 (2004).

[63] J. Csikai, Proc. of the enlargement workshop on "Neutron Measurements and Evaluations for Applications", Budapest, Hungary, Report EUR 21100 EN (2003).

[64] A.M. Pollard, C. Heron, Archaeological chemistry, Cambridge, Royal Society of Chemistry (1996).

[65] F.D. Brooks, A. Buffler, M.S. Allie, K. Bharuth-Ram, M.R. Nchodu and B.R.S. Simpson, Naseem, Nucl. Instrum. Methods Phys. Res. A 410, 319–328 (1998).

[66] Y. Yang, Y. Li, H. Wang, *et al*., Naseem, Nucl. Instrum. Methods Phys. Res. A 579, 400–403 (2007).

[67] K. Yoshikawa, K. Masuda, T. Takamatsu, S. Shiroya, T. Misawa, E. Hotta, M. Ohnishi, K. Yamauchi, H. Osawa, Y. Oshiyuki, Naseem, Nucl. Instrum. Methods Phys. Res. B 261, 299–302 (2007).

[68] E.T.H. Clifford, J.E. McFee, H. Ing, H.R. Andrews, D. Tennant, E. Harper, A.A. Faust, Naseem, Nucl. Instrum. Methods Phys. Res. A 579, 418–425 (2007).

[69] V.A. Gribkov, R.A. Miklaszewski, Proc. of an IAEA Tech. Meeting, Padova, IAEA-TM-29225, A-03 (2006).

[70] G. Verri, F. Mezzetti, A. Da Re, A. Bortolotti, L. Rapezzi, V.A. Gribkov, NUKLEONIKA 45(3), 189-191 (2000).

[71] S. Lee, S.H. Saw and A. Jalil, J Fusion Energy 32, 42-49 (2013).

[72] S. Lee, S.H. Saw, Journal of Physics: Conference Series 591, 012022 (2015).

[73] R.A. Behbahani and C. Xiao, Physics of Plasmas 22, 020708 (2015).

[74] H. Bruzzone , M. Barbaglia , H. Acuna , M. Milanese , R. Moroso , and S. Guichon , IEEE Trans. Plasma Sci. 41, 3180 (2013).

[75] B.L. Bures, M. Krishnan, and R. Madden, IEEE Trans. Plasma Sci. 38(4), 667-671 (2010).

[76] F. Veloso, C. Pavez, J. Moreno, V. Galaz, M. Zambra, and L. Soto, J. Fusion Energy 31, 30 (2012).

[77] H. Bruzzone, H. Acuna, M. Barbaglia, and A. Clausse, Plasma Phys. Controlled Fusion 48, 609 (2006).

[78] M. Barbaglia, H. Bruzzone, H. Acuña, L. Soto, and A. Clausse, Plasma Phys. Controlled Fusion 51, 045001 (2009).

[79] R. Pease, Procs. Phys. Soc. 70, 11 (1957).

[80] A. Robson, Phys. Fluids B 3, 1461 (1991).

[81] L. Bernal, H. Bruzzone, Plasma Phys. Control. Fusion 44, 223–231 (2002).

[82] R.S. Granetz, B. Esposito, J.H. Kim, R. Koslowski, M. Lehnen, J. R. Martin-Solis, C. Paz-Soldan, T. Rhee, J.C. Wesley, L. Zeng, Physics of Plasmas 21, 072506 (2014).

[83] R.A. Behbahani, A. Hirose and C. Xiao, Europhysics letter 113 55001(2016).

[84] Ja. H. Lee, D.R. McFarland, Wynford**,** Plasma Phys. 20, 1025-1038 (1978).

[85] Ja H. Lee, D.R. McFarland, and F. Hohl, Physics of Fluids 20(2), 313-321 (1977).

APPENDIX

1-Electrodes assembly: